



The University of
Nottingham

UNITED KINGDOM • CHINA • MALAYSIA

Advancements in discontinuous carbon fibre composite technologies for high- volume manufacturing processes

Zhaofei Xiao

MSc

Thesis submitted to the University of Nottingham for the degree of Doctor of
Philosophy

February 2018

Abstract

With a growing interest for lightweight design in the automotive industry, carbon fibre reinforced composite materials have attracted considerable attention from manufacturers as a means to save energy and improve vehicle performance. However, high material costs and long processing times for conventional carbon fibre fabrics limit their application to niche vehicle applications (<5,000ppa) where the unit costs are typically much higher than mainstream alternatives. Directed Carbon Fibre Preforming (DCFP) offers a low-cost and short (5 minutes) manufacturing cycle to produce semi-structural components from discontinuous fibres for volumes of up to 100,000ppa. However, conventional liquid moulding routes, such as resin transfer moulding or vacuum infusion are unable to match the short cycle times possible with this preforming step.

This thesis seeks to optimise the DCFP process to produce preforms suitable for serial production processes, such as High-Pressure Resin Transfer Moulding (HP-RTM). Preforms are optimised to achieve low areal mass variability (< 5%) for both simple 2D and complex 3D components, whilst ensuring they can withstand high in-mould pressures (up to 150 bar). A study of binder type and binder content is presented which demonstrates that optimal binder parameters can lead to higher overall mechanical properties compared to plaques produced by conventional RTM. Higher binder content prevents the preform from distorting (washing) when subjected to high injection pressures, which consequently results in lower void content compared to standard RTM. Using higher injection pressures can therefore effectively increase mechanical performance.

However, increasing binder content to 10% vol significantly affects the preform permeability, reducing it by approximately 30% when the target fibre volume fraction is 31%. A permeability model has been developed using a force-directed algorithm to create representative 3D volume elements of the preform architecture to include realistic through-thickness fibre distributions. The effect of binder content has been incorporated by adjusting the principal permeability values of the meso-scale tows, using experimental permeability measurements from unidirectional non-crimp fabrics. The model provides an upper boundary for the permeability of DCFP architectures.

Fibre homogeneity directly influences the tensile strength of DCFP, which can be controlled through tow size, fibre length and component thickness. However, the ultimate tensile strength is typically limited to $\sim 300\text{MPa}$ for an isotropic fibre distribution at 50% volume fraction when using industrial grade fibres (UTS $\sim 4900\text{MPa}$). This thesis investigates the opportunity for using higher performance aerospace grade carbon fibres to increase the ceiling tensile strength for plaques made from randomly orientated bundles and an epoxy matrix. Results indicate that using fibres with higher strengths do not necessarily result in higher composite component strengths, due to resin dominated failures. However, significant improvements in stiffness can be achieved, with the most cost-effective solution (stiffness per £) achieved by blending two carbon fibre grades together in the relative volume ratio of 10/90 (high stiffness fibre/low stiffness fibre).

Commercially available foam cores are unable to withstand the high moulding pressures encountered with HP-RTM, therefore it is difficult to produce lightweight

hollow sections using DCFP preforms for high volume applications. The development of a low-cost water-soluble core material is presented in this thesis, which is suitable for producing hollow composite structures. The bulk material of the core is sodium chloride (NaCl), which is held together by a water-soluble trehalose sugar binder. The composition of the core has been optimised to provide acceptable dissolution rates and mechanical properties for high volume structural composite applications. The compressive strength of the NaCl core is 57 MPa at ambient temperature, which reduces to 20 MPa when tested at 120°C. The compressive strength at elevated temperature is approximately 4 times higher than that of a water-soluble commercial benchmark and 33 times higher than a conventional structural closed-cell foam. The specific dissolution rate of the NaCl core is between 0.14 – 1.23 kg/(min·m²), depending on processing parameters, and the coefficient of thermal expansion is approximately 43 10⁻⁶/K. A practical example has been presented to demonstrate how the removable core can be used to produce a representative hollow section of an integrally stiffened panel.

Acknowledgement

I would like to take this opportunity to express appreciation to my supervisor Dr Lee Harper for his enormous help, technical support and guidance during my PhD period.

I would also like to thank Professor Nick Warrior for introducing me to the world of composite materials, which I love, and I would like to acknowledge Dr Connie Qian for her support and advice.

I would also like to thank Professor Andy Kennedy, Dr Andreas Endruweit and Dr Thomas Turner for their invaluable support to help me finish this thesis successfully. In addition, all members of the University of Nottingham's Composites Research Group are acknowledged for their assistance, in particular technicians Paul Johns, Ben Jennison and Harry Crocker.

Finally, I'm indebted to my wife Dr Zhe Liu and my parents for their love, support and encouragement.

Content

Abstract.....	3
Acknowledgement	6
Content	7
Nomenclature	11
Preface	14
Chapter 1 Introduction	16
1.1 Drivers of lightweight materials.....	16
1.1.1 Development trend in automotive industry	16
1.1.2 Materials, weight and cost.....	17
1.2 Discountinuous fibre composites and applications	19
1.3 Directed carbon fibre preforming.....	22
1.4 Core Materials.....	23
1.5 Theme of work	25
Chapter 2 Literature review.....	28
2.1 DCFP composites manufacturing technologies	28
2.1.1 DCFP process development	28
2.1.2 Moulding technologies for DCFP preforms – RTM, HP-RTM, and Compression moulding 29	
2.2 Factors influencing mechanical properties of DCFP components	32
2.2.1 Effects of fibre architecture parameters.....	32
2.2.2 Analytical models for strength and modulus of discontinuous carbon fibre composites	35
2.2.3 Effect of binder	37
2.3 Conclusions	39
Chapter 3 Experimental methodology.....	40
3.1 Preforming process development.....	40
3.2 Characterisations	43
3.2.1 Tensile test of dry DCFP preforms	43
3.2.2 Mechanical testing	44
3.2.3 Void analysis.....	47
Chapter 4 Manufacturing process studies.....	48
4.1 2D Preforming path studies	48
4.1.1 Fibre deposition process characterisation	48

4.1.2	2D preforming process.....	51
4.1.3	Areal mass variability measurement.....	52
4.2	Study of in-plane isotropy of 2D DCFP composites	56
4.3	3D T-shirt preform	58
4.3.1	Preforming process development.....	58
4.3.2	Areal mass variation measurement of 3D preform	60
4.4	Effects of binder on structural integrity of the DCFP preform	63
4.5	Effect of binder on properties of moulded DCFP.....	66
4.6	Effect of moulding process	67
4.6.1	Plaque manufacture.....	68
4.6.2	Results.....	69
4.7	Conclusions	74
Chapter 5	Permeability modelling of DCFP preforms.....	77
5.1	Review of literature related to permeability of composite materials	77
5.1.1	Permeability measurements.....	78
5.1.2	Factors influencing preform permeability	80
5.1.3	Permeability modelling.....	84
5.1.4	Conclusion.....	88
5.2	Experimental permeability measurement to investigate the effect of binder.....	89
5.2.1	Methodology.....	89
5.2.2	Measurement uncertainty	90
5.2.3	The effect of binder on permeability	92
5.3	DCFP permeability model creation	97
5.3.1	Model architecture	97
5.3.2	Random fibre generator.....	98
5.3.3	Fibre geometry analysis programme	100
5.3.4	Local permeability calculation	106
5.3.5	Flow simulations using PAM-RTM.....	107
5.4	DCFP permeability model validation.....	108
5.4.1	Validation of fibre geometry analysis programme	108
5.4.2	Predicted DCFP permeability results	115
5.5	Conclusions	117
Chapter 6	Structural investigations of DCFP using high strength and high modulus carbon fibres	119
6.1	Materials	119
6.2	Effects of fibre properties on strength and stiffness of DCFP	122

6.2.1	Strength.....	123
6.2.2	Stiffness.....	127
6.3	Effects of fibre hybridisation.....	128
6.4	Effect of fibre selection on impact properties	133
6.5	Overview of structural investigations of DCFP using high strength and high modulus carbon fibres	134
Chapter 7 Impulse excitation measurement for rapid Young's modulus determination of DCFP components.....		136
7.1	Background	136
7.2	Impulse excitation measurement setup	137
7.3	Comparison of modulus measurement between IET and tensile testing.....	138
Chapter 8 A water-soluble core material for manufacturing hollow composite sections.....		140
8.1	Introduction	140
8.2	Background	140
8.3	Water-soluble core development methodology	143
8.3.1	Design of experiment.....	144
8.3.2	Experimental methods.....	145
8.4	Core strength at ambient.....	149
8.5	Phase characterisation of trehalose	153
8.6	Core density	156
8.7	CTE measurement.....	157
8.8	Specific dissolution rate (SDR) measurement.....	157
8.9	Elevated temperature testing.....	159
8.10	Post moulding operations.....	163
8.11	Conclusions	166
Chapter 9 Thesis conclusions.....		168
9.1	Fibre volume fraction variability reduction	168
9.2	Complex 3D component manufacturing.....	169
9.3	High pressure DCFP moulding.....	169
9.4	Numerical permeability modelling	171
9.5	Mechanical property improvement using high strength and high modulus fibres	172
9.6	Rapid Young's modulus measurement technique	173
9.7	Novel water-soluble core development for manufacturing hollow composite sections	173
9.8	Future work.....	174
Appendices.....		176

Appendix A List of publication	176
Appendix B Matlab code of the Fibre Architecture Analysis Programme	177
References	182

Nomenclature

Abbreviations

AFP	Automated Fibre Placement
ATL	Automated Tape Laying
BMC	Bulk Moulding Compound
CFRP	Carbon Fibre Reinforced Plastic
CF-SMC	Carbon Fibre Sheet Moulding Compound
CTE	Coefficient of Thermal Expansion
DCFP	Directed Carbon Fibre Preforming
DFC	Discontinuous Fibre Composites
DFP	Directed Fibre Preforming
DSC	Differential scanning calorimetry
F3P	Ford Programmable Preforming Process
HP-RTM	High pressure Resin Transfer Moulding
IET	Impulse Excitation Technology
NCF	Non-Crimp Fabric
NT Core	NaCl-Trehalose Core
OEM	Original Equipment Manufacturer
P4	Programmable Powered Preforming Process
RTM	Resin Transfer Moulding
ROM	Rule Of Mixture
SDR	Specific Dissolution Rate

SMC	Sheet Moulding Compound
SRIM	Structural Reaction Injection Moulding
TCP	Tool Centre Point

Symbols

C_1	Geometry constant
C_2	Geometry constant
D_f	Fibre diameter
D_h	The spacing between tow height positions
D_{tow}	The true spacing between tows
E_c	Young's modulus of composites
E_f	Young's modulus of fibre
E_m	Young's modulus of matrix
F	Failure probability
f_f	Flexural resonant frequency
G_m	Shear modulus of matrix
H	Height
K	Permeability tensor
K_0	Kozeny constant
L	Length
N_n	Number of node
ΔP	Pressure gradient
R	Fibre packing factor
r	Radius

S_s	Seed size of fibre model
S_g	Grid size in permeability model
T	Correction factor
t	Time
V_f	Volume fraction of fibre
V_{fmax}	Max volume fraction of fibre
V_m	Volume fraction of matrix
v	Average volume velocity
W	Width
α_i	The proportion of fibres at orientation θ_i
θ_i	Fibre orientation
η_l	Length factor
η_o	Orientation factor
η	Fluid viscosity
σ_c	Stress of composites
σ_f	Stress of fibre
σ_m	Stress of matrix
ϵ	Strain

Preface

Discontinuous fibre composites are relatively easy to process and have much shorter processing cycle times compared to conventional fabric-based materials. They are therefore seen as a potential solution for lightweighting within the automotive industry, but there are a number of challenges still to overcome, as shown in Figure.1. Due to the randomly orientated fibre architecture and large stress raisers at the bundle ends, the mechanical properties of discontinuous fibre composites are lower than those of continuous fibre composites. Their discontinuous fibre structure can also complicate the moulding process, as severe fibre washing can occur under high in-mould pressure for rapid moulding processes, such as HP-RTM and compression moulding. The high fibre areal mass variability is another major challenge, because it directly influences the variability of the inter- and intra-plaque mechanical properties. Typically, many specimens need to be tested to achieve a representative mean value for material properties, which is time consuming, and low confidence in mechanical performance results in conservative designs. Additionally, local fibre volume fraction variation makes it difficult to predict the resin fill pattern during infusion, since the local permeability is also variable and can lead to high reject rates when components are improperly filled. Ultimately these challenges can be overcome, but consequently there are a lack of tools for discontinuous fibre composites to assist with material and process development and component design. This prevents OEMs from exploiting the full potential of these materials to pursue integrated, lightweight designs.

This thesis seeks to optimise the preforming process of discontinuous fibre composites to reduce preform areal mass variability. The compatibility of

discontinuous fibre composites with a rapid moulding processes, HP-RTM, is investigated, aiming to further shorten manufacturing cycle and improve mechanical properties. The work is supported by the development of a numerical permeability model, to provide accurate moulding flow simulations. The fibre materials are also investigated to seek a cost-effective fibre to produce high property composites. Furthermore, a novel, removable core material is developed to create hollow sections for integrally stiffened panels.

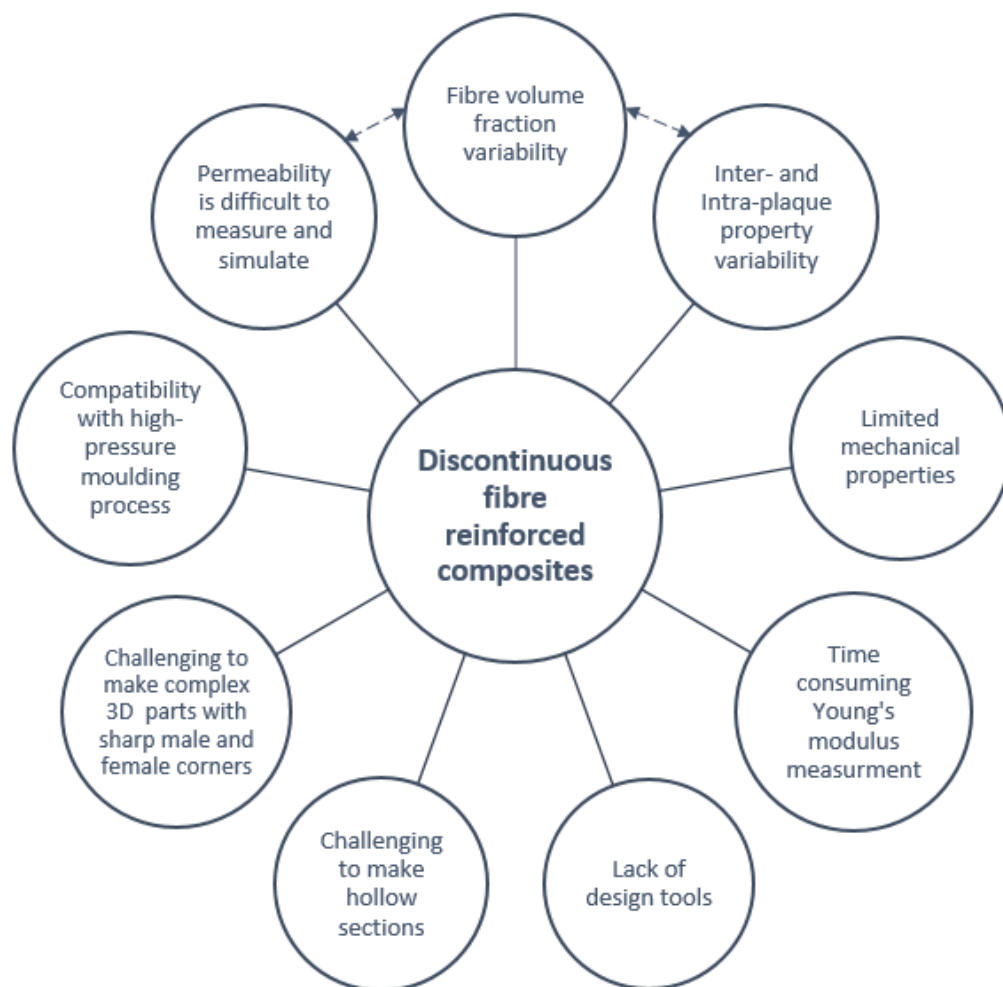


Figure.1 Current challenges preventing wider adoption of discontinuous fibre composites in structural automotive applications

Chapter 1 Introduction

Increasingly stringent emission regulations and global fuel shortages place enormous pressure on automobile companies around the world. Whilst many vehicle manufacturers have started to develop and produce hybrid and electric vehicles (EV) to overcome these challenges, hybrid powertrains and batteries add significant extra weight compared to conventional combustion engines, which brings adverse effects on energy consumption. Hence, weight reduction of the whole vehicle is crucial and carbon fibre composites offer one potential solution because of their low density and high mechanical performance. The main barrier to adoption is the cost of the raw materials and the long processing cycle times compared to conventional metallic solutions.

1.1 Drivers of lightweight materials

1.1.1 Development trend in automotive industry

According to the Paris Agreement (2016) [1], the European Union (EU) must achieve at least a 40% reduction in greenhouse gas emissions by the year 2030, and 80% by 2050, compared to 1990 levels. Hence, the EU has placed increasingly stringent CO₂ emission regulations on cars, since they contribute ~12% of total CO₂ emission in the EU [2]. From 2020, all new cars need to achieve 95 g CO₂/km, which is 40% less than the emission standard in 2015 [2]. This means a fuel consumption of 4.1 l/100km for a petrol engine [2]. Whilst some manufactures such as Tesla have built all-electric vehicles, the weight of the lithium ion batteries contribute to over a quarter of the vehicle weight (~540kg compared to 2000kg) [3]. According to Helms and Lambrecht

[4], fuel consumption will drop by over 0.3 l/100km, if the weight of a vehicle is 100kg lighter. Therefore, there are significant weight savings to be made in the rest of the structure using innovative designs and lightweight materials.

1.1.2 Materials, weight and cost

Steel is the most common material used in modern vehicles, not only because it provides adequate properties, but also because the manufacturing process has been improved after decades of research and development, which means production costs are minimised. However, the high density of steel (7.8 g/cm^3) limits its application in lightweight-design. The use of aluminium alloys in body panels, engines, and chassis designs has progressed, as the density (2.7 g/cm^3) is only about one third compared to steel. In the late 1990's, Audi made an all-aluminium space frame for its flagship model the A8. This technology was successfully transferred to a higher volume city car, the Audi A2, which weighed only 895kg. Over 60,000 A2s were produced a year, compared to just 15,000 for the A8 [5]. The A2 was 43% lighter than a comparable steel structure, due to the innovative aluminium space-frame. Whilst the A8 and A2 were a success, aluminium platforms are more difficult to repair and consequently many accident-damaged vehicles were scrapped. Raw material costs are also higher than steel and forming and joining are more difficult [6]. Jaguar Land Rover first adopted aluminium for the 2003 XJ model and currently uses it across the entire Jaguar range. Developments since 2003 have seen Jaguar Land Rover's minimum stamping radii reduced from 12mm to 8mm.

Carbon Fibre Reinforced Plastics (CFRPs) are the latest generation of lightweight materials used in modern automotive designs, since they offer low density (only ~60%

compared to aluminium alloys, $\sim 1.4\text{g/cm}^3$) and high stiffness and strength per unit weight. Additionally, CFRPs also have good corrosion resistance, and their properties can be tailored easily to suit the load requirements [7]. The McLaren P1 MSO carbon series, shown in Figure 1.1, is a good example to show the application of carbon fibre composites. It has a fully integrated carbon fibre tub (monocell) and all of the external body panels, front/rear bumpers and rear spoiler are made from carbon fibre for further weight reduction. The same technology is used to produce the monocell for all McLaren vehicles, resulting in 4,000 vehicles per annum. However, due to high raw material costs, touch-labour intensive processing and long cycle times (several hours), the application of CFRPs in higher volume manufacturing is limited [8]. For cost control, there are only 3 components manufactured from CFRP in the Audi R8 V10 space frame: the B pillars, the central tunnel and the rear bulkhead [9]. This multi-material design only uses carbon fibre for components that can be manufactured using automation, which are therefore geometrically simple. Multi-material designs will become more common in the future, but they will inevitably require innovative solutions for joining CFRPs and metals together.



Figure 1.1 McLaren P1 MSO carbon series and its carbon tub

In today's competitive market, a demand for more efficient production techniques is emerging in order to increase the volume of CFRP components in the automotive industry. Current limitations include the high capital investment for processes such as Automated Fibre Placement (AFP) and Automated Tape Laying (ATL), which tend to be dedicated to manufacturing just one component [10, 11]. These processes in particular are also limited in terms of fibre laydown rate (typically less than 15 kg/hour) [10], especially if the component geometry is complex and features double curvature [10]. AFP/ATL are therefore commonly reserved for aerospace applications producing wing skins and fuselages [10, 11], where machines can work at their optimum, laying down material over long distances.

For automotive applications, non-crimp fabrics and woven materials are thermoformed to create smaller, more complex, 3D preforms [12, 13] but material utilisation is limited to typically 60-70% [14, 15]. In time, net-shaped 2D preforms may be printed using AFP, but the current laydown rate is too low to meet demand. For example, a deposition rate of ~400 kg/hour is required for the BMW i3 at 40,000 vehicles per annum (each vehicle has ~300 kg of composites [16], assuming an average fibre weight fraction of 60%), which cannot be currently achieved with current aerospace focused machines.

1.2 Discountinuous fibre composites and applications

Compared to countinuous fibre composites, discountinuous fibre composites (DFCs) offer a compromise in terms of cycle time and component cost, as the production process of DFCs can be easily automated and material processing is less complicated compared to woven fabrics and pre-preg. Therefore, DFCs are the most widely

adopted fibre reinforced materials within the automotive industry, accounting for 90% of all composites used. Fibre length and reinforcement scale (filaments or bundles) can be varied greatly in these materials, enabling the mechanical properties to be tailored for specific applications. For DFCs, fibres are randomly distributed in the matrix in two ways to form different structures: a 2D layered structure or a 3D structure, as shown in Figure 1.2 [17]. In terms of the application of DFCs in the automotive industry, bulk moulding compounds (BMCs), which typically consist of individual short filaments distributed in the matrix, are used to produce low performance parts. The fibre distribution limits the fibre volume fraction to approximately 20%. Sheet moulding compounds (SMCs) are composed of layers of randomly aligned chopped bundles [18], which increases the ceiling volume fraction to approximately 50% [19]. Compression moulded SMCs have been used in vehicles since the 1970's. Body panels for the 1997 Renault Espace [20] were made from glass SMC, as were the body panels for the Alfa Romeo 4C [21]. The bonnet of the Chevrolet Corvette Z06 was manufactured from a carbon SMC [22]. Lamborghini developed 'Forged Composites', an advanced carbon fibre SMC, launched at the 2010 Paris Auto Show [23]. In 2017, the Lamborghini Huracan Performante used Forged Composites for the interior trim and front and rear spoilers [24].

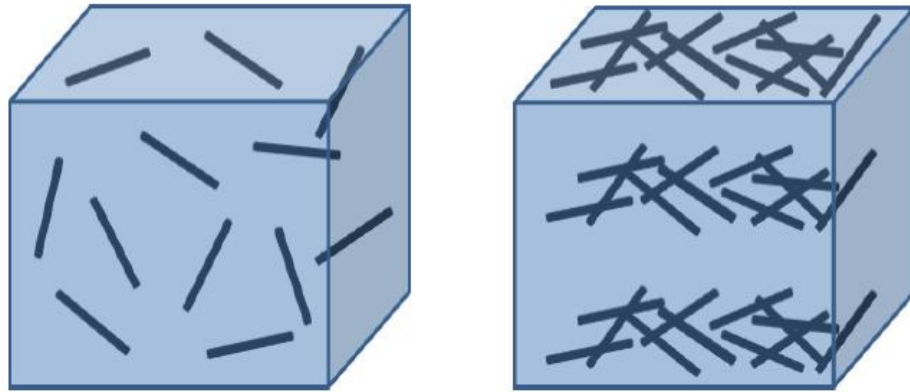


Figure 1.2 Fibre distribution of discontinuous fibre composites: 3D orientation (left) and 2D orientation (right) [17]

Carbon SMCs have superior mechanical properties to glass-based SMCs, with tensile stiffness and strength values of approximately 35 GPa and 300 MPa respectively (at 50% fibre volume fraction). The major problem is the cost of these materials. The most successful materials, such as Hexcel's HexMC, as used on the Boeing 787 window surround [25], are derived from unidirectional prepreg and are typically £60-80/kg. HexMC is a carbon fibre / epoxy moulding compound and consequently the material does not flow all that well under pressure due to the high molecular weight of the resin. Other alternatives tend to use vinyl-ester matrices to overcome this problem, but the tensile strength of the composite suffers as a consequence (typically 50% lower) due to poor fibre/matrix adhesion.

The Directed Fibre Preforming (DFP) process produces DFCs for liquid moulding processes, such as resin transfer moulding (RTM) or resin infusion. The resulting fibre architecture is very similar to comparable SMC parts, but DFP enables low cost liquid epoxy resins to be used and avoids the need to produce a prepreg. In the DFP process, fibres are chopped and sprayed onto a perforated screen with a powder binder, using

a robotic arm to create a net-shaped preform. The Programmable Powered Preforming Process (P4) [26] was the first recognised DFP process using glass fibre. Ford developed the Ford Programmable Preforming Process (F3P) in 1998 [27], using string binder to replace the powder type, in order to prevent blockages on the perforated screen. As the process can be automated, the potential production rate of DFCs can achieve over 50,000 parts per annum (ppa). Sotira Composites successfully implemented this process to produce door opening rings and boot lid surrounds for the Aston Martin DBS, with a total part production volume of 15,000 ppa [28].

1.3 Directed carbon fibre preforming

The Directed Carbon Fibre Preforming (DCFP) process was developed at the University of Nottingham, as part of a UK government funded programme involving Aston Martin, Ford US and Hexcel (ALBOS – Affordable Lightweight Body Structures). The aim was to produce low cost, low wastage (<5%) preforms with short cycle times (5 - 10 minutes) for liquid moulding processes [8]. With the introduction of carbon fibre, DCFP components offered higher mechanical properties and lower weight than glass fibre counter parts, whilst still offering significant cost savings compared to using carbon fibre textiles.

DCFP has successfully been used to produce semi-structural components for the automotive industry [21, 28, 29], but major drawbacks include higher material variability ($\pm 20\%$) compared to continuous fibre composite processes [8], and lower mechanical properties; particularly tensile strength [8, 30]. Fibre alignment has been investigated to improve fibre packing to increase the ceiling fibre volume fraction

and therefore mechanical performance [31, 32], but this comes at the expense of reducing the fibre deposition rate [31].

Recent studies [33, 34] have investigated the possibility of creating hybrid fibre preforms, combining both continuous and discontinuous fibres in local regions to provide a compromise between material wastage, mechanical performance and the level of automation that can be applied. Evans et al. [34] indicated that the tensile stiffness and strength follow a linear relationship when an increasing volume of continuous unidirectional fibre is added to a discontinuous fibre architecture. The challenge is managing the stress transfer from the continuous fibres into the discontinuous fibre material within the transition zone, in order to avoid creating large stress concentrations that are detrimental to the composite strength. Hybrid material solutions offer a good compromise in terms of material deposition rates and mechanical performance, but it is important to ensure that the resulting material can be processed using conventional moulding routes. Corbridge et al. [33] have shown some of the challenges faced when co-compression moulding discontinuous fibre compounds and unidirectional prepregs, including ply migration and distortion of the unidirectional fibres.

1.4 Core Materials

It is currently difficult to produce hollow composite sections or sandwich panels from discontinuous fibre materials such as SMC or DCFP, which limits their weight saving potential compared to more optimised structures using continuous fibres. Foam materials are commonly used to form sandwich panels [35], but current high volume

composite manufacturing processes, such as compression moulding or high pressure resin transfer moulding (HP-RTM), can generate pressures of 30-150 bar inside the mould tool [36, 37], which means that closed-cell structural foams typically require very high densities (200 kg/m^3 for a compressive strength of 6 MPa [38]) to prevent crushing. These materials tend to stay in the final moulding and therefore add parasitic mass.

To facilitate the mass production of lightweight composites designs, a removable core material is required to support high-pressure moulding processes (e.g. compression moulding and HP-RTM). Furthermore, hollow structures can provide additional design flexibility, for example, routing of wiring harnesses and HVAC within structural composite components to further save weight and increase vehicle cabin space.

Removable core materials are available and are commonly used in the automotive industry for manufacturing hollow metallic structures, for example sand cores for casting cylinder blocks [39, 40]. Sand cores are held together by a binder material, such as sodium silicate, which hardens when exposed to carbon dioxide [41]. Mechanical removal methods, such as shaking and knocking, are required to extract the sand, which can be difficult if access is limited or the component is fragile, as the bonded sand particles do not readily flow [41]. Plastics such as polyoxymethylene (POM) and low melting temperature metals such as zinc based alloys (ZnAl4Cu1) are also used to make cores, and can be burnt off or melted out at elevated temperatures [39]. The removal temperatures for extractable polymers ($\sim 180^\circ\text{C}$) and metals (380°C) are typically incompatible with the polymer matrix, or they are insufficiently stiff and

can crush under the moulding pressure. Caustic solutions containing sodium hydroxide may be used for removing ceramic-based cores [42, 43], but this is harmful to the environment and can affect the mechanical performance of the finished product [44]. Current removable cores, such as Aquacore [45] also tend to be incompatible with high pressure moulding processes, as the resin can infiltrate into the core during the infusion process, impeding the core removal. Clearly there are opportunities for reducing the mass of structural composite components, but the challenge is finding a removable core material that can be subjected to high pressures, can be quickly and easily removed and can be manufactured at low cost.

1.5 Theme of work

DCFP was initially developed to produce preforms for Resin Transfer Moulding (RTM) [8, 46], but a 5 – 10 minute preforming cycle time means that the +30 minute RTM cycle is the bottle neck for producing higher volumes (>15,000ppa). This thesis investigates the possibility of producing discontinuous fibre composite components via high pressure RTM (HP-RTM) [47], which is amenable to higher production rates when combined with fast curing epoxy resins.

The inlet pressure for HP-RTM is typically 70 – 150 bar to achieve resin flow rates of 30-80 g/second [48, 49], which can create large forces within the preform and the possibility of fibre washing. Pinch points are typically used around the perimeter of HP-RTM tooling to prevent the movement of continuous fibre fabrics, but these are ineffective for discontinuous fibre materials as preforms can tear. Resistance to washing is therefore dependent on preform compaction and binder content. This

thesis investigates the influence of binder type and binder content on the dry preform strength and the corresponding ultimate tensile strength of the composite.

The void content is also compared between HP-RTM and RTM moulded DCFP plaques. Dry or poorly impregnated macroscale regions appear when the RTM resin flow front reaches the outlet gate prior to complete filling. This occurs due to local variations in DCFP preform permeability [50] and processing disturbances, such as race-tracking [51]. In addition, microscale voids can be generated in the material due to the inhomogeneous fluid flow propagation caused by the dual-scale of the preform [52].

Finally, a compression moulding route is investigated to understand if in-mould flow of the fibres can yield a more homogeneous fibre distribution and therefore reduce the material variability compared with the RTM/HP-RTM moulded plaques. Compression moulding is often overlooked because of the cost of tooling and the size of the press required, but in reality there is little difference between HP-RTM and compression moulding, as similar pressures are required to ensure the mould remains closed during injection.

Chapter 2 summarises a comprehensive literature review conducted for discontinuous fibre composites, in particular the factors affecting the mechanical properties. Chapter 3 presents the DCFP preforming facility and mechanical characterisation methods used in the thesis. Chapter 4 focuses on the optimisation of DCFP preforms to achieve uniform fibre distribution for both 2D and 3D structures. The mechanical properties of DCFP plaques are investigated to understand the level of in-plane isotropy for 2D DCFP preforms, and the effects of binder type, binder content and moulding process (RTM, HP-RTM and compression moulding).

A finite element model (Chapter 5) is presented to simulate the permeability measurement for DCFP preforms. A force-directed algorithm is used to create realistic 3D preform fibre architectures, accounting for the through-thickness fibre distribution. Local permeability values are calculated based on this architecture and then the global permeability is solved using PAM-RTM.

The effect of fibre strength and modulus on the mechanical properties of DCFP is investigated in Chapter 6. DCFP components with hybrid fibre architectures (two types of fibres with different modulus) are investigated to provide a balance between mechanical performance and material cost. In Chapter 7, a non-destructive modulus measurement method is conducted using acoustics and is compared with conventional mechanical tests. This provides a convenient inline quality control method that can potentially be used to identify component defects.

Chapter 8 presents the development of a low cost water-soluble NaCl-based core material, which is suitable for producing hollow composite structures via high pressure moulding processes (> 100 bar), such as compression moulding and HP-RTM. The composition of the core is optimised to provide rapid dissolution, and mechanical properties that exceed those of commercially available cores. A practical example is presented, using the removable core to produce representative hollow sections typically found in the automotive industry.

Chapter 2 Literature review

This chapter presents the literature review for the development of the Directed Carbon Fibre Preforming (DCFP) process and its moulding technologies. The factors affecting the mechanical properties of DCFP are also reviewed.

2.1 DCFP composites manufacturing technologies

2.1.1 DCFP process development

The Directed Carbon Fibre Preforming (DCFP) process is an automated method for producing net-shaped preforms for liquid moulding processes. The process typically consists of three steps: deposition, consolidation, and demoulding [8]. During the deposition stage, carbon fibre tow is cut into segments (fibre bundles) with constant length directly from the bobbin. The fibre bundles, along with a powder binder are then sprayed on the surface of the preforming tool by a fully automated robot arm. During the consolidation stage, the binder melts under heat to hold the fibres together, ensuring the preform becomes rigid (consolidated) once cured. The consolidated preform is then ejected from the tool during the demoulding stage. The cycle time can be as short as 5 – 10 minutes, and the material cost is minimised as fibre tows are used directly from the bobbin rather than applying extra intermediate processes to align or weave the fibres together. Furthermore, because the chopped bundles are deposited directly onto the mould to form net-shaped preforms, the material wastage is less than 5%wt. Although carbon fibre has higher tensile strength (~30 %) and stiffness (~300 %) than glass fibre, it also creates some difficulties in terms of the manufacturing process. The fibre chopping system in the P4 process [26] used for making glass fibre preforms was reported to be unsuitable for carbon fibre,

as blockages could easily occur [8]. Hence, the University of Nottingham further developed the chopping system to ensure it was compatible with carbon fibre. Additionally, the deposition of the low density tow (1.80 g/cm^3 for carbon fibre VS 2.54 g/cm^3 for E-glass) material is easily influenced by airstreams in the production cell, resulting in problems with preform consistency, particularly as the areal mass of the fibre layers increases [30].

2.1.2 Moulding technologies for DCFP preforms – RTM, HP-RTM, and Compression moulding

Resin transfer moulding (RTM) is a member of the liquid composite moulding family [53]. The key feature of this process is that a liquid resin is pushed into a closed mould with a dry preform inside under a certain pressure (typically $< 10\text{bar}$) provided by a pressure vessel or injection system. After the preform is fully impregnated by the resin and the resin is cured in the mould, the moulded component can be ejected. The RTM process is schematically shown in Figure 2.1. The use of this process can be traced back to the 1940s for manufacturing boats using glass fibre reinforced plastics, using a vacuum to assist the resin impregnation [53]. RTM has been widely used since the 1980's in the development of structural and semi-structural parts for automobiles, aircraft, sporting goods etc. [53]. Since the DCFP process was initially developed by the University of Nottingham, many studies have been carried out on the characterisation of DCFP parts moulded by RTM [8, 17, 54]. Turner et al. [46] showed that RTM moulded DCFP parts are cost effective when the annual production volume increases beyond 500 parts/annum, compared with a semi-impregnated laminate system. However, long manufacturing cycle times for conventional RTM

(approximately 30-60 minutes depending on resin system,) limit its application in the automotive industry.

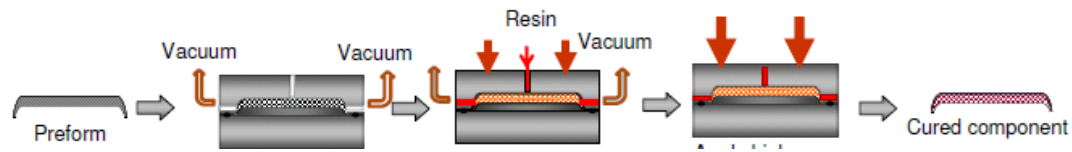


Figure 2.1 RTM moulding process: placing preform into a mould; applying optional vacuum after mould closure; injecting pre-mixed resin into the mould; component is cured in the mould before demoulding

Structural reaction injection moulding (SRIM) is another liquid moulding process similar to RTM. Highly reactive two-component polyurethane, which can be cured in seconds, is the most common resin used in SRIM [55, 56]. During the moulding process, the two components stored separately are pumped into a mixing chamber and injected into the mould cavity after impinging mixing [56]. Due to the rapid curing rate, in order to keep good infiltration, the fibre volume fraction (V_f) in SRIM typically is limited at ~30% [57]. In recent years, HP-RTM is developed by the previous SRIM developers: KraussMaffei (Germany) and Hennecke (Germany), for example. HP-RTM has been used commercially as a fast manufacturing process for high volume production of carbon fibre composites components with a V_f of 60% [49, 57-59]. HP-RTM is developed on the basis of conventional RTM, but it uses a similar resin injection system with SRIM, providing much higher injection pressures (>100bar) to fill the mould cavity quickly. In order to withstand the higher injection pressure, a high press force (typically 36,000 kN) is needed to seal the mould tool [36]. Furthermore, reactive epoxy resins have been developed to achieve short cycle times (1-10min), which reduces the cycle time by 85% compared with conventional RTM [37]. Hillermeier et al. have developed resin systems that cure within 2 minutes and

5 minutes, which are suitable for HP-RTM [60]. HP-RTM moulded parts are also reported to have low void content and excellent surface finish [48] compared to standard RTM, driving the development of suitable preforming technologies. Hence, the combination of DCFP and HP-RTM can suitably increase productivity of discontinuous fibre composites up to 100,000 ppa (assuming a 5-minute Takt time) if some of the associated challenges can be overcome.

The main problem with HP-RTM is fibre distortion - “fibre washing”, due to the high injection pressure, as shown in Figure 2.2. In addition to using advanced low-viscosity resins, attention should be paid to the binder technology used during the preforming stage. For example, the EPS620 binder made by Momentive was developed to provide strong bonding for fibres to prevent fibre washing [60]. This reactive binder fully cross-links during the preforming stage to provide a strong fibre-fibre bond. This however, can affect the ultimate composite strength, as it does not get absorbed into the bulk matrix during resin infiltration and can therefore act as a pollutant. It is unknown whether the same binder materials are suitable for discontinuous fibre composite applications and at what percentage levels they are effective.

Compression moulding is one of the fastest manufacturing processes for long fibre (>10 mm) composites production. It has been used extensively for manufacturing SMC parts within the automotive industry. The mechanical properties of carbon fibre SMC (CF-SMC) were investigated by Cabrera and Castro [61], showing that there was up to 200% improvement in tensile stiffness, compared with glass fibre SMC counterparts. However, the high cost of raw materials and the labour-intensive charge preparation step has limited the uptake of CF-SMCs for automotive

applications. Evans et al. [62] developed a system that is able to chop carbon fibre and spray resin simultaneously to make net-shaped charges. The charges are subsequently moulded by compression moulding, achieving tensile modulus and strength values comparable to the commercial systems (36 GPa and 320 MPa respectively [62] from the isotropic fibre architecture).

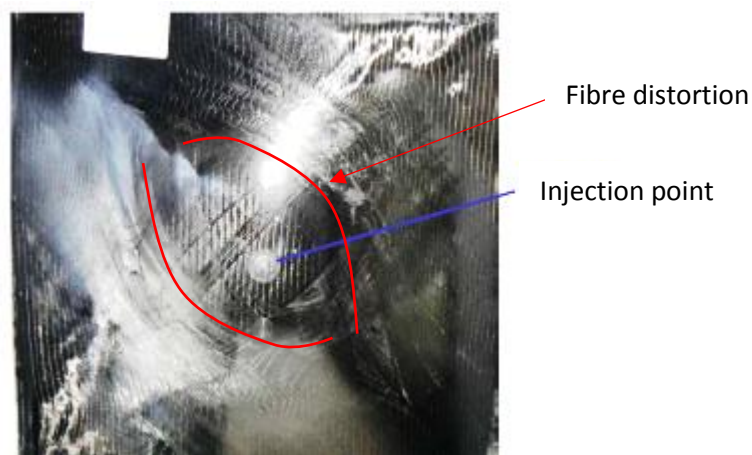


Figure 2.2 Large fibre distortion (indicated by red line) in a composites part made by HP-RTM

2.2 Factors influencing mechanical properties of DCFP components

2.2.1 Effects of fibre architecture parameters

Harper et al. [63-65] carried out a series of experiments to investigate the effects of DCFP fibre architecture parameters: tow size, fibre length, and filamentisation. The strength and modulus of DCFP parts can be enhanced in general, by using methods that improve fibre distribution, such as using fibres with smaller tow sizes, shorter fibre lengths, and high levels of tow filamentisation (fragmenting the tow to achieve

smaller filament counts). However, Jacob et al. [66] found that both strength and stiffness decreased when shorter fibre lengths were used. The authors attributed the reduction in strength and stiffness to an increase in stress raisers introduced by shorter fibres in the specimens. There is clearly a critical length for fibre bundles, but it is difficult to establish. Harper et al. [64] proposed a model based on the Kelly-Tyson model, but it has never been effectively validated. The data presented in [17] indicate that increasing fibre length from 12 mm to 29 mm results in a 19% increase in strength, but only a 4% increase in modulus.

Many studies indicate the advantage of using smaller tow sizes for improving tensile strength and modulus of discontinuous fibre composites. Smaller tows provide a more homogeneous fibre distribution, avoiding resin rich regions and ensuring a more uniform fibre volume fraction distribution across the component to provide more efficient stress transfer between the fibre bundles [17]. Larger tows containing more synchronised parallel filaments will have larger stress concentrations at the bundle ends, resulting in a negative effect on the composite strength [67]. It should be noted that smaller tow sizes are more expensive than larger tows, following a non-linear relationship as shown in Figure 2.3 [8]. Filamentisation can be used to fragment larger tow sizes to effectively create smaller tows. This has a similar effect on the mechanical properties as using smaller tow sizes, but the splitting process is not easy to control and results in lots of single filaments and very small clusters of filaments. This can create problems with preform loft (high bulk factor), which limits the maximum fibre volume fraction to approximately 30% [17].

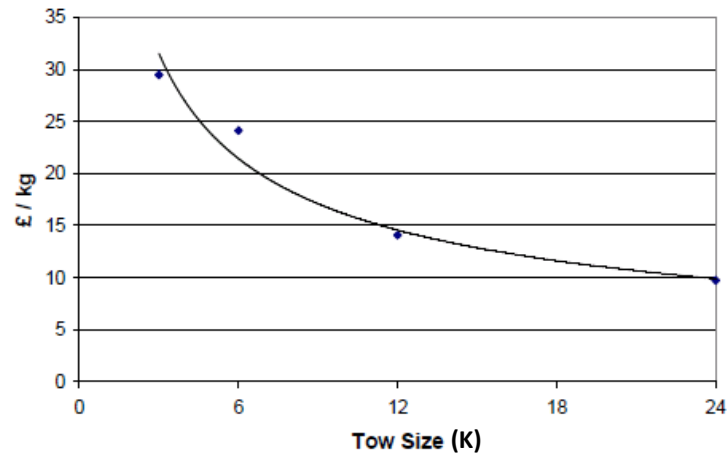


Figure 2.3 Carbon fibre cost (Toho Tenax Europe GmbH, 2003) versus tow size [8]

The effect of specimen thickness on mechanical properties has also been studied [17]. For a 24K DCFP component, when thickness increases from 1 mm to 3mm, its stiffness and strength increase by 19% and 50% respectively [17]. Increasing both specimen thickness and increasing preform areal density improve mechanical properties of composites by reducing preform variability [8].

It is clear that many previous studies tend to focus on the effects of parameters that influence fibre distribution and the cause of defects (such as stress raisers). However, the effect of the constituent materials, in particular the fibre strength and fibre modulus, on mechanical properties of moulded DCFP part has not yet been studied. This thesis aims to understand if the random rule of mixtures (ROM) is applicable for DCFP materials when using carbon fibres with a range of different stiffnesses and strengths. This study will indicate if there is a practical upper limit in terms of the fibre contribution to the ultimate composite strength.

Hybrid fibre architectures containing both carbon fibre and glass fibre offer a compromise between mechanical properties and material cost [68-71]. Glass fibres are added into carbon fibre composites to enhance failure strain and reduce material cost, while higher carbon fibre content in glass fibre composites helps improve strength and stiffness. The hybrid effect of combining M40/T300 [72] and IM7/T700 [73] (the stiffness ratio of high-modulus fibre to low-modulus fibre is between 1.6 and 1.2 respectively) has been studied for unidirectional fabrics. Higher content of high modulus fibre in hybrid composites leads to higher overall composites stiffness, and these values are in close agreement with the theoretical values predicted by rule of mixtures. However, when the high-modulus fibre content increases in the range of 25% - 50 %, the measured composite stiffness values are ~4% lower than the theoretical values. The strength of hybrid composites on the other hand, significantly decreases with increasing high stiffness fibre content due to the low failure strain [72]. The hybrid effect of using two different carbon fibre grades for random discontinuous fibre composites requires further investigation.

2.2.2 Analytical models for strength and modulus of discontinuous carbon fibre composites

2.2.2.1 Modulus

The most commonly used method for estimating the longitudinal modulus of composites is the rule of mixture (ROM), which assumes that the strain in the fibres is equal to the strain in the matrix [74]. The equation below shows the solution for the modulus of a composite containing continuous fibres:

$$E_c = V_f E_f + V_m E_m$$

Equation 1

where E is Young's modulus and V is the volume fraction, and the subscripts c, f, and m represent the composite, fibre and matrix respectively. The shear-lag model is a widely used approach for stiffness estimation, introducing a length factor (η_l) [75] to account for the discontinuous fibres and an orientation factor (η_o) [76] to account for the random orientation distribution:

$$E_c = \eta_l \eta_o V_f E_f + (1 - V_f) E_m$$

Equation 2

$$\eta_l = \frac{1 - \tanh(\frac{\varphi l}{2})}{(\frac{\varphi l}{2})}$$

Equation 3

$$\varphi = \sqrt{\frac{2G_m}{E_f \ln(\frac{R}{r})}}$$

Equation 4

$$\eta_o = \sum \alpha_i \cos^4 \theta_i$$

Equation 5

The fibre length (l), the radius (r), the shear modulus of the matrix (G_m) and the fibre packing factor (R) are considered. α_i is the proportion of fibres at orientation θ_i . For a perfectly random 2D (planar) fibre structure, the orientation factor is 0.375 [76]. When the fibre filament aspect ratio (length/diameter) is over 1000, which is the case for DCFP, the stiffness model can be simplified to the random ROM [17]:

$$E_c = 0.375 V_f E_f + V_m E_m$$

Equation 6

In the shear-lag model it is assumed that there is no tensile stress at the fibre ends, but strains of up to 0.5% have been found at fibre ends when E_f/E_m is as low as 16 [77]. However, when E_f/E_m approaches 100 (the case for carbon fibre/epoxy), the end effects can be ignored [78].

2.2.2.2 Strength

The estimation for strength is similar to the one for modulus in the form of ROM, because the stress is assumed to be linear with the strain ($\sigma = \epsilon E$). For unidirectional composites, the strength achieved when the fibre breaks is:

$$\sigma_c = V_f \sigma_f + (1 - V_f) \sigma_m^* \quad \text{Equation 7}$$

$$\sigma_m^* = \epsilon_{fb} E_m \quad \text{Equation 8}$$

Where ϵ_{fb} is the strain that causes fibre failure. However, the strength of a discontinuous fibre composite cannot achieve the value calculated by the equations above, because stress concentrations will occur at the fibre ends. Kelly and Tyson [79] proposed a length efficiency factor by introducing a critical length term. The difficulty predicting the ultimate composite strength is due to material variability and multiple modes of failure. Weibull's weakest link theory [80] can be applied to describe the strength variability:

$$F_n(\sigma) = 1 - \exp\left[-n\left(\frac{\sigma}{\sigma_0}\right)^m\right] \quad \text{Equation 9}$$

where F is failure probability of n elements under stress σ , σ_0 is the scale parameter having a relationship with material volume, and m is shape parameter which is a measure of material variability. If a material is highly variable, it will have a higher probability for failure, because its properties depend on the weakest link. Hence, for the DCFP process, improving the fibre homogeneity is important for achieving consistently high strength values.

2.2.3 Effect of binder

Ideally, binders should be able to provide good adhesion between fibre layers as well as provide dimensional control to prevent spring-back after preforming [81]. Binders are either thermoset or thermoplastic materials which appear as solids at ambient temperatures and can be easily melted by heating [81, 82]. In terms of HP-RTM, as more binders are added into preforms to prevent fibre washing-out under high pressure, high binder content may have a significant influence on mechanical properties. However, there is no literature about the effect of binder content on mechanical properties of HP-RTM parts. Hence, in this section, the effect of binder for conventional RTM parts is reviewed to get a general idea of how binders influence mechanical performance.

Generally, the effects of binder concentration on mechanical properties of a composite preform and moulded component have been widely investigated [8, 83-85]. In a previous binder study [83], the optimum content of PT 500, an powdered epoxy binder manufactured by 3M, is suggested to be in the range of 4 – 6 wt.%. For the preform with lower binder concentration (1% or 2% approximately), there is insufficient adhesion. When binder content exceeds 8 wt.%, the fabric will be too rigid and higher resin injection pressures are required for mould filling, as the pore volume of the preform is lower. Furthermore, Harper [8] carried out experiments on the investigation of binder content for DCFP. The modulus and ultimate tensile strength of moulded DCFP components were investigated, using three different types of binders and at three levels (3wt%, 6wt.% and 9wt.%). The results indicated that both composite strength and modulus were improved when binder content increased from 3wt.% to 6wt.%, however there was a reduction in properties when the binder content increased further to 9wt.%. Hillermeier and Seferis [84]

investigated the effect of binder distribution on mechanical properties of moulded parts, by comparing the effect of different application methods. Compared to manual applying binders by using a sifter, the nozzle-sprayed binders provided better interlaminar fracture toughness (30% increase) and interlaminar shear strength due to better binder distribution.

2.3 Conclusions

DCFP is a cost effective manufacturing process with a ~5 minutes cycle time and generates ~5% material waste, so it is suitable for the automotive industry for high volume production. Whilst the tensile strength of DCFP is only approximately half of continuous fibre counterparts, the modulus is approximately 80%. One possibility for increasing the mechanical properties of DCFP parts further is to increase the stiffness and strength of the reinforcing fibre, but this has an obvious impact on the component cost. This thesis will find the cost/performance balance for a range of carbon fibre types, ranging from intermediate modulus to high modulus variants. The literature review also suggests that blending different grades of fibre to create a hybrid fibre architecture may have a positive effect on the tensile stiffness and strength of the DCFP composite. HP-RTM is a rapid moulding technology, which may work with DCFP to further improve production rates. However, DCFP preforms need to withstand the high injection pressures to avoid fibre washing, whilst ensuring the binder material does not have a negative effect on the mechanical properties.

Chapter 3 Experimental methodology

The facility and methodology used to develop DCFP preforms for both 2D and 3D structures are introduced. Additionally, the characterisation methods for dry preform and moulded plaques are presented.

3.1 Preforming process development

DCFP preforms were produced using the facility (Figure 3.1) developed at the University of Nottingham. Fibre tows were chopped into 22.5mm and 45mm long bundles using the chopping system mounted on a 6-axis Fanuc robot (Figure 3.2). Fibres were sprayed onto a perforated tool with powder binder. Under the tool, a large fan is used to provide a pressure gradient (0.05 bar) to retain the fibres on the tool.

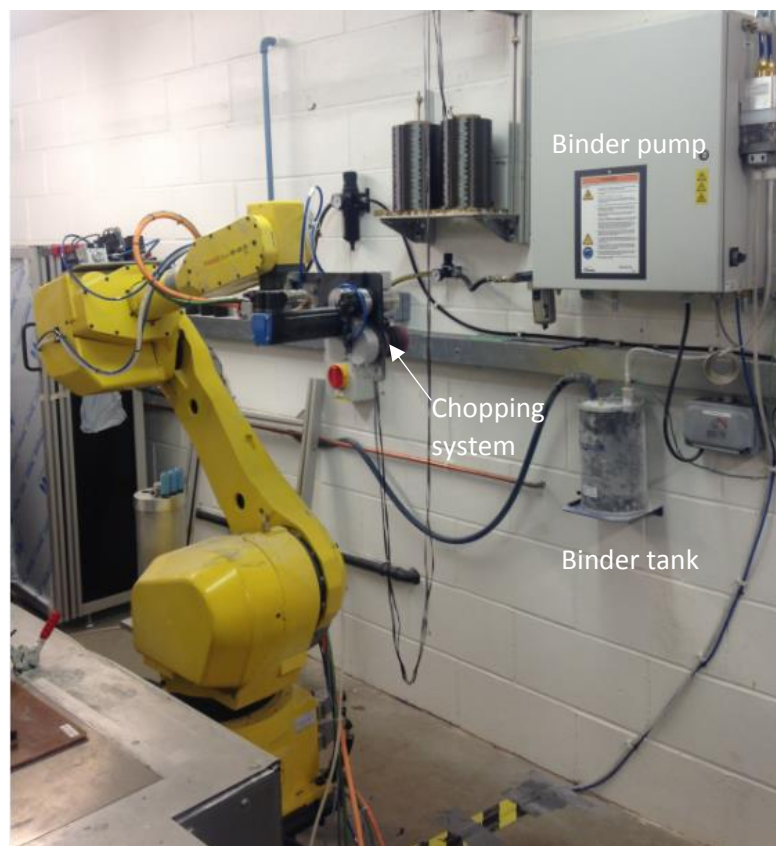


Figure 3.1 FANUC robot with fibre chopping system and binder spraying system

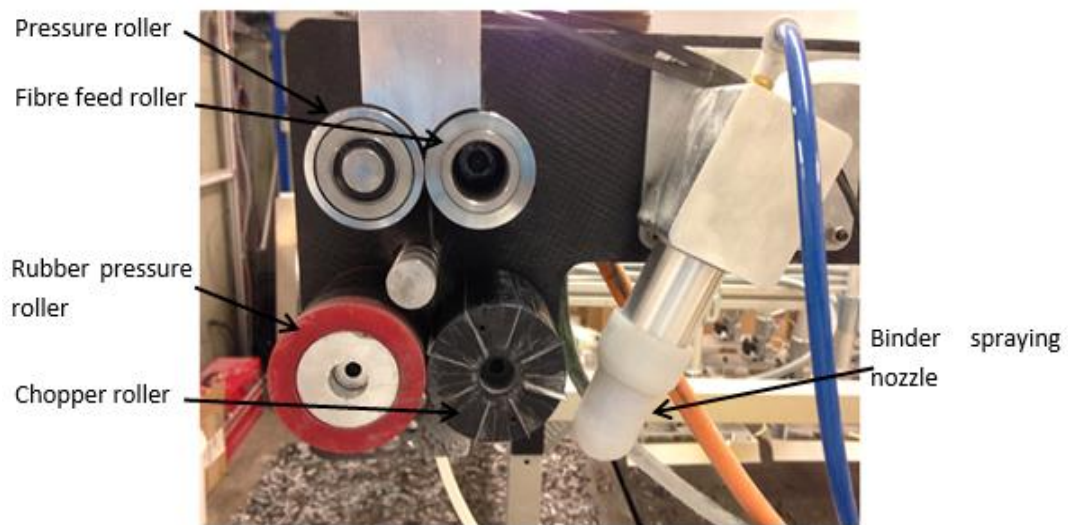


Figure 3.2 Fibre chopping system and binder spray nozzle

The fibre deposition process was first characterised in order to understand perform variability, using the methodology below:

- Fibres were sprayed along two directions (marked as X and Y directions in Figure 3.3): X: robot direction same as chopper's tangential direction; Y: robot direction perpendicular to chopper's tangential direction.
- A photo was then taken of the preform, in order to measure the path bias distance between the centre line of the actual preform path and the designed robot path (green line).
- Two tool centre point (TCP) heights were selected: 50 mm and 200 mm.



Figure 3.3 Fibre deposition characterisation along two directions (X and Y)

For the work in this thesis, robot paths were programmed for a 2D flat preform (700mm*600mm) and a more complex 3D automotive structure, to investigate the mechanical properties of moulded DCFP components and to demonstrate the effectiveness of the DCFP process respectively. The tools used for manufacturing the 2D and 3D preforms are shown Figure 3.4.

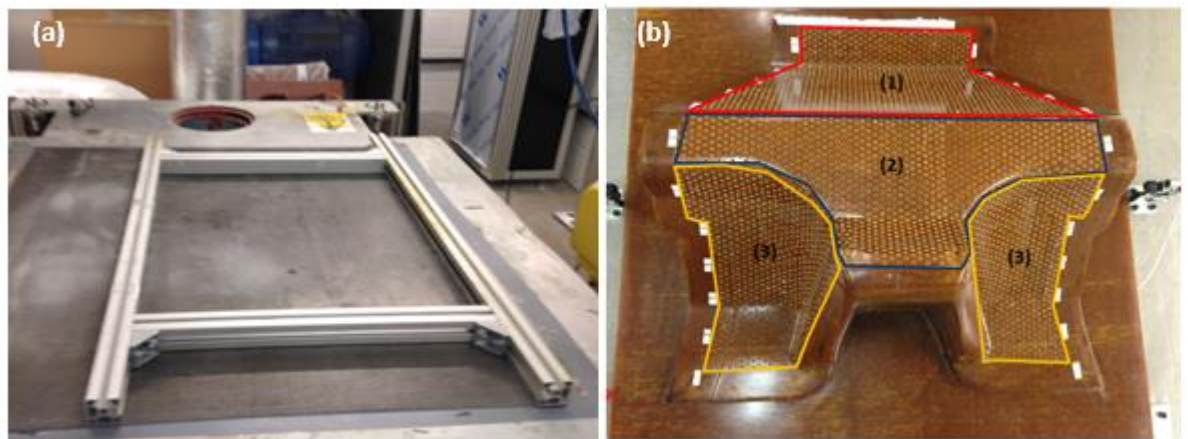


Figure 3.4 (a) Frame used to make 2D 700mm*600mm preforms; (b) the 3D tool used for 'T-shirt' preforms

3.2 Characterisations

3.2.1 Tensile test of dry DCFP preforms

Tensile properties of dry rectangular DCFP preforms (T700 carbon fibre) with different binder contents (5wt.%, 10wt.%, and 15wt.%) and types (EPS620-Reactive and EP05390-Unreactive) were tested, according to ISO3342:1995. Both binders are provided by Momentive. During the manufacturing process of DCFP preforms, two spacers (1.7mm and 2.5mm thick) were placed between the press platens to control the thickness of preforms, to represent different fibre fractions at V_f 50% and V_f 34%.

The details of the manufacturing parameters are listed in Table 3.1.

Table 3.1 The manufacturing details of the dry DCFP preforms (T700) used for areal mass variability measurement

Binder types	Binder content	Preform area density	Fibre length & tow size	Spacer used	Consolidation temperature and compaction pressure	Preform size
EPS 620	5wt% 10wt% 15wt%	1200 gsm	45mm 12K	1, 1.7mm-thick strips 2, 2.5mm-thick strips	160°C 0.15 MPa	700mm × 600mm
EP 05390	5wt% 10wt% 15wt%	1200 gsm	45mm 12K	1, 1.7mm-thick strips 2, 2.5mm-thick strips	90°C 0.15 MPa	700mm × 600mm

In order to conduct dry preform tensile tests, preforms were cut into 280mm × 115mm pieces. For each type of preform, 10 samples were tested with an initial distance between the 2 grips of 200mm, using an INSTRON 5966 testing machine shown in Figure 3.5. The tensile force was recorded by a 5KN load cell attached to the crosshead of the testing machine. The displacement measurement was also

recorded from the crosshead of the machine, due to the low compliance of the preforms. The test speed was 10mm/min. No slippage of the samples was observed near the two grips.

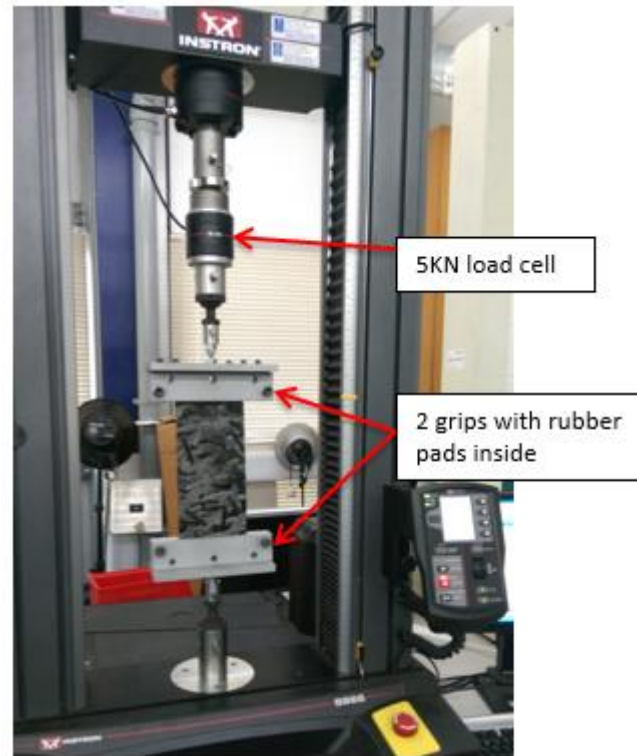


Figure 3.5 Dry DCFP preform testing rig and machine

3.2.2 Mechanical testing

Three mechanical testing methods were used for the moulded plaques: tensile test, compression test, and Charpy impact test (Table3.2).

Table3.2 Test methods used

Test method	Test standard	Specimen size
Tensile	BS EN ISO 527-4:1997	250mm × 25mm × 2.7mm
Compression	ASTM D3410-03	150mm × 25mm × 2.7mm
Charpy impact	BS EN ISO 179-1/2001	80mm × 10mm × 2.7mm

Both tensile and compression tests of moulded plaques were conducted on an INSTRON 5578 universal testing machine at a test rate of 1 mm/min. Tensile testing was performed according to ISO 527-4: 1997. Aluminium tabs (50 mm × 25 mm × 1.5 mm) were glued at each end of the specimen and on both sides to prevent slippage and minimise stress concentrations in the jaw region. The gauge length of the specimen was 150 mm. All specimens were painted matt white and then speckle coated to enable a non-contact video gauge to be used (IMETRUM Universal Video Extensometer). The strain was calculated using the IMETRUM Video Gauge™ analysis software. A 50 kN load cell was used to record the applied load during the test. Straight-sided specimens were used rather than dog-boned specimens, as failure generally occurred within the gauge length of each sample. These materials are notch insensitive [86] and are therefore more likely to fail due to the inherent stress concentrations within the material rather than due to stress raisers in the grip area.

Compression tests were conducted according to ASTM D3410-03 standard. All specimens were also painted matt white and then speckle coated to enable the same video gauge system used in the tensile test. The IMETRUM Video Gauge™ analysis software was also used to calculate strain. Each specimen had a gauge length of 12.7 mm between the parallel clamps.

An Avery Denison Charpy impact test machine (Figure 3.6) was selected to carry out the flatwise impact test on un-notched specimens. Specimens were cut, polished and tested according to ISO 179-1/1f. “Normal Flatwise” flexural Charpy impact tests (ISO13802) were performed using a strike velocity of 3.46m/s. The results from this

test provided a comparative quantitative measure of toughness, indicating the energy required to fracture each material.



Figure 3.6 Avery Dension Charpy impact test machine

Two different studies were performed in this thesis to determine the mechanical properties of moulded DCFP plaques. In the first study plaques moulded by HP-RTM (T700 DCFP, 12K-45mm-EPS620-10wt.%) were selected to conduct tensile tests to investigate the inter- and intra-plaque variation for DCFP properties. For each plaque, 20 tensile specimens were prepared: The longitudinal direction of 10 specimens (marked as 0 deg) was parallel to the flow direction during resin injection, whilst the other 10 specimens were cut transverse to the flow direction (marked as 90 deg), shown in Figure 3.7. For the second study, 5 specimens were prepared and tested for each of the three mechanical tests mentioned above, to investigate the effects of fibre properties, binders, and moulding processes on the mechanical properties of DCFP.

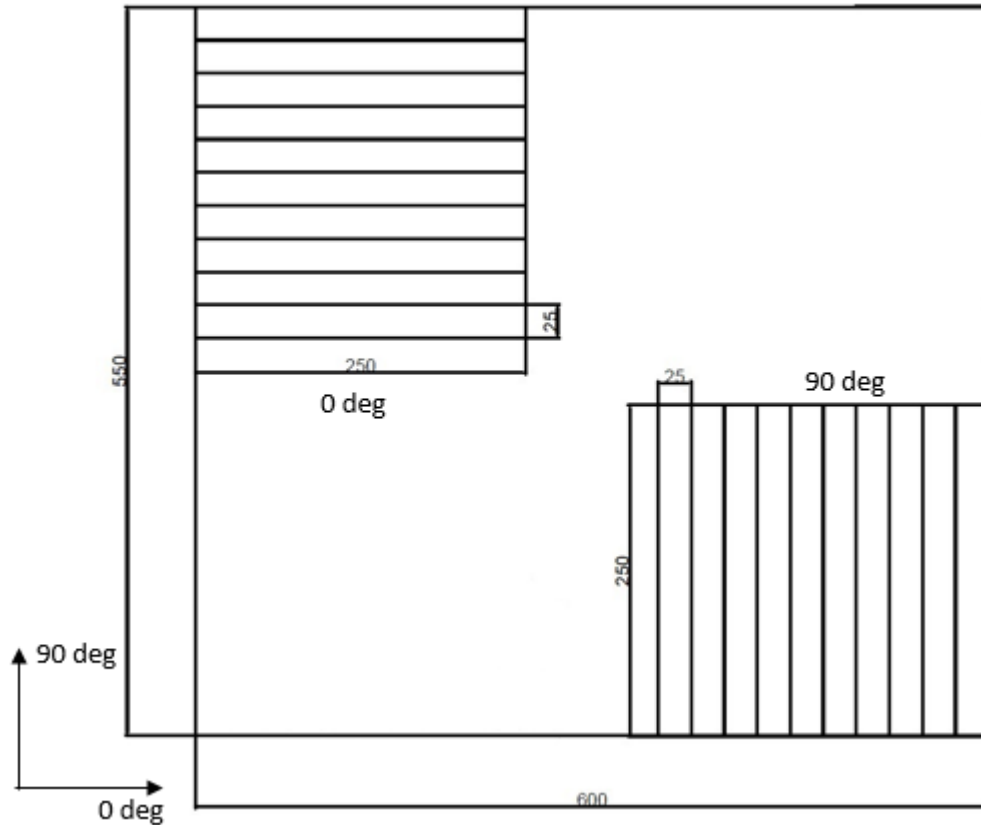


Figure 3.7 Cutting plan of the HP-RTM moulded DCFP (T700 DCFP, 12K-45mm-EPS620-10wt.%) to investigate the inter- and intra-plaque variation

3.2.3 Void analysis

Void analysis specimens were taken from ends of compression test specimens, which were clamped in the jaws and were consequently a suitable distance from the failure site. Specimens were mounted in polyester casting resin and then polished using silicon carbide paper (P240, P400, P800, P1200, P2500, and P4000) and a 1 μm alumina powder paste. A Zeiss AxioLab optical microscope with $\times 5$ magnification lens and QImaging QICAM 12-bit digital camera were used to take micrographs of cross-sections of the specimens. All micrographs were processed using ImageJ to determine void locations, by applying a grey-scale threshold. Void fraction was measured by calculating the area percentage in each image.

Chapter 4 Manufacturing process studies

This chapter introduces the optimisation process of DCFP preforms to achieve uniform fibre distribution for both 2D and 3D structures. In order to understand the level of in-plane isotropy for 2D DCFP preforms, the mechanical properties of the moulded DCFP plaques are investigated. The effects of binder and moulding process (RTM, HP-RTM and compression moulding) on mechanical properties of DCFP plaques are also investigated.

4.1 2D Preforming path studies

4.1.1 Fibre deposition process characterisation

Figure 4.1 shows fibre distributions in the X and Y directions, as sprayed by the robot mounted chopper gun, at two Tool Centre Point (TCP) heights. The spray pattern is wider when the robot is travelling in the X direction compared to the Y direction. This bias increases from 70 mm to 130 mm (Table 4.1) when the TCP height increases from 50 mm to 200 mm. No path bias was observed in the Y direction for either TCP height. The path bias is caused by fibre deposition angle (θ), shown in Figure 4.2. The chopped fibre tows do not fall vertically onto the metal screen due to the inertia from the chopper rollers. Furthermore, by using the higher TCP, the width of the fibre deposition path in the X and Y directions increases by 70% (from 130 mm to 240 mm) and 60% (from 100 mm to 160 mm) respectively, as shown in Table 4.1.

Reducing the TCP height is an effective way to reduce the path bias in the X direction. In addition, the reduced path width improves the preforming resolution, giving more precise control over where fibres land on the tool. However, when the TCP height is 50 mm (Figure 4.1 (a)), the chopped fibres cluster along the centreline in the Y

direction, which influences fibre coverage. Therefore, during the optimisation of the 2D preforming process, the path bias must be compensated for in the robot path design by shifting the tool centre points in the X and Y axis directions accordingly (Figure 4.3), whilst achieving a good preforming resolution and maintaining good fibre coverage, by adjusting the path offsets and the TCP height.

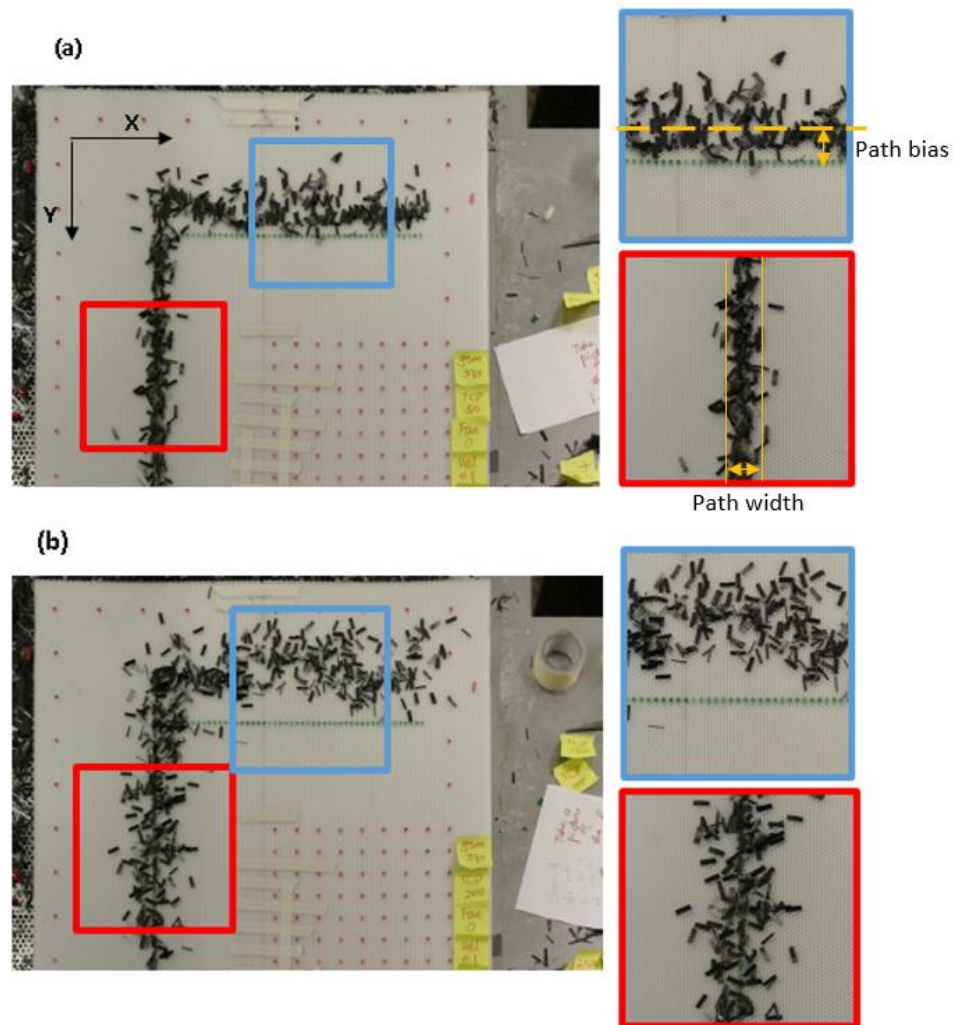


Figure 4.1 Fibre distributions at X and Y directions at two TCP height: (a) 50 mm (b) 200 mm

Table 4.1 Fibre deposition path bias and width at X and Y directions with different TCP height

TCP height	X direction		Y direction	
	Path bias	Path width	Path bias	Path width
50 mm	70 mm	130 mm	0 mm	100 mm
200 mm	130 mm	240 mm	0 mm	160 mm

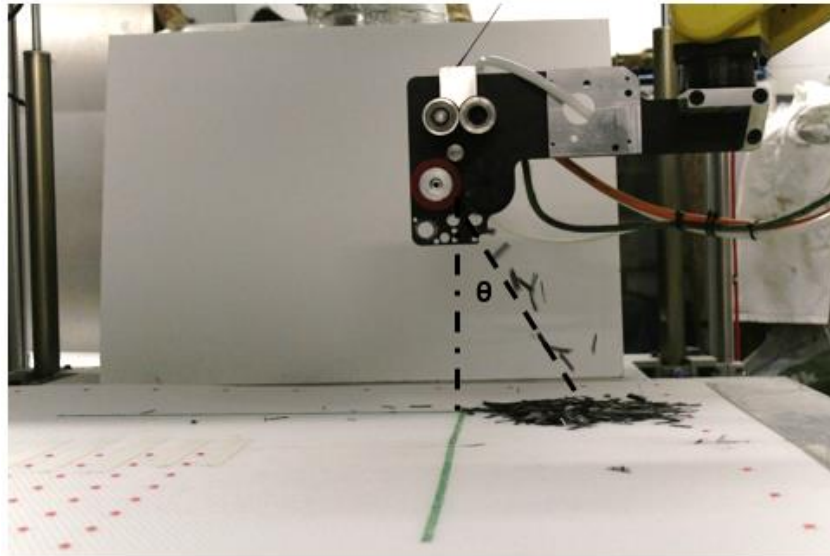


Figure 4.2 A typical fibre deposition path after chopping gun

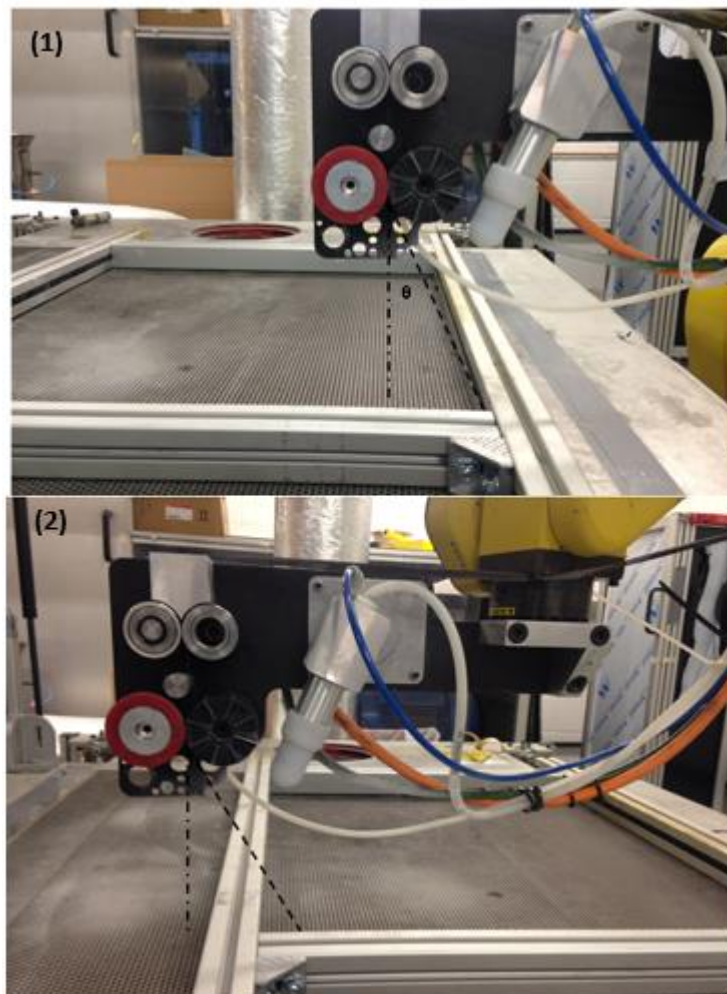


Figure 4.3 Fibre falling off angle and compensation positions of chopper gun at the right edge (1) and left edge (2) of the frame to make sure fibres are deposited with the frame

4.1.2 2D preforming process

Two orthogonal spray passes were conducted to improve the homogeneity of the sprayed preforms, based on the areal mass variability study conducted by Harper et al. [63]. Each layer had a linear sweep offset of 50mm, as shown in Figure 4.5. Following fibre deposition, preforms manufactured with reactive binder (EPS620) were consolidated at 160°C for 3 minutes under a pressure of 1.5 bar, before being cooled to room temperature. Preforms manufactured with the non-reactive binder were consolidated at 90°C for the same duration at the same pressure.

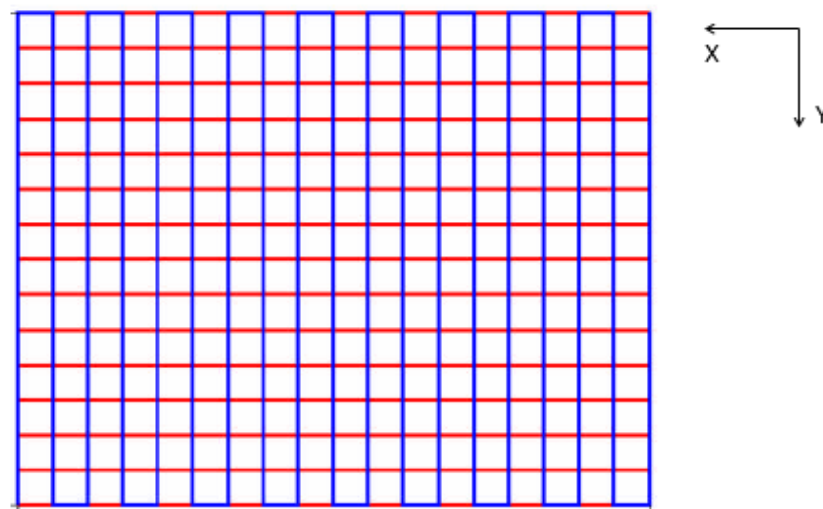


Figure 4.4 Schematics of fibre deposition strategy: east/west pass and north/south pass

Before characterising the mechanical performance of DCFP components, it is important to ensure that the robot path is able to manufacture preforms with low areal mass variability, as variable preforms result in locally variable mechanical properties. Areal mass measurements were conducted to evaluate the fibre distribution as many as the modified preforming path can create a preform with a mass variation of < 5%.

The areal mass variability was measured for each preform by weighing small coupons. For 2D preforms, 700 mm × 600 mm preforms were stamped into 50 mm × 50 mm squares and weighed using a balance. The areal mass distribution was plotted from these measurements, which was used to adjust the robot path programme to reduce variability. The adjustments in the path offsets and tool centre point (TCP) height of the initial and modified robot paths are listed in Table 4.2.

Table 4.2 Preforms and the corresponding modification information of robot path

Preform	Preform information	Adjustment
Initial	700*600mm fibre length 45mm EPS620 (5 wt.%)	
Modified	700*600mm fibre length 45mm EPS620 (5 wt.%)	<ul style="list-style-type: none"> • X coordinate of the robot path was shifted by -30mm • The Y coordinate was shifted by +45mm • TCP height in the Z direction was reduced by 80 mm

4.1.3 Areal mass variability measurement

The areal mass variability measurement results are illustrated in Figure 4.5 to Figure 4.8 and Table 4.3 to Table 4.4. In Figure 4.5 and Figure 4.7, areal mass distributions are plotted from the measurement of 50mm × 50mm coupons from two 700mm × 600mm preforms. The target areal density of carbon fibre in the measured preforms was 1200gsm, so the mass for each 50mm × 50mm coupon (including 5wt.% EPS620 binders) is 3.1g. A 5% error in areal mass was considered to be acceptable in this work, therefore the mass of each coupon was expected to be in the range of 3.0 – 3.2g. Based on the results of areal mass variability measurement for the original robot path programme, it can be seen that many regions along the bottom and left edges of the preform do not meet the areal mass target. In addition, the global

average mass does not meet the target value for any of the preform sizes studied. (indicated by red frames in Figure 4.5). By comparing mass measurements from the original robot path listed in Table 4.3, the modified robot programme helps reduce the intra-preform mass variation to 3% (Table 4.4), due to shifting the robot path, adjusting the TCP of the robot in X, Y, and Z coordinates, and an increase in the chop speed to compensate for fibre loss caused by fibre slippage between the feed rollers. Details of the adjustments made are listed in Table 4.2. More of the 50mm × 50mm coupons have a mass within the acceptable range (Figure 4.7), which means that the average mass of the preform is close to the target. Based on the results in Table 4.4, only the average mass of the 400mm × 300mm preform has an error of 3%.

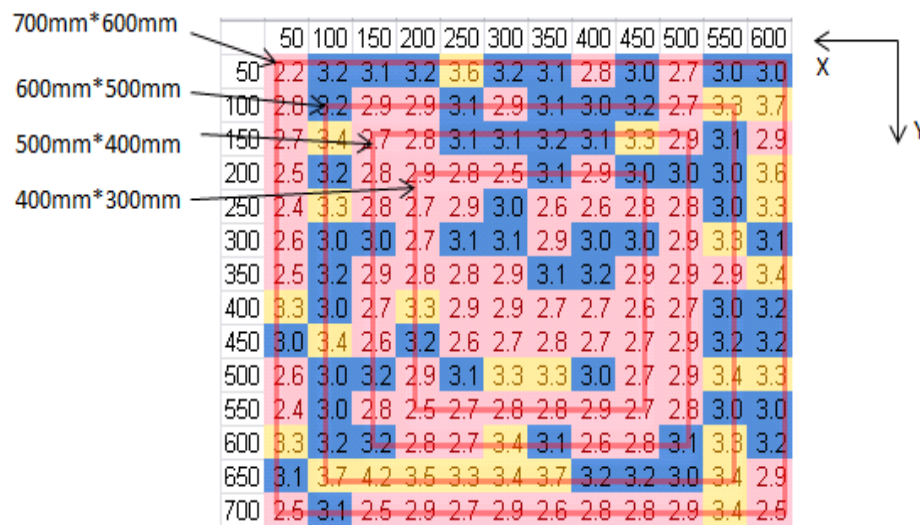


Figure 4.5 Mass distribution of the 700mm×600mm preform made by unmodified robot path

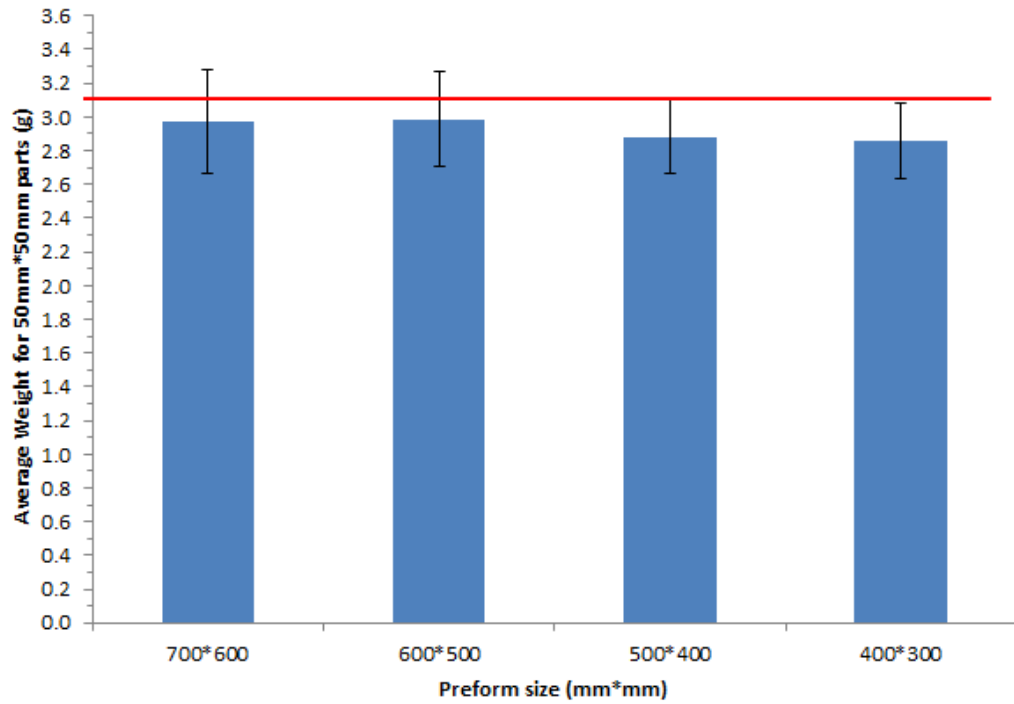


Figure 4.6 The profile of average mass of 50mm×50mm parts at different sizes for 700mm×600mm preform made by unmodified robot path

Table 4.3 Standard deviation and error to the target of the average mass of 50mm×50mm parts at different sizes for the 700mm×600mm preform made by unmodified robot path

	Target mass (g)	700mm×600m m	600mm×500m m	500mm×400m m	400mm×300m m
Average mass (g)	3.1	3.0	3.0	2.9	2.9
Standard deviation (COV)		0.31 (10%)	0.28 (10%)	0.22 (8%)	0.22 (8%)
Error to target		3%	3%	6%	6%

	50	100	150	200	250	300	350	400	450	500	550	600
50	2.9	3.0	3.4	3.2	3.3	3.1	3.2	2.9	3.0	2.8	3.1	3.1
100	3.0	3.2	3.0	3.1	3.1	3.0	3.0	3.0	3.0	3.0	3.0	3.3
150	2.8	3.1	3.0	2.9	3.0	3.0	2.9	3.1	3.0	3.1	3.0	3.1
200	3.0	3.1	3.2	3.1	3.0	3.0	3.2	3.1	3.0	3.2	3.2	3.4
250	3.1	3.0	3.2	3.0	2.9	3.1	3.2	3.0	2.9	3.2	3.1	3.3
300	2.9	3.1	3.0	3.0	2.9	3.0	3.1	2.9	3.1	3.3	3.1	3.2
350	3.0	3.0	3.1	3.0	3.1	3.0	3.0	3.0	3.1	3.0	3.0	3.4
400	2.8	3.1	3.1	2.8	2.9	3.0	3.0	2.9	3.1	3.0	2.9	3.2
450	3.0	3.1	3.2	3.1	3.1	3.0	3.2	3.1	3.0	3.0	3.2	3.3
500	2.9	2.9	3.0	2.9	3.0	3.0	3.3	3.0	2.9	3.0	3.3	3.2
550	3.0	3.2	3.0	3.0	3.1	3.0	2.9	3.1	3.0	3.0	3.2	3.4
600	2.9	2.8	3.0	2.9	3.0	3.0	3.2	3.0	3.1	3.0	3.0	3.2
650	3.1	3.1	3.2	3.3	3.2	3.3	3.3	3.1	3.0	3.2	3.2	3.3
700	2.9	3.0	3.1	3.0	3.2	3.0	3.2	3.1	2.9	3.0	3.3	3.0

Figure 4.7 Mass distribution of the 700mm×600mm preform made by modified robot path

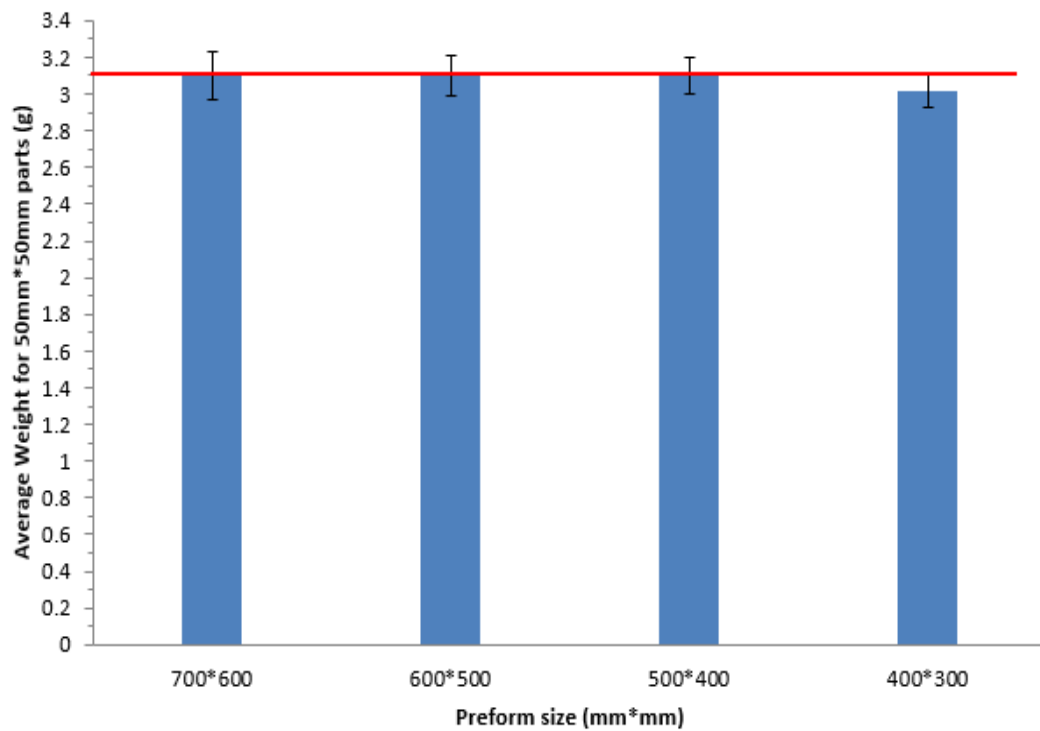


Figure 4.8 The profile of average mass of 50mm×50mm parts at different sizes for the 700mm×600mm preform made by modified robot path

Table 4.4 Standard deviation and error to the target of the average mass of 50mm×50mm parts at different sizes for the 700mm×600mm preform made by modified robot path

	Target mass (g)	700mm×600mm	600mm×500mm	500mm×400mm	400mm×300mm
Average mass (g)	3.1	3.1	3.1	3.1	3.0
Standard deviation (COV)		0.10 (3%)	0.11 (3%)	0.10 (3%)	0.10 (3%)
Error to target		0%	0%	0%	3%

4.2 Study of in-plane isotropy of 2D DCFP composites

The last section showed that the fibre deposition path developed in this work can achieve good fibre distribution (3% local variation in areal mass). This section confirms whether the randomly distributed DCFP preforms is isotropic by conducting tensile tests at 0° and 90°. The difference in mechanical properties among three moulded plaques is also studied.

Both Figure 4.9 and Figure 4.10 show the results of the tensile tests for the HP-RTM moulded T700 12K DCFP-45mm-EPS620-10wt.%. From Figure 4.9 it can be seen that although the average tensile strengths of samples from 3 moulded plaques at two directions have a slight variation, if each individual test point is plotted (Figure 4.10), 75% of the points are located within the range of the overall standard deviation (dashed lines). Furthermore, for the points outside of the overall standard deviation range, there is no clear indication to suggest why the tensile strengths are so variable for these coupons. This random distribution of tensile strengths reflects the inherent variability for these DCFP preforms. Since the intra-plaque coefficient of variation for this DCFP variant (8.0%) is higher than the inter-plaque variation (3.0%), the

mechanical properties of a single moulded DCFP plaque are representative for this material.

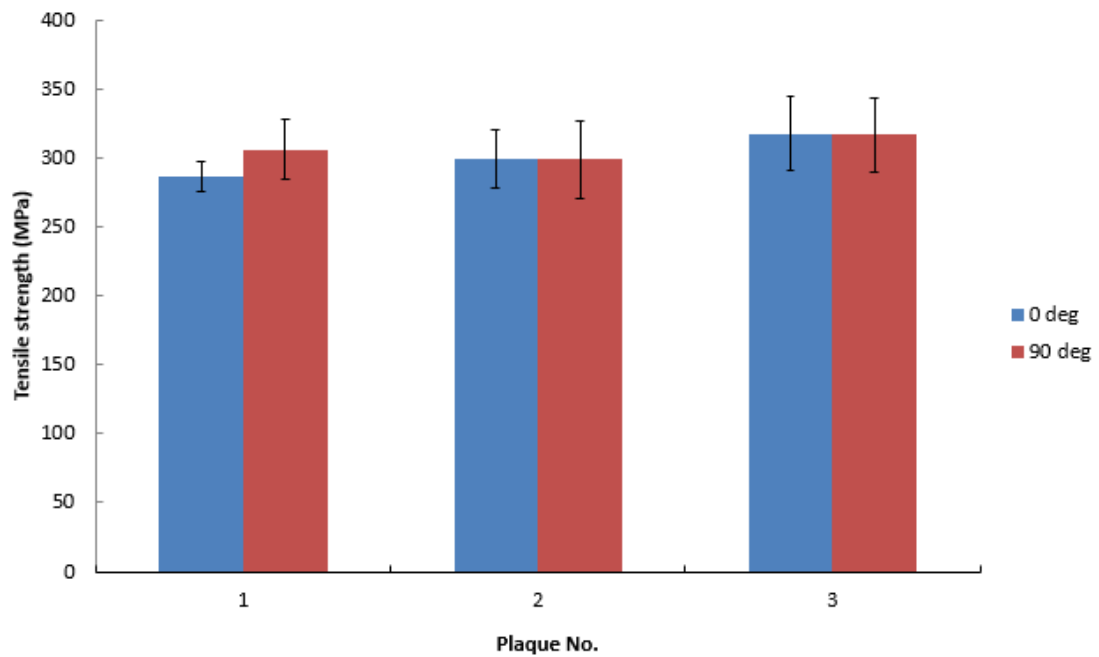


Figure 4.9 Average tensile strengths of 3 HP-RTM moulded T700 12K DCFP parts (45mm-EPS620-10wt.%) at two directions

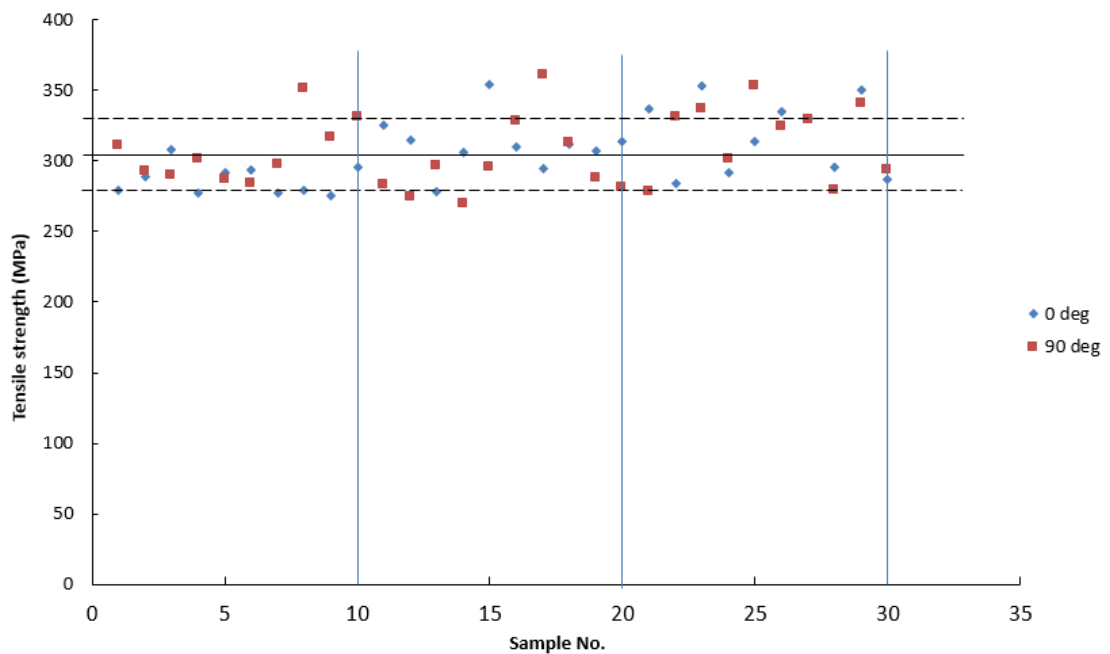


Figure 4.10 Tensile strength distribution of each HP-RTM moulded T700 DCFP specimen (45mm-EPS620-10wt.); Average strength (solid line), standard deviation range (dash line).

4.3 3D T-shirt preform

4.3.1 Preforming process development

A robot path programme was also developed for a 3D structure, based on the preforming system and fibre deposition strategy used for the 2D preform. The 3D structure is referred to as the T-shirt preform due to its shape. The optimisation of the T-shirt preform was conducted as follows:

- 1) Robot reachability test. From Figure 3.4 (b), it can be seen that several regions on the 3D mould have steep sides. Therefore, the location and orientation of the 3D mould were adjusted to achieve the most suitable position for the movement of the robot and to ensure that each corner could be reached. The TCP should be orthogonal to the surface of the tool at all times. When TCP reaches to a position where 10 mm higher than the tool surface is, it should have 10mm free space to any direction.
- 2) Robot path design. When the reachability test was completed, the robot path programme for the 3D structure was produced and modified to achieve good fibre coverage on the 3D mould. Based on the experience learnt from 2D preforming, at narrow and steep regions, low TCP height should be used to improve the accuracy of preforming, while on large surface, high TCP height can be used to increase coverage of fibre for a single sweep to reduce manufacturing cycle. Currently this can only be achieved by visual inspection to determine fibre coverage. Many pictures were taken at different angles after spraying one layer of fibre on the mould to check for large unreinforced regions without fibre. The robot path was modified by adjusting the

coordinates, the angle of the robot arm and the TCP height. This checking process was conducted over and over again until a good coverage was achieved.

- 3) Areal mass measurement. After chopped fibres were deposited with a binder on to the 3D tool with perforated holes, a flexible silicone cover was placed over the preform. Twelve infra-red heating elements located above the tool were used to heat the preform, as shown in Figure 4.11. An air pressure of 0.05 bar was applied, using a fan to consolidate the preform. After consolidation, the preform was de-moulded from the tool. The moulded preform was transferred to a trimming jig and a rotary blade was used to cut off excess fibre around the edge, as shown in Figure 4.12. Areal mass measurements were taken to compare the local mass of the 3D preform against the global target value. Step 2 was repeated until the local mass variability was less than 5%.

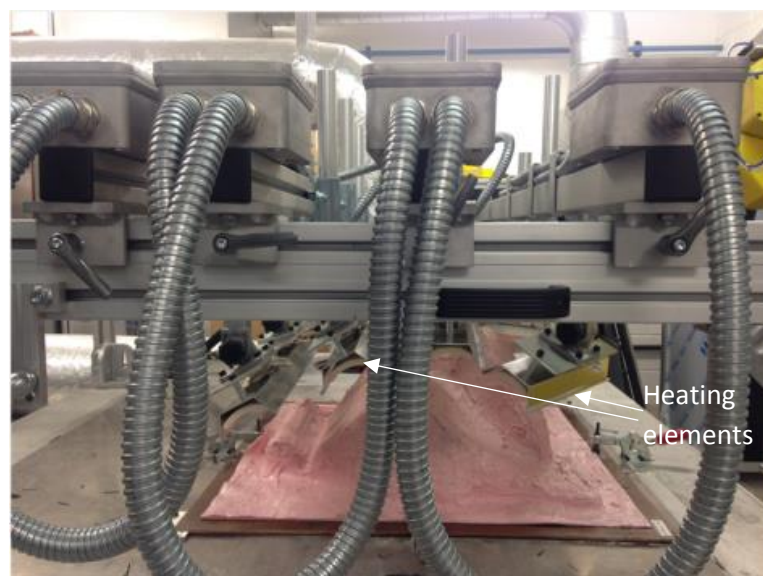


Figure 4.11 Infra-red heating elements setup for 3D T-shirt preforms

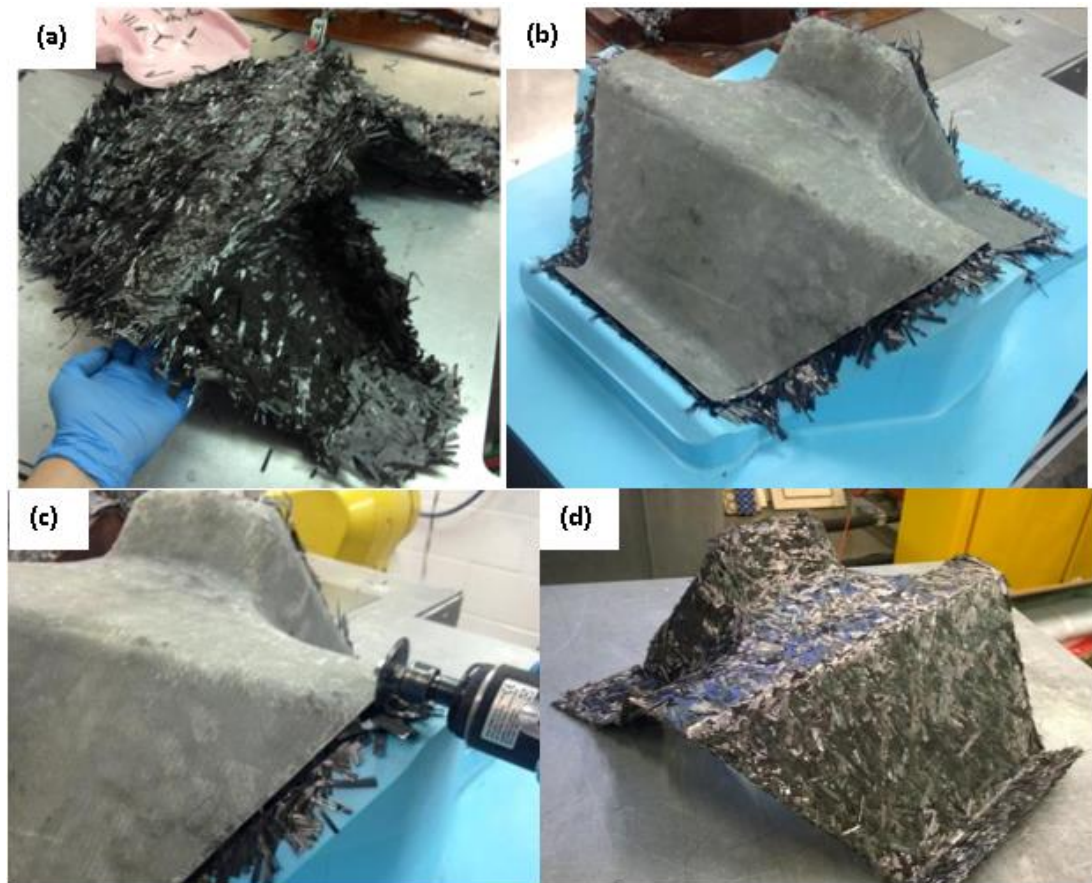


Figure 4.12 T-shirt preform trimming process: (a) Raw preform; (b) Rigid shell placed on; (c) Rotor blade trimming preform edges; (d) Trimmed preform

4.3.2 Areal mass variation measurement of 3D preform

There are more challenges to overcome for manufacturing a 3D preform. Due to the presence of near-vertical sides, it is difficult for the chopper gun to always remain orthogonal to the tool surface and the fibres are likely to be influenced by gravity and will fall off the tool. Male corners on a 3D mould are also problematic, as fibres slip to lower adjacent regions, whilst female corners are likely to collect falling fibres from adjacent slopes, leading to higher than expected fibre volume fractions. Hence, areal mass variation measurements are also important for confirming the quality of 3D preforms.

The results of the mass variation measurements for the 3 main parts of the 3D preform are shown in Table 4.5, Table 4.6, and Figure 4.13. It can be seen that the 3D preform manufactured by using the modified robot programme has more uniform mass distribution and both the weights of its 3 main parts and 50mm×50mm pieces have a difference of <5% (reduced from over 10%) to the target values, compared with the initial preform. It should also be noted that the local mass distribution may vary considerably compared to the design values near the boundaries where the shape changes or the areal mass locally changes (e.g. the part(2)-(3*) boundary and the part(3*)-(3) boundary). For instance, when spraying chopped fibre bundles along the upper and lower boundaries of part(3*), fibre bundles inevitably fall into part(2) and part(3), because the fibre spray cone is large compared to those boundary features, even though the robot paths have been compensated. When the TCP height was down to 50 mm, the fibre preforming path can still be up to 130 mm wide (Table 4.1).

Table 4.5 Mass distribution of 3 main parts in 3D preforms

Preform mass distribution					
Region	Areal mass (gsm)	Binder content (wt.%)	Target weight (g)	Initial (g)	Modified (g)
1	1772	10	164.4	135.5	162.3
2	1772	10	89.8	108.1	91.2
3*	3150	10	98.6	109	99.5
3	1378	10			
Total			451.3	461.6	452.5

Table 4.6 Mass distribution of 50mm×50mm pieces in 3D preforms

Mass distribution of 50mm×50mm pieces					
Region	Areal mass (gsm)	Binder content (wt.%)	Target weight (g)	Initial (g) (COV)	Modified (g) (COV)
1	1772	10	4.85	4.43 (6.1%)	4.82 (4.1%)
2	1772	10	4.85	5.25 (26.1%)	4.75 (4.6%)
3*	3150	10	8.70	7.30 (12.2%)	8.62 (5.1%)
3	1378	10	3.85	4.67 (11.3%)	3.73 (4.9%)

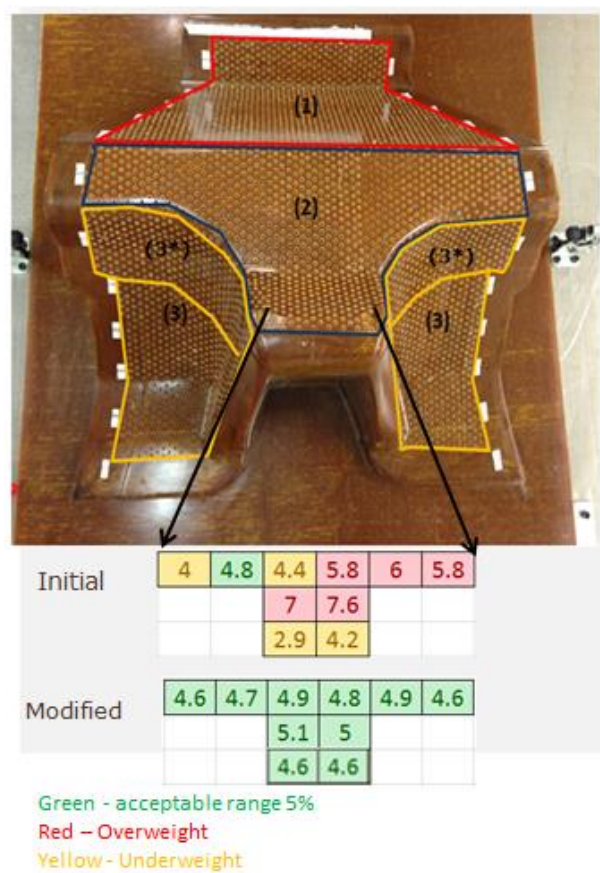


Figure 4.13 Schematic of mass distribution in part (2)

From the two sections above, the DCFP process developed in this work produced preforms with low mass variability (< 5%) for both 2D and 3D geometries, and there was no significant difference in mechanical properties among moulded DCFP parts having the same fibre and binder settings, which indicates that the manufacturing

process is reliable and repeatable. It also shows that the fibre deposition process produces an isotropic fibre distribution with no bias. Hence, this process was used to conduct the investigations of the effects of binder and moulding process on mechanical properties of DCFP in the sections below.

4.4 Effects of binder on structural integrity of the DCFP preform

A separate study was conducted to investigate the effect of binder material on the strength of dry DCFP preforms and also the mechanical properties of moulded components. Two different binders were used to create DCFP preforms for HP-RTM; Momentive EP05390 and EPS620. Momentive EP05390 is an unreactive binder with a softening temperature of 80 – 90 °C. This binder is commonly used for preforming applications and can be reheated to allow for easy shaping and hot-melt bonding to adjacent plies. Momentive EPS620 is a reactive binder that was developed for more demanding applications, where stronger fibre preforms are required to prevent fibre deformation during processes such as HP-RTM. This binder also softens between 80 – 90 °C and is reversible at this temperature. However, cross-linking occurs if the temperature is increased beyond 100 °C. For example the binder fully cross-links in 20 seconds when cured at 160 °C. EP05390 and EPS620 are referred to as 'Unreactive' and 'Reactive' throughout this work. Three binder levels (5 wt. %, 10 wt.% and 15 wt. %) were selected for both types of binder to investigate the effect on the dry preform strength. Two different binder levels (5 wt. % and 10 wt. % of EPS620) were used to investigate the influence of the binder level on the tensile properties of moulded DCFP composites.

Figure 4.14 shows the dry preform strength as a function of binder content for both the Reactive (EPS620) and Unreactive binder (EP05390) systems. The dry preform tensile strength gives an indication of how the preform will behave during the resin injection stage in a HP-RTM process, as the preform strength is dependent on how well the binder adheres the fibre together at the local fibre-fibre contact points. The ultimate load for the Unreactive system follows a linear trend for increasing binder levels, increasing from 102 N to 388 N between 5% and 15% loadings. The ultimate loads for the Reactive system are generally much higher than for the Unreactive system, ranging from 210 N to 1625 N for the same binder levels. Micrographs in Figure 4.15 indicate that the binder was more homogeneously distributed for the Reactive system, as the particle size ($\sim 90\text{ }\mu\text{m}$) was smaller in comparison to the Unreactive system ($\sim 150\text{ }\mu\text{m}$). Figure 4.15 (a) also shows that the Unreactive binder forms concentrated circular droplets once melted, whereas the Reactive binder tends to flow further along the fibre boundaries and can penetrate deeper within the tow to encapsulate more of the filaments.

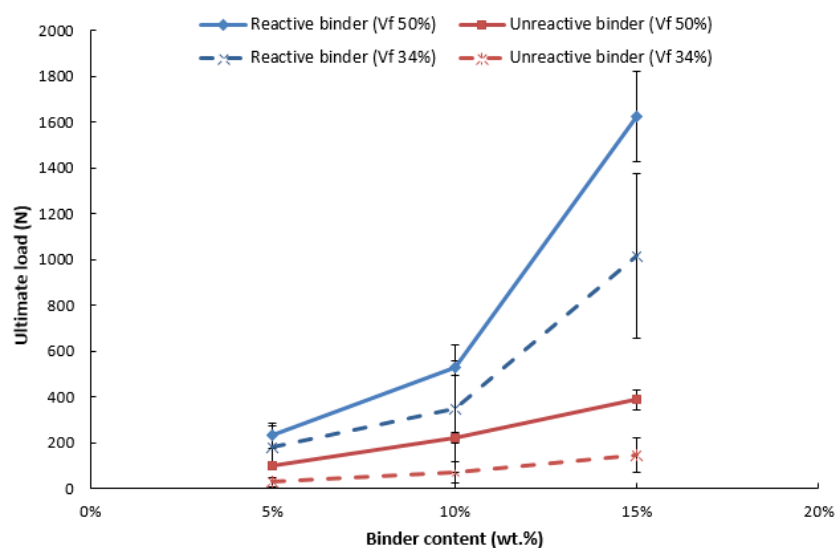


Figure 4.14 The ultimate load of dry DCFP preforms (used to create Vf 50% and Vf 34% moulded plaques) at different binder levels

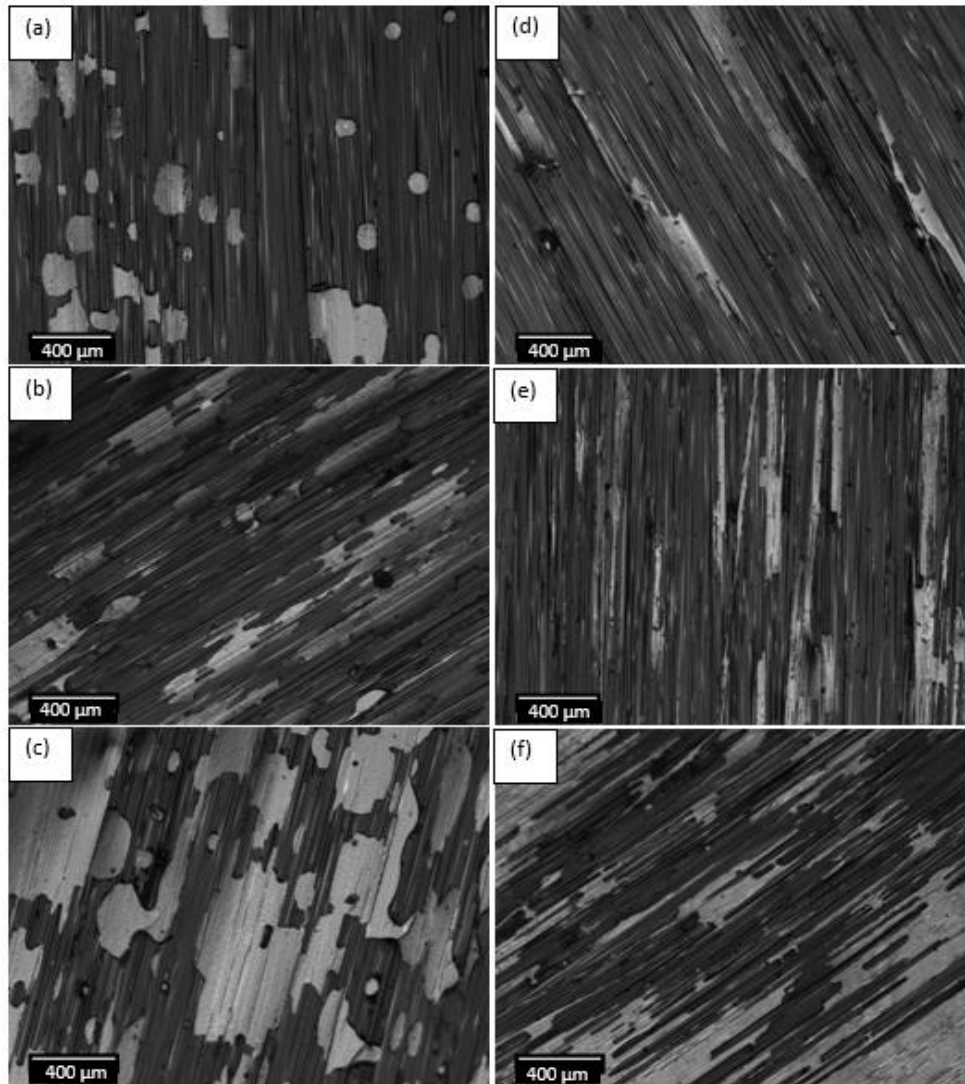


Figure 4.15 (a) – (c) Unreactive binder (locating on fibre tow surface) at 3 binder levels (5 wt.%, 10 wt.%, 15 wt.%) (d) – (f) Reactive binder (penetrating within the tow) at 3 binder levels (5 wt.%, 10 wt.%, 15 wt.%)

The resin temperature during HP-RTM was 80 °C, which is similar to the melting temperature of the Unreactive binder. The fibre architecture of plaques made with the Unreactive system was therefore influenced by the resin flow, regardless of the binder level. This can be seen clearly from the photographs in Figure 4.16 which compare the surfaces of plaques moulded with 10% Reactive and Unreactive binder.

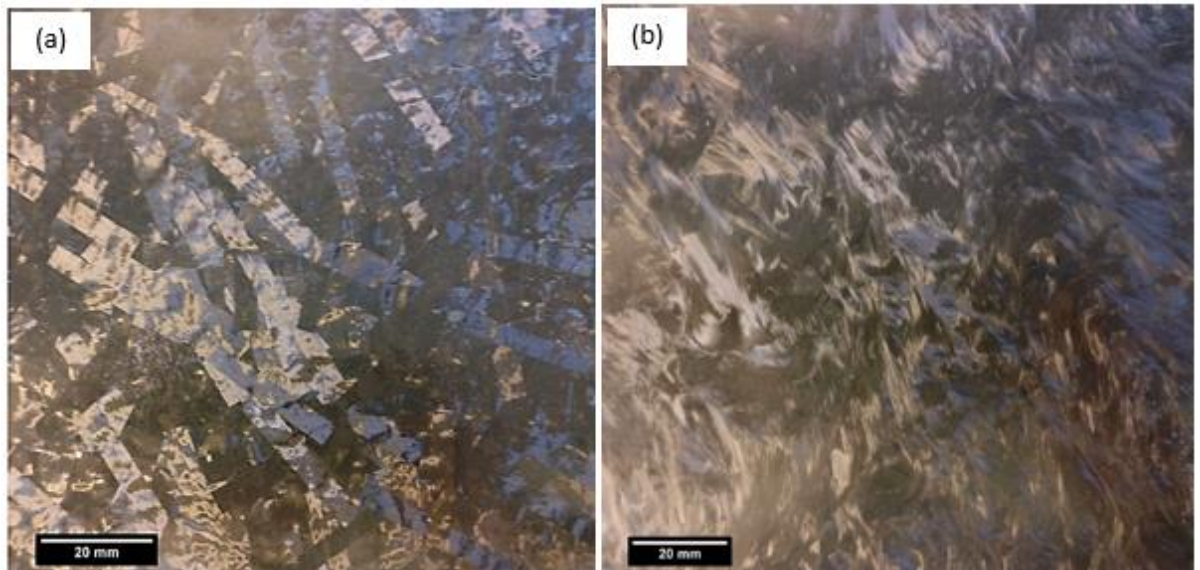


Figure 4.16 Fibre patterns on the surfaces of the HP-RTM moulded DCFPs with (a) 10wt.% Reactive binder (without fibre washing) and (b) 10wt.% Unreactive binder (with fibre washing)

4.5 Effect of binder on properties of moulded DCFP

Table 4.7 summarises the tensile properties of the moulded HP-RTM DCFP plaques with 5 wt.% and 10 wt.% binder content. The influence of the binder content on both the stiffness and strength is negligible (within the experimental error). The average stiffness of plaques preformed with the Reactive binder is similar for each binder level and binder type ($\sim 37 \text{ GPa} \pm 1.1\%$). Similarly the tensile strength increases by just 1.15% as the Reactive binder content increase from 5 wt.% to 10 wt.% (302.6 MPa to 306.1 MPa). The tensile strength of plaques moulded with 10 wt.% Reactive binder was approximately 4% higher than the tensile strength of plaques moulded with 10 wt.% Unreactive binder. Whilst this is statistically insignificant (coefficient of variation is $\sim 8\%$ in each case), this discrepancy is likely to increase if the target volume fraction is reduced. There is sufficient compaction of the fibres at 50% Vf

when the tool closes, which prevents fibre movement regardless of the binder type. The local fibre compaction force reduces as the volume fraction reduces, which leads to a reduction in the dry preform strength (Figure 4.14 – dash line), so more fibre distortion is expected during injection if the Unreactive system is used (as demonstrated in Figure 4.16). This becomes particularly relevant for more complex 3D components where the local thickness of the preform may vary around male corners, causing preform thinning. These regions are likely to experience a lower level of preform compaction as the mould tool closes and are therefore prone to fibre movement during resin injection, particularly if the Unreactive binder is used or there is insufficient binder.

Table 4.7 Tensile properties of HP-RTM moulded DCFPs with different binder types and content

Binder type and content	Reactive – 5wt.%	Reactive – 10wt.%	Unreactive – 10wt.%
Tensile strength (MPa)	302.6±19.3	306.1±24.5	294.0±22.1
Tensile modulus (GPa)	36.8±4.2	37.4±4.3	36.7±3.9

4.6 Effect of moulding process

Three moulding processes (RTM, HP-RTM, and compression moulding) were selected to investigate the effect of processing route on the mechanical properties of the moulded DCFP components. The resin systems used in the three moulding processes and their mechanical properties are listed in Table 4.8.

Table 4.8 Resin systems of three moulding processes used in this work and their tensile properties

	RTM	HP-RTM	Compression moulding
Resin system	Prime 20LV, Slow hardener (100:26 by wt)	EPIKOTE 05475 resin, EPIKURE 05443 curing agent, PAT 657/BW mould release additive (100:24:1.5 by wt)	Resin XU3508, Aradur 1571, Accelerator 1573, Hardener XB3403 (100:20:3:12 by wt)
Manufacturer	Gurit	Momentive	Huntsman
UTS (MPa)	73	85	78.6
Elastic Modulus (GPa)	3.5	2.9	3.2
Strain to failure (%)	3.5	6.0	4.5

4.6.1 Plaque manufacture

Each DCFP preform was trimmed to 300 mm × 300 mm for RTM moulding. Prime 20LV epoxy resin, supplied by Gurit, was injected into the mould at 8 bar and then cured at 70°C for 2 hours. The moulded plaques were post cured freestanding at 65°C for 8 hours in a hot air oven. HP-RTM was conducted by Voith GmbH to manufacture 700 mm × 600 mm DCFP components. A three component epoxy system was used consisting of Momentive EPIKOTE 05475 resin, EPIKURE 05443 curing agent and PAT 657/BW internal mould release additive (100:24:1.5 by wt). The EPIKOTE resin was preheated to 80 °C and injected with the curing agent and additive into a HP-RTM mould heated to 115°C. An injection pressure of 150 bar was used and the part was injected in approximately 30 seconds at a constant injection flow rate of 30 g/s. The cure time was 7 minutes.

For the compression moulding process, a liquid resin was sprayed during the fibre deposition stage (without powder binder) to create a net-shaped charge, following the methodology outlined by Evans et al. [62]. A four component system supplied by

Huntsman was used, consisting of Resin XU3508, Aradur 1571, Accelerator 1573 and Hardener XB3403 (100:20:3:12 by wt). The resin was preheated to 65 °C to reduce the viscosity below 0.5 Pa s during the deposition stage. The charge was left to chemically B-stage for 24 hours, before isothermal compression moulding at 130 °C for 30 min and under compression pressure of 85bar, followed by a 3.5 h freestanding post cure in an oven. Mechanical properties of the three resin systems are presented in Table 4.8.

4.6.2 Results

Figure 4.17 compares the tensile properties of DCFP plaques moulded by three different processes: RTM, HP-RTM, and compression moulding. The influence of the moulding process on the mechanical properties is highly dependent on the fibre type used. There is no appreciable difference in tensile strength (~300 MPa) or tensile modulus (~36 GPa) for plaques moulded by the three different processes when using T700 carbon fibre. Whereas the tensile stiffness and strength for plaques manufactured using K13916 fibre increase by over 100% (81 MPa to 174 MPa and 54 GPa to 125 GPa respectively) when using compression moulding rather than RTM.

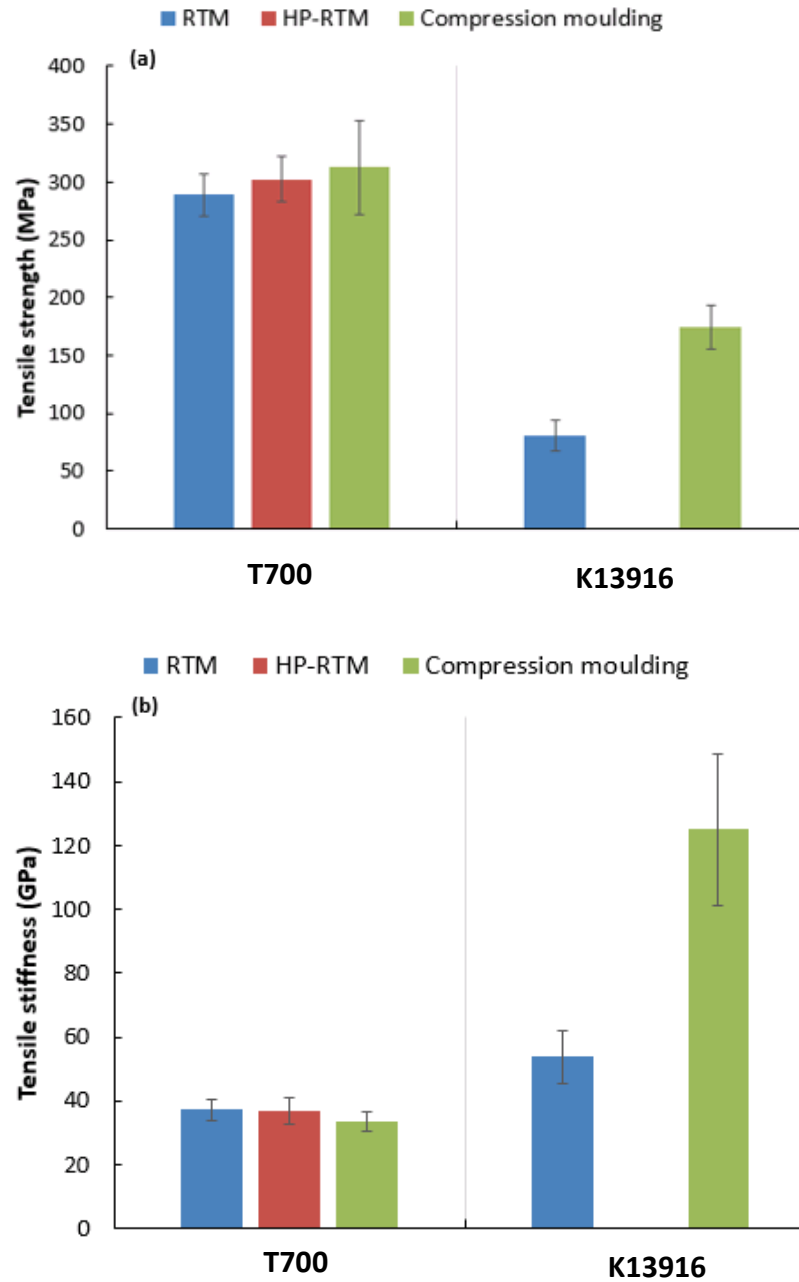


Figure 4.17 The effect of moulding route on (a) tensile strength and (b) tensile modulus for T700 and K13916

Micrographs in Figure 4.18 indicate that the fibre homogeneity is generally poorer for K13916 than T700 when sprayed by the DCFP chopper gun to create preforms for RTM (comparing (a) and (b)), due to the high linear density of the 16K tow (2200 g/km). Whilst the fibre distribution is similar during the charge deposition stage for the compression moulded components, in-mould flow occurs when pressure is

applied during the moulding stage to redistribute the fibres and minimise resin rich regions. This is supported by the volume fraction measurements presented in Table 4.9, which indicate that the coefficient of variation reduced from 13.2% to 8.5% for the RTM moulded plaques using K13916. The tows can also fragment due to shear, reducing the effective tow size and the level of filament end synchronisation, which has been demonstrated to have a positive effect on the tensile strength [87]. The microscopy images in Figure 4.18 (a) indicate large resin rich regions (the largest area is 8.7 mm²) for the RTM plaque manufactured with K13916. Whereas the largest area of these resin rich regions is reduced to just 0.8 mm² when moulded by compression moulding, as shown in Figure 4.18 (d). Compression moulding also reduces the size of the resin rich regions for T700 from 0.7 mm² to 0.2 mm², which results in an increase in tensile strength of 24 MPa.

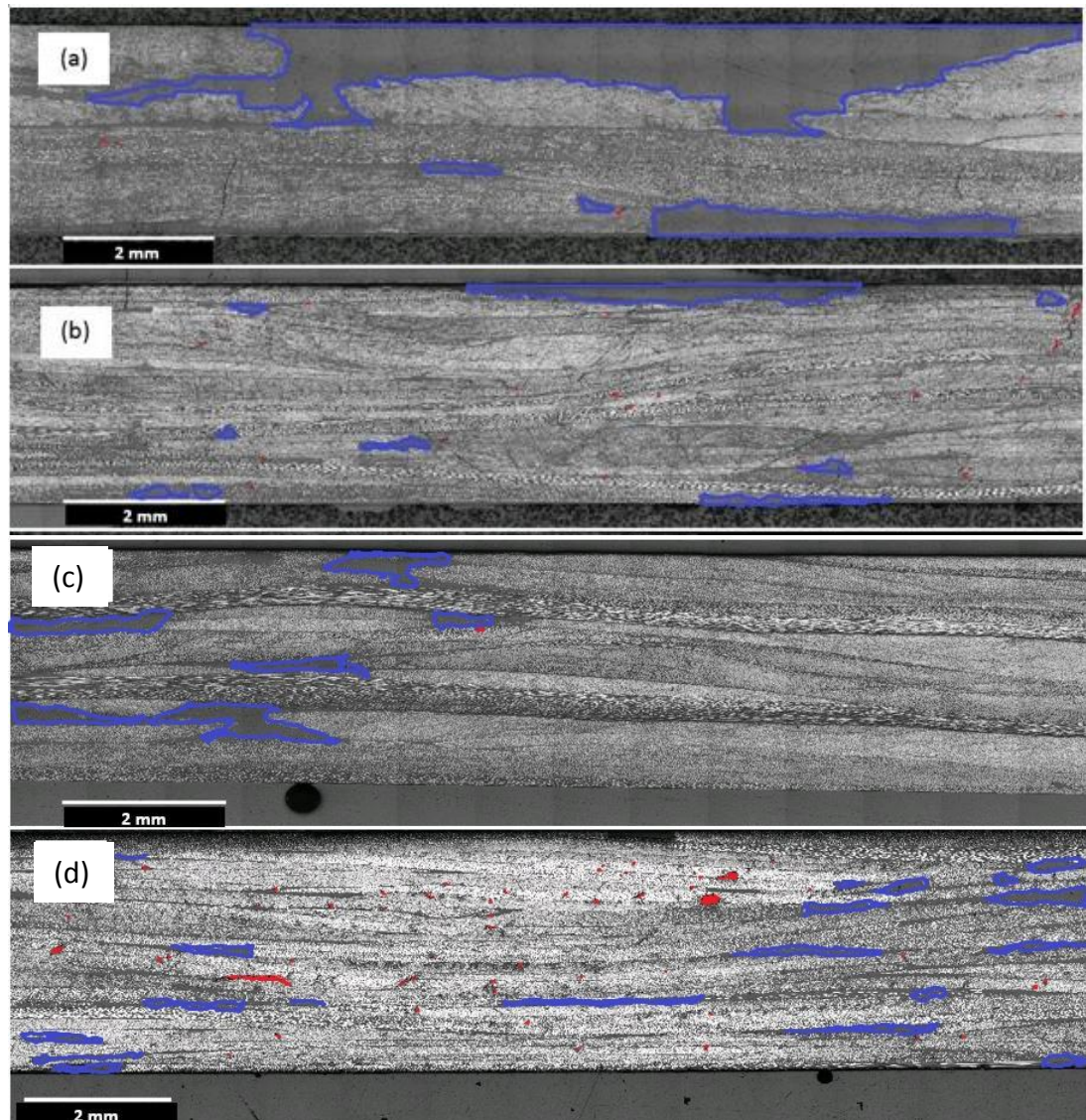


Figure 4.18 Microscopy images ($\times 5$ magnification) showing fibre distribution for RTM moulded DCFP plaques manufactured from (a) K13916 (b) T700; (c) – (d) K13916 and T700 DCFP plaques moulded by compression moulding. Blue lines and red dots indicate the resin rich regions and voids

Table 4.9 V_f COV of moulded DCFP plaques (V_f 50%) using different fibres

	T700	K13916
RTM	3.4%	13.2%
Compression moulding	3.2%	8.5%

The tensile stiffness of compression moulded plaques made from K13916 (125 GPa) is much closer to the theoretical stiffness (135 GPa) from the analytical model. Compression moulding improves the fibre distribution compared to both RTM

processes, as there is in-mould flow of the fibre network. This improves the connectivity between the fibre bundles, which enables better stress transfer.

Table 4.10 compares the three moulding routes in terms of cycle time and void content for DCFP plaques manufactured from Fibre 1. Compared to conventional RTM, HP-RTM and compression moulding offer ~60% faster moulding cycles, due to the reactivity of the resins used. Due to a higher resin injection pressure, an average void content of 0.63% was achieved using HP-RTM, which was approximately 25% lower than standard RTM (0.83%). The compression moulded parts have the highest void content (0.99%) among all the specimens observed. However, lower void content may be possible if a higher moulding pressure is used, as the void content in random carbon fibre SMCs was shown to reduce by 30% when the compression pressure was increased from 20 bar to 85 bar [62]. The applied pressure for the current study was limited to 85 bar due to the hardware available.

Table 4.10 Comparison of process, cycle time, and void level for DCFP plaques manufactured by three different moulding routes (T700, 45mm, Reactive binder 5wt.%, V_f 50%)

RTM			HP-RTM			Compression moulding		
Process	Time (s)	Void content	Process	Time (s)	Void content	Process	Time (s)	Void content
DCFP spray and unload	360	0.83%±0.13%	DCFP spray and unload	360	0.63%±0.05%	DCFP spray and unload	360	0.99%±0.14%
Prepare mould tool	600		Prepare mould tool	600		B-stage* & Prepare mould tool	600	
Load preform	60		Load preform	60		Load preform	60	
RTM inject	120		High pressure Circulation & Resin Injection	70		Mould closing & Consolidation	15	
RTM in-mould cure	1800		In-mould curing	120		Curing	180	
Total time	2940		Total time	1210		Total time	1275	

*The B-stage can be shortened to ~300s at 90 °C [59]

4.7 Conclusions

In this chapter, the fibre deposition path was characterised for the DCFP preforming development. The actual fibre preforming path in the X direction (robot direction same as chopper's tangential direction) was influenced by the robot and chopper gun, whilst no bias was observed in the Y direction (robot direction perpendicular to chopper's tangential direction). Reducing the TCP height can reduce the path bias and improve preforming resolution by reducing the width of the preforming path. When the TCP height was decreased from 200 mm to 50 mm, the path bias in the X direction reduced from 130 mm to 70 mm, and the path width reduced from 240 mm

to 130 mm. Based on the fibre deposition characterisation results, a robot programme for 2D DCFP preforming was developed, which can achieve low areal mass variability ($< 5\%$) and better preforming resolution. The fibre deposition method was shown to produce quasi-isotropic fibre distributions with no significant difference in mechanical performance in the two orthogonal directions. Hence, this method is suitable for producing planar structures, such as car bonnets or roofs, where some simple, gentle curvature could be added by post forming.

Using similar fibre deposition optimisation methods, the robot programme for a 3D (T-shirt) component was developed to overcome the influences of gravity, near-vertical surfaces and male/female corners, to also offer a preform with a local mass variability of less than 5%. Because the diameter of the fibre spray cone is too large compared to the features on the T-shirt structure, the influence of some factors could not be completely eliminated for the 3D component, therefore it was difficult to avoid fibre overspray.

Compared to EP05390, the reactive Momentive EPS620 binder offers higher bonding strength for DCFP preforms, making it suitable for high pressure manufacturing processes such as HP-RTM. It impregnates the fibre tow to provide 3D bonding rather than staying on the surface of the fibre tows. The influence of increasing the EPS620 binder content from 5 wt.% to 10 wt.% had a negligible effect on the strength and stiffness of moulded DCFP components.

Compared to conventional RTM, HP-RTM and compression moulding reduce the manufacturing cycle time by approximately 60%. Whilst the void content of the compression moulded DCFP plaques was the highest (0.99%) of the three moulding

processes, the in-mould flow of the charge improves the fibre distribution, reducing the size of resin rich regions to achieve higher mechanical properties than the other two moulding methods. For K13916 carbon fibre, the tensile stiffness and strength was improved by over 100% when compression moulding was used over RTM for the same fibre architecture.

Chapter 5 Permeability modelling of DCFP preforms

In this chapter a permeability model has been developed for DCFP, using a 3D pre-processor to produce realistic fibre architectures with appropriate through-thickness fibre distributions [88]. Local permeability values are calculated for the preform depending on the local fibre orientation and volume fraction. An experimental study has been conducted to understand the influence of the powder binder materials on the permeability of UD-NCF. This information has been used to calculate the effective mesoscale permeability values of the discontinuous fibre bundles. The model has been used to establish the effect of binder on the macroscale DCFP permeability, as higher binder content is generally required to stabilise preforms subjected to high injection pressures in HP-RTM (>100 bar).

5.1 Review of literature related to permeability of composite materials

Liquid moulding processes are typically used to manufacture DCFP components. DCFP preforms ideally require low flow resistance to reduce the moulding cycle time and to ensure there are no dry spots in the moulded part. In practice, resin race tracking, caused by fibre architecture variability, may occur during DCFP moulding, increasing the risk of dry regions. The local permeability of the preform is governed by both micro-scale permeability (intra-bundle flow) and macro-scale permeability (inter-bundle flow). Hence, there is a need to understand the local permeability variability of a DCFP preform to ensure the resin flow through the preform is repeatable and predictable.

5.1.1 Permeability measurements

The measurement of permeability is based on Darcy's law, expressed as follows [89]:

$$v = -\frac{K}{\eta} \Delta P \quad \text{Equation 10}$$

where v is average volume velocity, η is fluid viscosity, ΔP is the gradient of pressure, and K is permeability tensor. Permeability is a property of a porous material showing how easy a fluid can flow through the material under a pressure gradient. It is also described as 'fluid conductivity' by Collins [90]. In a three dimensional space, tensor K is written as:

$$[K] = \begin{pmatrix} K_{xx} & K_{xy} & K_{xz} \\ K_{yx} & K_{yy} & K_{yz} \\ K_{zx} & K_{zy} & K_{zz} \end{pmatrix} \quad \text{Equation 11}$$

For a thin preform (i.e. less than 3 mm), only the in-plane permeability in x and y directions are of interest. Additionally, the permeability tensor is orthotropic, so K_{xy} equals to K_{yx} [91]. Therefore, the tensor K can be rewritten as:

$$[K] = \begin{pmatrix} K_{xx} & 0 \\ 0 & K_{yy} \end{pmatrix} \quad \text{Equation 12}$$

There are two main methods for measuring in-plane permeability: unidirectional and radial flow measurements [92], illustrated schematically in Figure 5.1. For radial flow measurement, fluid is injected into the centre of the mould containing a preform. The elliptical flow front shape is recorded as a function of time. In contrast, for unidirectional flow measurement, the preform is placed in a rectangular mould. Fluid is injected at one side of the mould to make sure the fluid goes through the preform only in one direction. Both of the measurements can be applied under constant pressure or constant flow rate. Wong [91] compared the features of these two

measurement methods, as summarised in Table 5.1. In terms of permeability calculation, for the unidirectional flow method, the pressure drop and flow rate are measured and the permeability can be calculated simply using Darcy's law, while the calculation is more complicated for the radial flow method. The elliptical flow front needs to be resolved into a circle and then two principal permeabilities can be calculated through a series of calculations [89, 91]. However, due to the local variability in the DCFP architecture, it is difficult to observe a clear elliptical flow front, which creates further difficulties in calculating the macroscale permeability. Hence, for permeability measurement of DCFP, the unidirectional flow measurement method is a good choice due to its simplicity and efficiency.

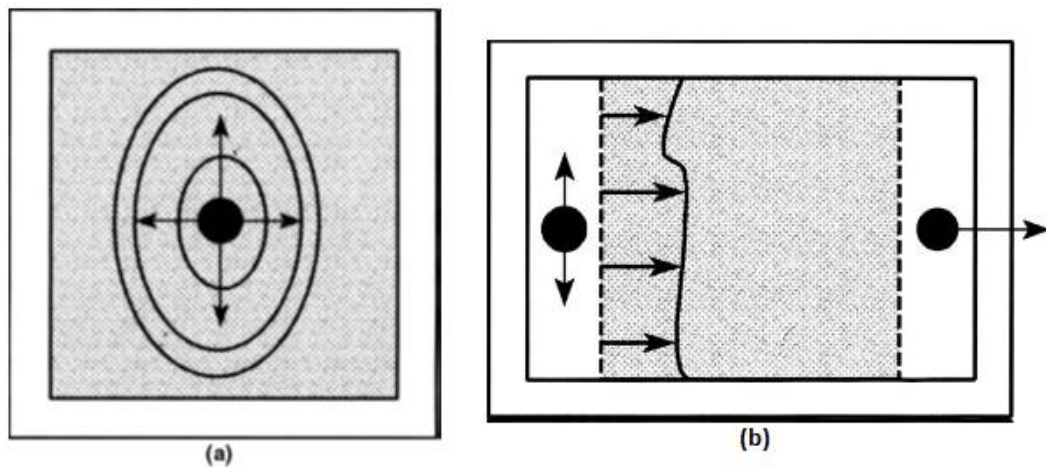


Figure 5.1 Schematics of geometries of radial (a) and unidirectional (b) flow measurement moulds [92]

Table 5.1 A comparison between unidirectional and radial flow in-plane permeability measurement methods [91]

Experimental Methods	Features
Rectilinear (Unidirectional) flow method	<ul style="list-style-type: none"> • Yields permeability along the flow direction only. Employed mainly to characterise isotropic materials. • Permits measurement of saturated and unsaturated permeabilities. • Easy implementation and calculation of permeability. • Prone to edge effects – a preferential flow observed along the mould wall due to a small gap existing between the wall and the preform (usually referred to as 'racetracking').
Radial flow method	<ul style="list-style-type: none"> • Simultaneous determination of both principal in-plane permeabilities and tensorial orientation. • Measurement of saturated and unsaturated permeabilities. • More complex data processing. • Complicated analytical solution of the permeability values. Error might be induced when determining the equivalent elliptical flow front from the data.

5.1.2 Factors influencing preform permeability

In addition to fluid speed, fluid viscosity, and pressure gradient, which are all terms in Darcy's law, many other variables influence the permeability of fibre reinforced composites as discussed below.

5.1.2.1 Fibre architecture parameters

Endruweit et al. [93] investigated the influence of fabric non-uniformity on the variations of in-plane permeability. Understandably, higher homogeneity of the fabric architecture resulted in lower variability of the local permeability. Although this study was conducted for continuous fibre fabrics [93], these observations are still relevant DCFP preforms. Endruweit et al. [94] conducted a series of permeability measurements for two fibre types with different lengths (10mm - 45mm) and tow sizes (3K - 24K): One fibre had high potential to filamentise (Fibre E), while another

one had low potential (Fibre J). For Fibre E, the global permeability increased with increasing fibre length (Figure 5.2 (a)), whilst there was no clear trend for the effect of fibre length for Fibre J (Figure 5.2 (b)). Fibre J provides a more heterogeneous structure due to little filamentisation (bundle fragmentation), which means resin can flow readily through the inter-bundle spaces. Whilst fibre E produces a more homogeneous architecture due to high filamentisation, the inter-bundle spacings get significantly larger as the fibre length increases, as there are fewer bundle segments per unit volume for longer lengths. The inter-bundle spacings are an order of magnitude higher for Fibre J, even for short fibre lengths, therefore the effect of fibre length for Fibre J is less significant in terms of the permeability. For fibres without filamentisation, the spacing between fibre bundles has a large influence on the permeability variability, as indicated by the error bars in Figure 5.2(b) compared to Figure 5.2(a).

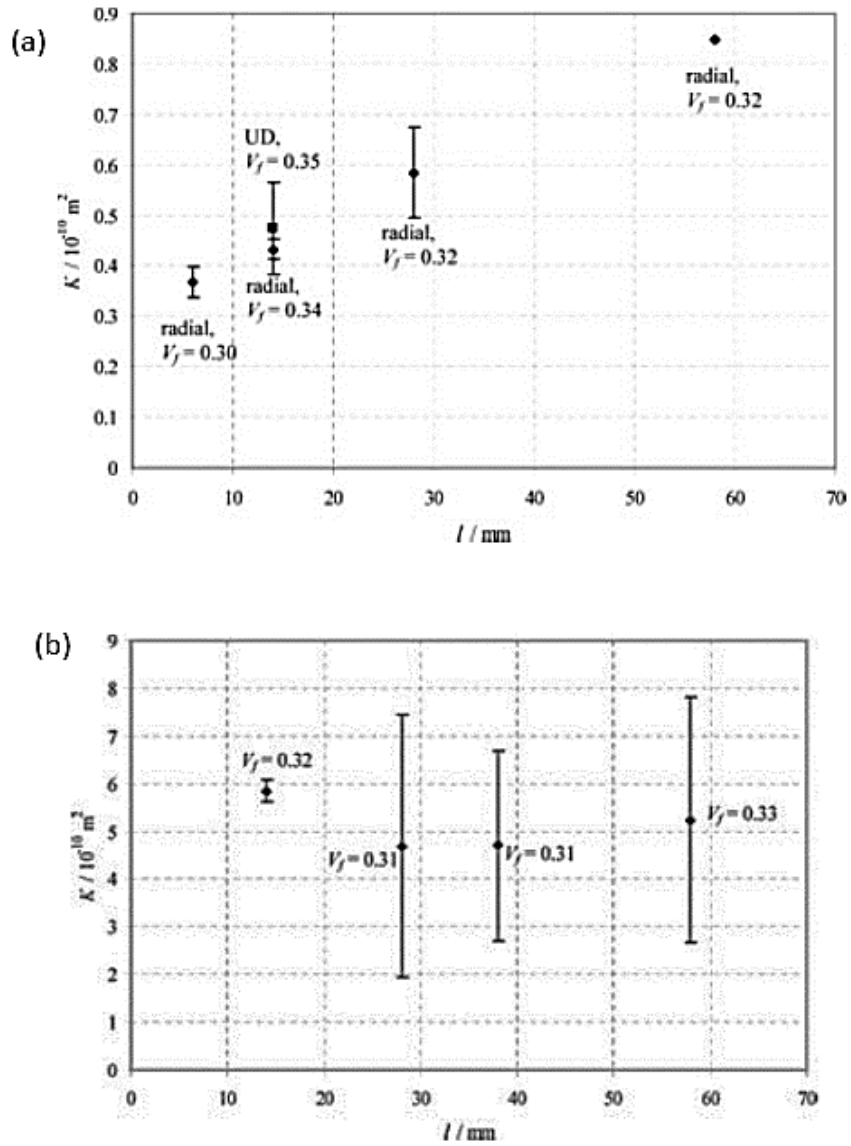


Figure 5.2 Isotropic permeability K versus fibre length for a 24K fibre with (a) high-level and (b) low-level filamentisation

5.1.2.2 Micro-scale factors

Not only can the macro-structure of carbon fibre composites influence the permeability, but also some parameters at the filament level can affect permeability too, such as fibre diameter, bundle size, and fibre volume fraction. The effect of these

parameters on permeability is described by the empirical Carman-Kozeny equation expressed as follows [95, 96]:

$$K = \frac{D_f^2}{16K_0} \left(\frac{\varepsilon^3}{(1-\varepsilon)^2} \right) \quad \text{Equation 13}$$

where D_f is fibre diameter, ε is porosity (which equals to one minus fibre volume fraction), and K_0 is the Kozeny constant. This equation is also applied to the in-plane permeability modelling for many liquid moulding process studies [97-99].

For the permeability studies at the micro-scale, capillary pressure is considered [97, 99]. Therefore, the pressure gradient in Equation 10 contains both applied mechanical pressure and capillary pressure. With this consideration, Foley and Gillespie [97] modelled fluid impregnation in a fibre bundle to understand the effect of fibre diameter. It was found that for a certain bundle size, the infiltration time increased by 100 times when fibre diameter decreased from 7 μm to 70 nm. However, according to Amico and Lekakou [100], the effect of capillary pressure will be negligible when the resin injection pressure exceeds 1 bar.

Endruweit et al. [98] investigated the permeability in fibre bundles with random filament arrangements. In this study, a compaction process for several 12K bundles was used to simulate an increase in fibre volume fraction. The permeability of a fibre bundle parallel to its axis dropped from $0.577 \times 10^{-12} \text{ m}^2$ to $0.180 \times 10^{-12} \text{ m}^2$ when the fibre volume fraction increased from 46% to 72%.

5.1.2.3 Effect of binder content

During mould filling, binders in the preform will obstruct resin flow. Rohatgi and Lee [101] found that permeability decreased by ~40% when binder content increased

from 0 wt.% to 8 wt.%. Furthermore, compared with binders that were distributed on the outside of fibre bundles, binders that permeate inside fibre bundles have no significant influence on permeability. This is because they remain within the fibre tows rather than blocking the critical flow channel between bundles [101]. A reduction in permeability was also reported by Shih et al. [81] as binder concentration was increased. However, Dickert et al. [102] considered the effect of binder concentration on permeability to be more complex. They carried out permeability measurements for 5 types of non-crimp fabric and found that the permeability of two fabrics increased when the binder content increased from 0 to 2%, as the binder particles acted as spacers between the fibre layers. Hence, flow channels were widened, leading to an increase in permeability. Furthermore, Brody and Gillespie [103] indicated that dissolution of binders can increase the viscosity of the resin, which complicates the permeability measurement according to Darcy's law.

5.1.3 Permeability modelling

5.1.3.1 Analytical permeability model

Analytical models for permeability prediction are formed by many closed-form equations, using physical parameters to describe the flow process.

Kozeny [95] proposed an early approach to describe flow through an isotropic porous medium. Carman [96] modified the Kozeny's approach by considering the specific pore surface area and eventually derived the Kozeny-Carman equation (Equation 13). This equation has been widely applied for fabric permeability prediction, but it is unsuitable for describing transverse flow through aligned fibres. On the basis of the

Kozeny-Carman equation, Gebart [104] proposed two equations which are able to properly describe the permeability along the flow axis (k_1) and the permeability perpendicular to the flow axis (k_2). The equations are as follows:

$$k_1 = \frac{R_f^2 (1-V_f)^3}{4c_1 V_f^2} \quad \text{Equation 14}$$

$$k_2 = c_2 \left(\sqrt{\frac{V_{fmax}}{V_f}} - 1 \right)^2 R_f^2 \quad \text{Equation 15}$$

where R_f is the radius of fibre, V_f is fibre volume fraction, and c_1 , c_2 , and V_{fmax} are geometry constants which are dependent on the fibre arrangement. The values of these geometrical constants are listed in Table 5.2. Quadratic fibre packing is typically assumed for DCFP preform permeability modelling [94, 105].

Table 5.2 The parameter values in Equation 14 and Equation 15.

Fibre arrangement	C_1	C_2	V_{fmax}
Quadratic packing	1.78	0.40	78.5%
Hexagonal packing	1.66	0.23	90.7%

The permeability of the spacings between the fibre layers and fibre bundles should also be considered. Ni et al. [106] derived a so called ‘equivalent permeability’ to represent the permeability between plates:

$$K = \frac{H^2}{12} \quad \text{Equation 16}$$

where H is the cavity height.

Furthermore, the unidirectional flow permeability can be calculated by using the equation as follows [99]:

$$K = -\frac{x^2 \varepsilon \eta}{2 \Delta P t} \quad \text{Equation 17}$$

where t is penetration time and x is the penetration distance.

5.1.3.2 Numerical permeability models

Flow through a 3D unit cell of a plain weave structure was simulated by Ngo and Tamma [107] using a finite element method. Although the results provided a good correlation with previously published permeability measurement data, the authors relied upon published geometric data to conduct the simulation. Fibre volume fraction and the fibre arrangement were assumed rather than measured for the local permeability calculation. Deleglise et al. [108] provided a model for high speed RTM injection with highly reactive resins, using Darcy's law. Hence, the viscosity change of the resin during the injection process was considered.

Endruweit et al. [105] proposed a stochastic model to describe the distribution of random fibre bundles in DCFP architectures, introducing a local orientation for each fibre bundle, α_i . The in-plane permeability of a fibre bundle was expressed as follows:

$$K_i(\Delta\alpha_i) = \begin{pmatrix} k_1 \cos^2 \Delta\alpha_i + k_2 \sin^2 \Delta\alpha_i & (k_2 - k_1) \sin \Delta\alpha_i \cos \Delta\alpha_i \\ (k_2 - k_1) \sin \Delta\alpha_i \cos \Delta\alpha_i & k_1 \sin^2 \Delta\alpha_i + k_2 \cos^2 \Delta\alpha_i \end{pmatrix} \quad \text{Equation 18}$$

where $\Delta\alpha_i$ equals to $(\alpha_i - \alpha_0)$ and α_0 is the principal material axis of the stack of N bundles. However, this model overlooks the spacing between fibre bundles. This model was further developed [94], to include the spacings, assuming several different fibre distributions (Homogenisation, cluster, and even, shown in Figure 5.3) according to observations made from micrographs. The expression used to determine the permeability of a representative cell is shown in Equation 19, where T_f is the thickness of fibre bundle, T_m is the inner mould cavity thickness, and h is the spacing between fibre bundles. Results indicate that evenly distributed spacings

between fibre bundles (through thickness) produces the most accurate permeability predictions. However, these values are 25% higher than the experimental data. In practice the fibre bundles cannot be evenly distributed through the thickness direction, therefore the simulation results in [105] represent an over-estimation of the DCFP permeability. Additionally, the fibre architecture was generated by a 2D beam model, shown in Figure 5.4. Each beam element represented a fibre bundle with an assumed width, which introduced some errors in terms of the fibre distribution. Hence, this method indicates that the methodology is appropriate for predicting the mesoscale permeability, but a more accurate pre-processing tool is required to generate more realistic fibre architectures to improve predictions.

$$K = \sum_{i=1}^N \frac{T_f}{T_m} K_i(\Delta\alpha_i) + \sum_{j=1}^M \frac{h_j}{T_m} \frac{h_j^2}{12} \quad \text{Equation 19}$$

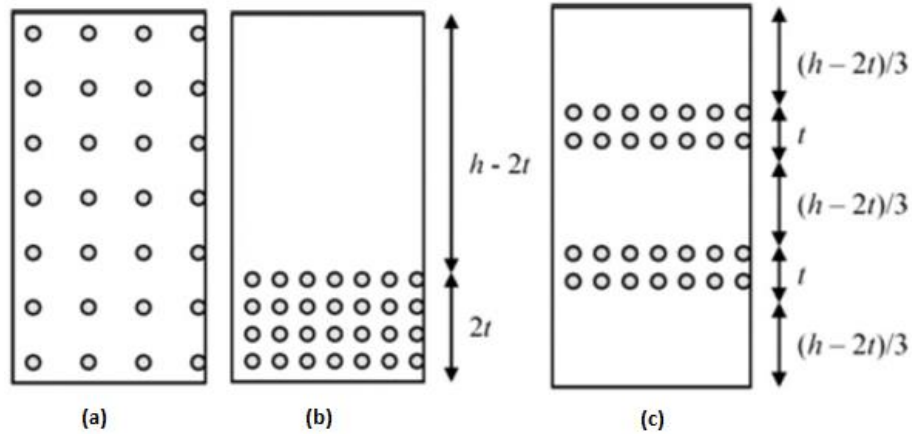


Figure 5.3 Fibre distribution types: (a) homogenisation, (b) cluster, and (c) even

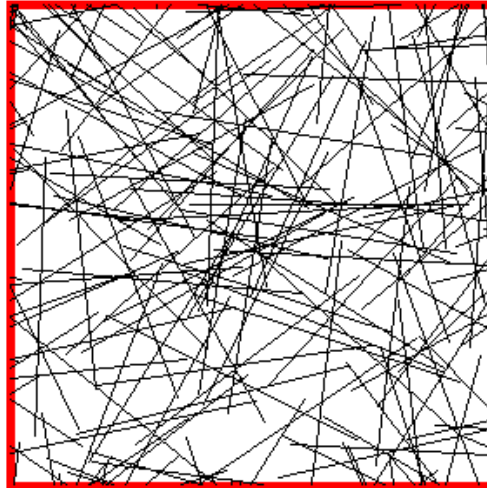


Figure 5.4 The beam-element DCFP architecture model used in [105]

5.1.4 Conclusion

DCFP preform variability makes permeability measurement time consuming, so an accurate predictive model would be beneficial to understand the effect of key microstructural parameters. Previous attempts at predicting the permeability of DCFP were limited by simple assumptions for the fibre distribution through the thickness. A more realistic pre-processor is required to produce accurate fibre architectures, in order to predict the permeability of DCFP with confidence. HP-RTM is a rapid moulding technology that can work with DCFP to further improve production rate. Higher binder content is needed to prevent fibre washing under high resin injection pressure. Hence, it is also essential to understand the effect of the binder content on the preform permeability and build this into the simulation.

5.2 Experimental permeability measurement to investigate the effect of binder

5.2.1 Methodology

Permeabilities of DCFP and UD-NCF preforms with different binder types and content were measured in a unidirectional flow measurement mould (Figure 5.5). The cavity height of the mould was 2mm when the mould was assembled. The details of all the preforms measured are listed in Table 5.3. The permeability test coupons have the same dimensions as the dry preform tensile test coupons: 280mm × 115mm. The test coupon was 0.25 mm wider than the inner cavity wall on each side, to prevent race-tacking. After a preform was placed in the mould, 5w-20 engine oil (with a viscosity of 0.118Pa·s) was injected into the mould under a pressure of 1.5 bar. When oil reached the position of the pressure sensor (indicated in Figure 5.5), which was 250mm from the inlet, the time was recorded. The viscosity of the oil, the distance between the sensor and the inlet, and the time for the oil to reach the sensor were used to calculate the permeability, using the equation below.

$$K = \frac{x^2 \eta \phi}{2 \Delta P t} \quad \text{Equation 20}$$

$$\phi = 1 - V_f \quad \text{Equation 21}$$

where x is the distance between the sensor and the inlet port, η is the viscosity of the engine oil, ΔP is the pressure used to inject oil, t is the time when oil flow reaches to the sensor, and V_f is the carbon volume fraction in the mould. Thirty measurements were conducted for DCFP preforms with 45mm-long fibre and 10wt.% of EPS620 binder (DCFP-45mm-EPS620-10wt.%). Fifteen repeats were performed for all other preform types.

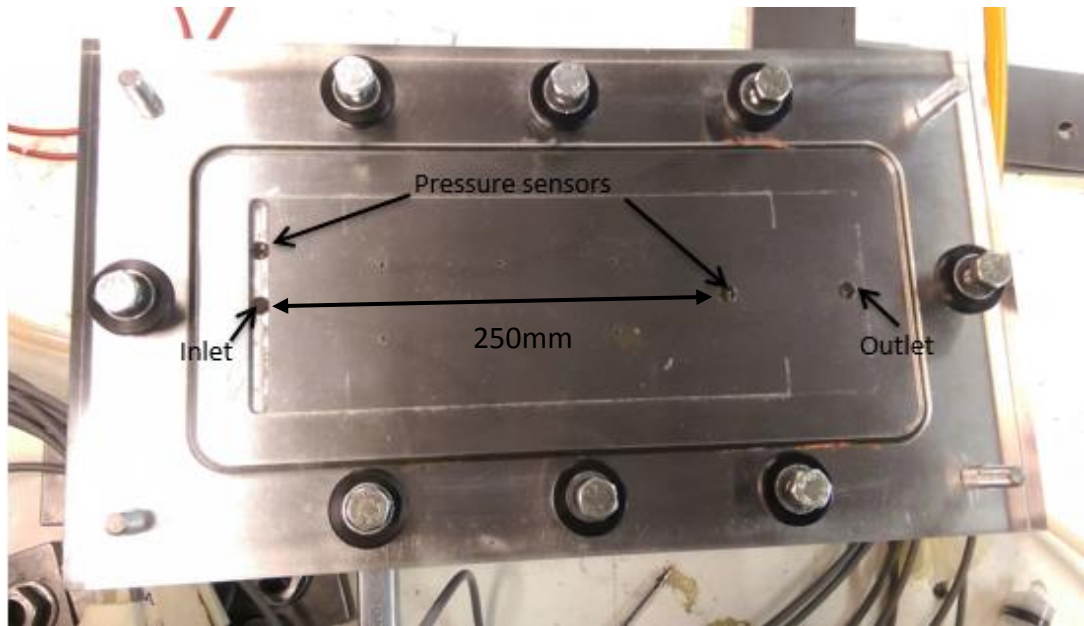


Figure 5.5 Unidirectional flow permeability measurement rig

Table 5.3 Details of preforms in permeability measurement

Sample type	Fibre length	Carbon V_f in the permeability measurement mould	Binder type	Manufacturer	Binder content	Measurement repeat
DCFP	45mm	31%	EPS620	Momentive	5wt.%	15
					10wt.%	30
	45mm	46%	EPS620	Momentive	5wt.%	15
					10wt.%	15
	45mm	31%	Neoxil 940	Aliancys (Formerly DSM)	5wt.%	15
					10wt.%	15
UD-NCF	-	46%	EPS620	Momentive	0wt.%	15
					5wt.%	15
					10wt.%	15

5.2.2 Measurement uncertainty

In-plane permeability measurements of thirty DCFP samples (T700 12K, V_f 31%, EPS620 10wt.%), taken from three DCFP preforms, were conducted to quantify the level of variability and to understand the size of the population required to achieve a representative mean value [94]. The cumulative average permeability value is

plotted as a function of the number of measurements in Figure 5.6. For the low fibre volume fraction ($V_f=31\%$), approximately 10 measurements are required before the average permeability value reaches a stable plateau. The average permeability value after 10 iterations is within 97.6%, which offers an error of approximate 3%, of the average value after 30 iterations. A typical irregular flow front for a DCFP preform with a fibre volume fraction of 31% is shown in Figure 5.7, which was taken in-situ during a permeability measurement. This is caused by the inhomogeneous fibre distribution, since on average there were only 4.2 tows/cm² for this particular fibre architecture, which resulted in large resin rich regions.

The homogeneity improves for specimens with a 46% fibre volume fraction, increasing the factor to 6.3 tows/cm². Consequently, the representative average permeability value is achieved after just 6 iterations, as shown in Figure 5.6. For the following work in this thesis, at least 10 measurements or simulations are performed for each permeability measurement for all DCFP fibre architectures.

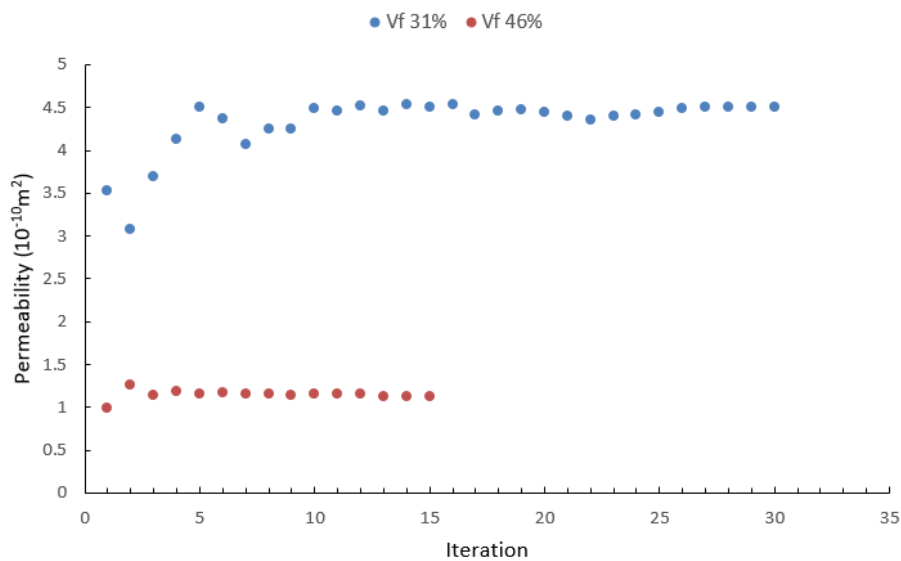


Figure 5.6 Cumulative average permeability value as a function of number of measurements for two different DCFP preform architectures (T700 12K, V_f 31% and 46%, EPS620 10wt.%).



Figure 5.7 Typical profile of flow front from a DCFP preform during an in-plane permeability test

5.2.3 The effect of binder on permeability

5.2.3.1 The effect of binder on permeability of unidirectional fibre fabric

Figure 5.8 shows the measured permeability values (k_1 and k_2) for a unidirectional (UD) non-crimp fabric (NCF) using three different EPS620 binder levels: 0 wt.%, 5 wt.%, and 10wt.%. The value of k_1 (fibre longitudinal direction) decreased by 60.1% (from $4.04 \times 10^{-10} \text{m}^2$ to $1.61 \times 10^{-10} \text{m}^2$) when 5 wt.% of binder was added to the preforms. However, the effect of binder became less significant when the binder level increased from 5 wt.% to 10 wt.% (from $1.61 \times 10^{-10} \text{m}^2$ to $1.55 \times 10^{-10} \text{m}^2$), as the permeability only decreased by a further 4%. Compared to k_1 , the permeability in the transverse fibre transverse direction, k_2 , is less sensitive to the increasing binder level, especially in the range of 0 wt.% - 5 wt.%, as shown by Figure 5.8. The permeability reduction ratios at different binder levels are listed in Table 5.4.

If it is assumed that fibre filaments in the UD-NCF preform are homogenously distributed in the quadratic form, then Equation 14 and Equation 15 and parameters in Table 5.2 can be used to predict k_1 and k_2 for the UD NCF. Consequently, k_1 and k_2 are calculated to be $2.37 \times 10^{-12} \text{m}^2$ and $0.25 \times 10^{-12} \text{m}^2$ respectively. There is a significant difference between k_1 and k_2 for the analytical values as in the experimental values ($k_1 4.04 \times 10^{-10} \text{m}^2$; $k_2 1.19 \times 10^{-10} \text{m}^2$) when the preforms have 0 wt.% binder, albeit k_1 is approximately 4 times higher than k_2 in both the experimental and analytical values. This can be attributed to the architecture of the NCF, which contains intra-ply stitches, which create spaces between the fibre tows in the transverse direction and local out-of-plane resin channels around each stitch. Figure 5.9 illustrates the flow fronts for the UD-NCF preforms with different binder levels taken from the permeability measurement. From Figure 5.9 (a) and (c), it can be seen that the flow progresses quickly through the spacing between the fibre tows (in the k_1 direction) and through the stitches when there is no binder in the preforms, generating a slight waviness in the fibre tows in the k_2 direction. Because of the large difference in flow velocity for fibre tows compared to the spacing/stitches, some dry spots were observed (Figure 5.9 (c)) after the flow front had passed. When the binder level was increases to 10wt.%, the tow spacing still provided a flow channel (Figure 5.9 (b)) in the k_1 direction, but the propagation of the flow front in the transverse k_2 direction (Figure 5.9 (d)) was obstructed by the binder, so the profile of the flow front appeared to be linear.

Based on the results, binders influence the principal permeabilities, k_1 and k_2 , in different ways. Hence, the decreasing ratios of the permeability in the principal directions of the NCF (Table 5.4) can be used to account for the effects of binder in

the DCFP permeability model, by using Equation 14 and 15 as the binder content increases.

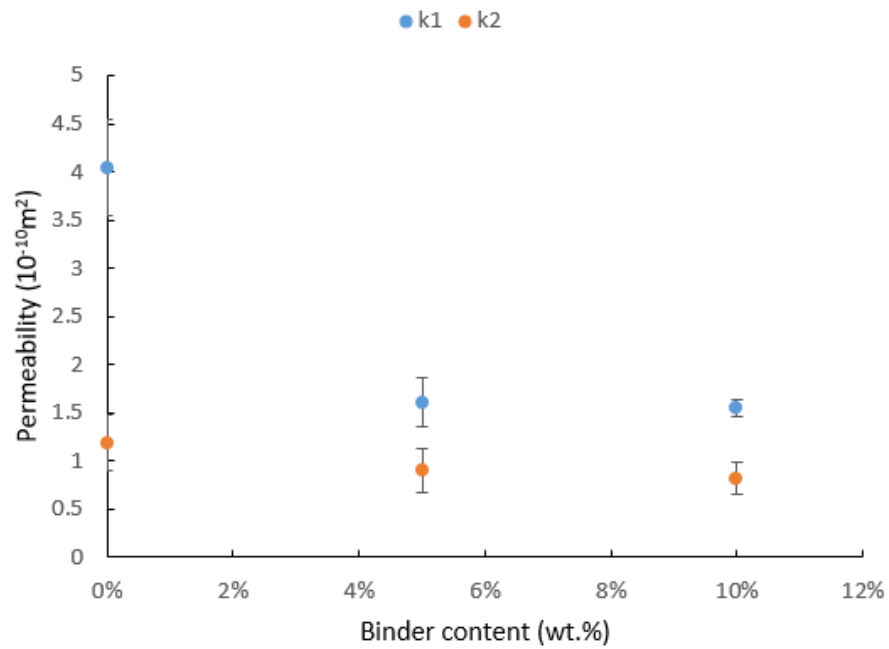


Figure 5.8 k₁ and k₂ values of the UD-NCF preforms (V_f 46% in the permeability rig) at three EPS620 binder levels: 0wt.%, 5wt.% and 10wt.%

Table 5.4 Permeability decrease ratio at k₁ and k₂ directions at different binder levels

Decrease ratio	Binder content		
	0 wt.%	5 wt.%	10 wt.%
k ₁	-	-60.1%	-3.7%
k ₂	-	-24.7%	-9.1%

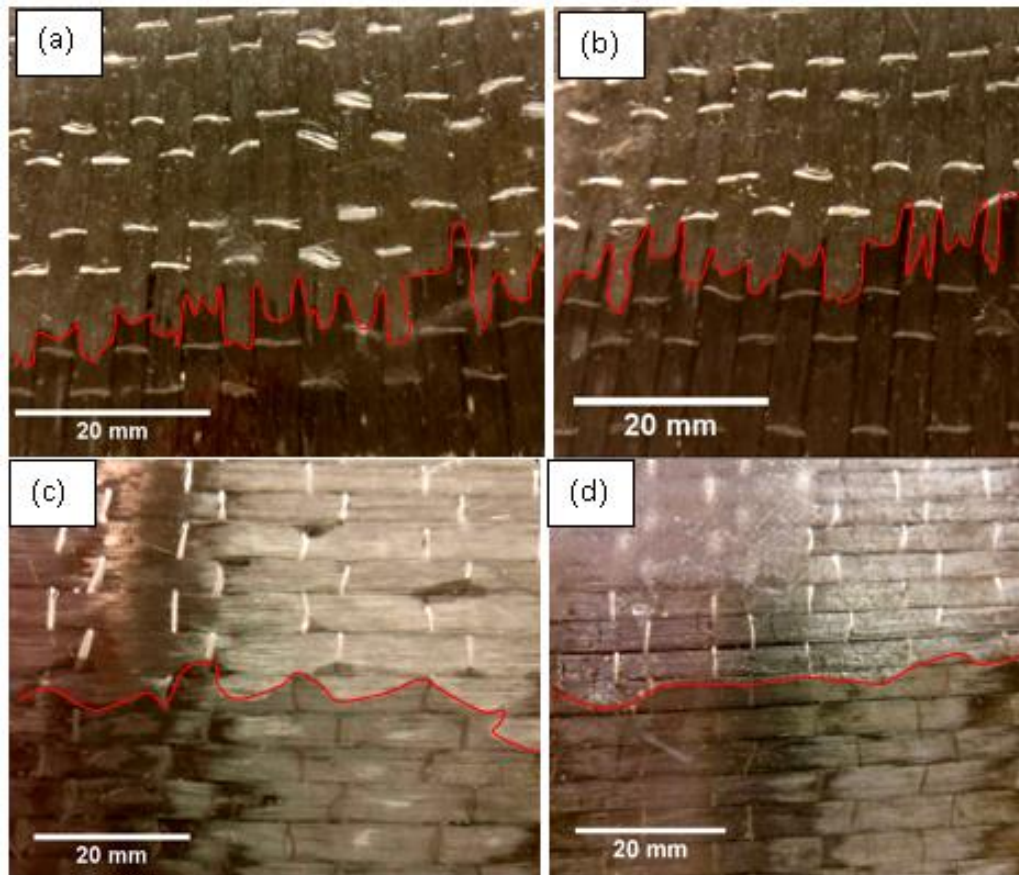


Figure 5.9 The profiles of flow fronts on the UD-NCF preforms with different binder levels at k1 and k2 directions: (a) 0wt.% k1; (b) 10wt.% k1; (c) 0wt.% k2; (d) 10wt.% k2.

5.2.3.2 The effect of binder on permeability of DCFP

From the last sub-section, the effects of binder content on the permeability at fibre longitudinal and transverse directions are different. This section will address the effect of binder on the permeability of random discontinuous fibre architecture. The permeability results of DCFP preforms with different binder types and levels are listed in Table 5.5. In general, the permeability reduces as the binder content increases, since the binder material hinders fluid flow at the bundle-bundle contact points. In addition, at low binder levels (5wt.%), the permeability of the DCFP preforms with Neoxil940 binder is approximately double that of the preforms using

EPS620 binder ($11.49 \times 10^{-10} \text{m}^2$ VS $6.32 \times 10^{-10} \text{m}^2$ respectively). This large difference can be attributed to the difference in binder distribution caused by the different particle sizes (EPS620 $\sim 100 \mu\text{m}$; Neoxil940 $\sim 900 \mu\text{m}$). The distribution of the coarser Neoxil940 binder is less homogenous, particularly when the binder level is low. This is also supported by the larger standard deviation value reported for the permeability of specimens produced with the Neoxil system. As the binder content increases to 10wt.%, the difference in permeabilities between the EPS620 and Neoxil940 bindered preforms becomes smaller (permeabilities of both are around $5 \times 10^{-10} \text{m}^2$), as the distribution of the coarse binder improves.

As the volume fraction of carbon fibre increases, the effect of binder concentration on the in-plane permeability becomes less significant. The permeability reduces by approximately 16% as the binder content is increased from 5wt.% to 10wt.% at a V_f of 46%, compared to a reduction of 27% at a V_f of 31%. Both the inter and intra bundle spacings reduce as the fibre volume fraction increases, which dominates the preform permeability more than the binder content. It is conceivable that less binder is required for preforms with higher fibre volume fractions, as the through-thickness pressure induced by the tool is sufficient to hold the preform in position. However, the success of this approach depends on the homogeneity of the fibres and the complexity of the preform, as the pressure is non-isostatic and will be lower on near-vertical faces.

Table 5.5 Permeability measurement results of DCFPs with different binder types and levels

	Permeability unit	EPS620 5wt.%	EPS620 10wt.%	Reduction
Carbon fibre Vf 31%	10^{-10}m^2	6.32 ± 1.90	4.59 ± 1.10	27.4%
Carbon fibre Vf 46%	10^{-10}m^2	1.34 ± 0.45	1.13 ± 0.33	15.7%
		Neoxil940 5wt.%	Neoxil940 10wt.%	
Carbon fibre Vf 31%	10^{-10}m^2	11.49 ± 4.02	5.07 ± 2.14	55.8%

5.3 DCFP permeability model creation

5.3.1 Model architecture

Four programmes were used for modelling the permeability of DCFP preforms: 1) A force-directed algorithm was used to deposit discontinuous fibre bundles to create a ‘digital-twin’ of the representative DCFP architecture, 2) The fibre geometry was analysed using a Matlab script to determine the local fibre volume fraction, local fibre orientations and through-thickness spacings, 3) Local permeability values were calculated to account for the heterogeneous fibre distribution, 4) PAM-RTM was used to simulate resin flow through the preform in order to calculate the global permeability values based on the fill time. The relationship between these four programmes is presented in Figure 5.10.

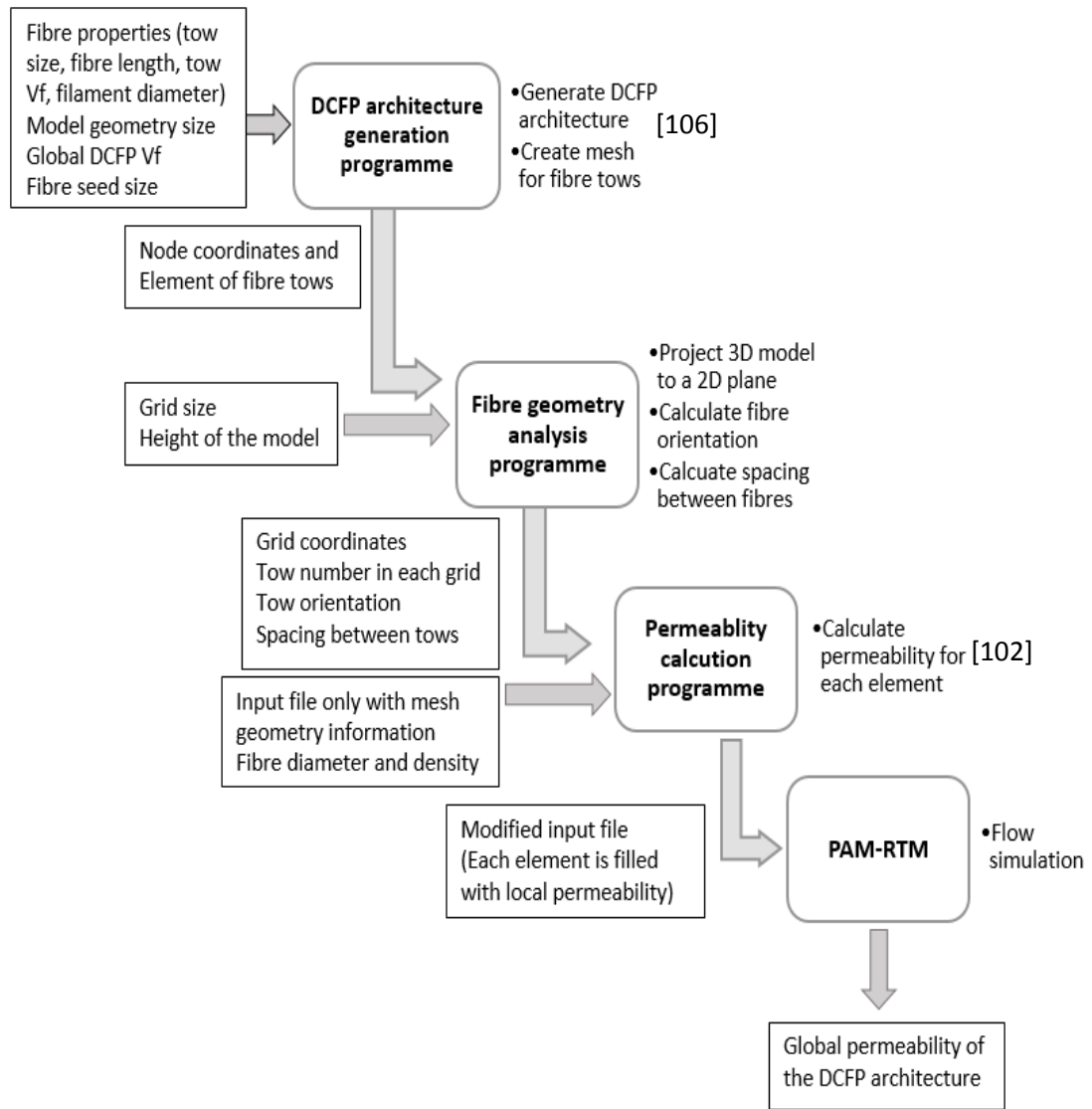


Figure 5.10 The programmes used for permeability modelling in present work and input/output information at each stage

5.3.2 Random fibre generator

A 3D DCFP preform model was generated by the fibre architecture generation programme, developed in [88], through the procedures shown in Figure 5.11. The fibre properties (tow size, fibre length, tow volume fraction) and model size (dimensions and global carbon fibre volume fraction) were defined at the beginning. The values of the node charges and the spring properties were applied to the model

according to [109]. The nodal charges determine the fibre distribution in the through-thickness direction by applying reaction forces between neighbouring fibre bundles. Detailed explanations of the mechanism can be found in [109].

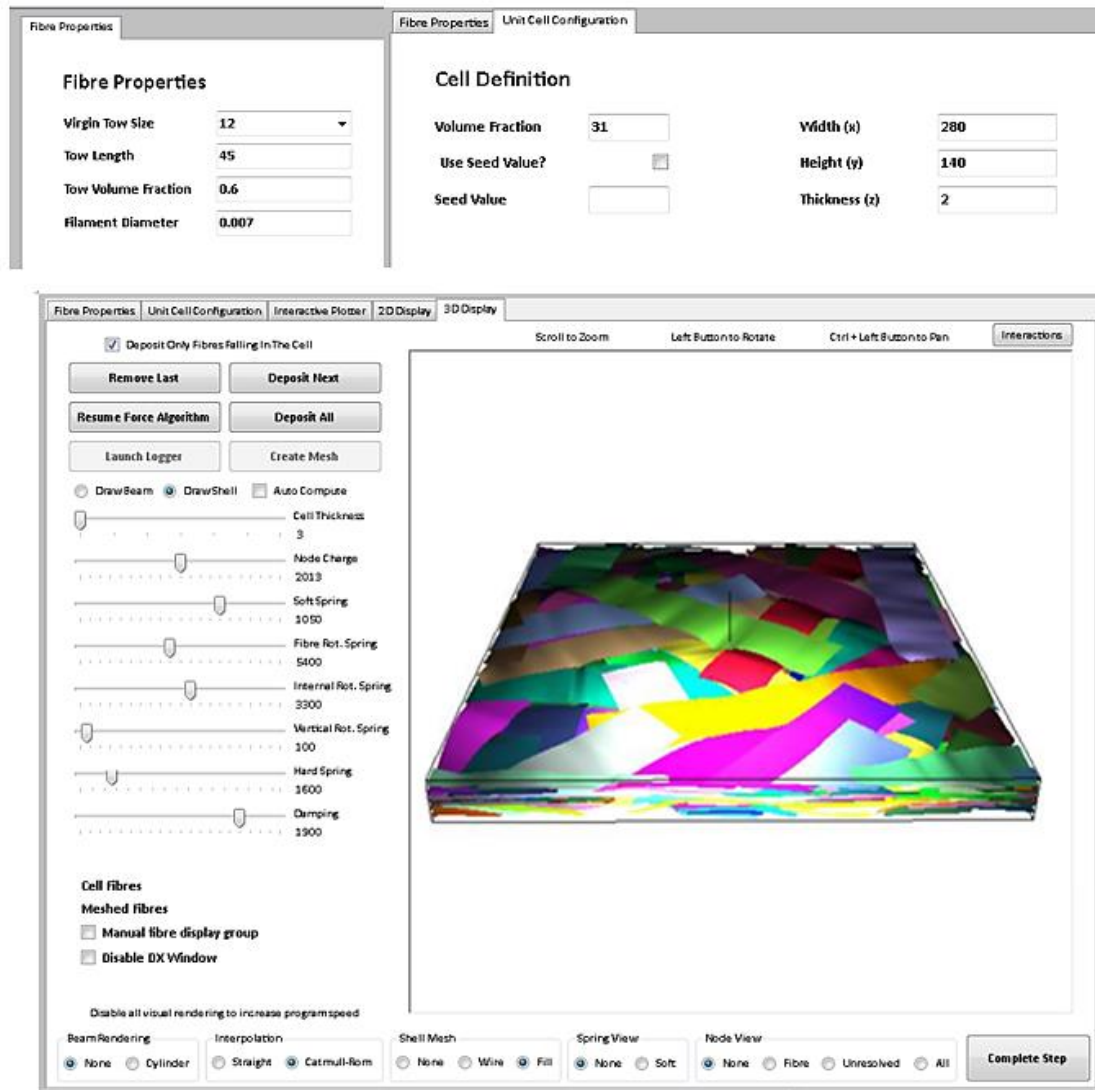


Figure 5.11 Screenshots from the 3D DCFP architecture generation programme to the procedures: Fibre properties and Model cell size definitions; 3D fibre architecture generation

When the fibre architecture generation is finished, an Abaqus input file containing nodal and element information is automatically created. The meshed fibre structure in Abaqus is shown in Figure 5.12.

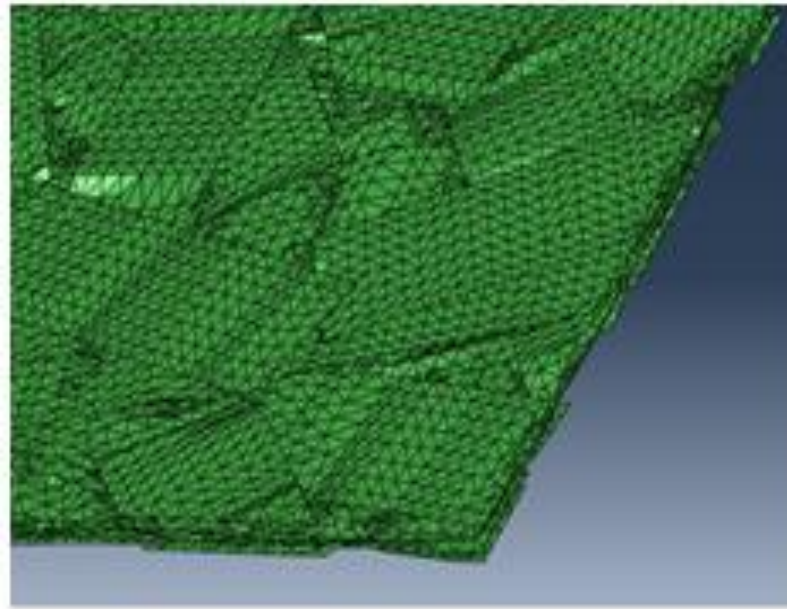


Figure 5.12 3D DCFP preform model generated in the fibre architecture generation programme

5.3.3 Fibre geometry analysis programme

A fibre geometry analysis programme (code in Appendix B) was developed in the present work to convert the information from the 3D model (coordinates and orientation) into a 2D shell model, as illustrated in Figure 5.13. 2D grids were generated containing the number of fibre bundles located in this grid, the orientation of each bundle and the through-thickness spacing between bundles.

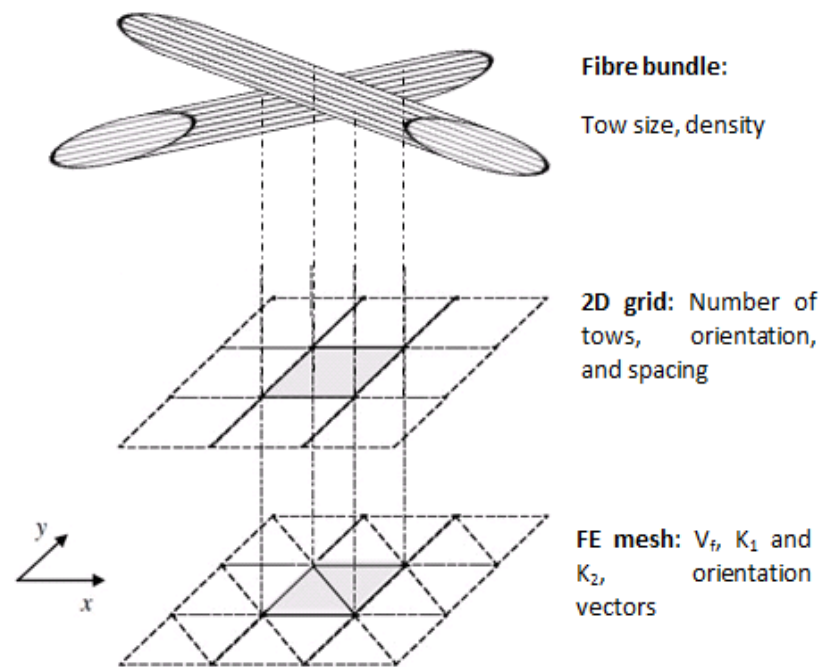


Figure 5.13 Derivation of the material parameters for finite element flow simulation from fibre bundle properties and geometric information

The procedure for analysing the 3D fibre architecture is listed below:

- 1) Firstly a regular 2D square grid is overlaid on the top surface of the representative volume element.
- 2) The coordinates of two corner points of a tow (point 1 and point 2 shown in Figure 5.14) are used to determine the orientation using simple trigonometric functions.

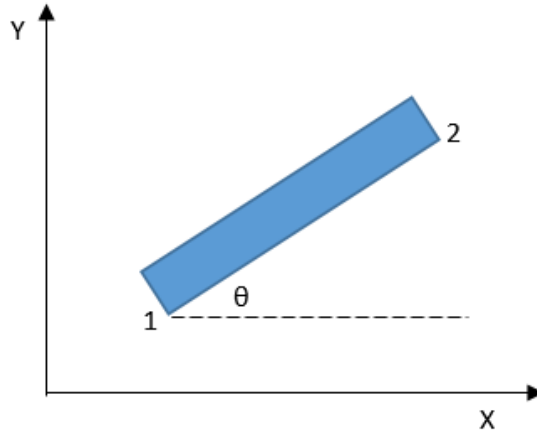


Figure 5.14 Schematics of orientation calculation for a fibre tow

- 3) The nodes from the meshed fibre architecture are used to determine the location of each fibre relative to the grid. The critical detail is to determine what percentage of a tow lies within any square of the grid if only one node is present. One node does not necessarily equate to 1 whole tow (Figure 5.15 (a)), as this will lead to the tow area being overestimated and consequently the fibre volume fraction. An area threshold was therefore determined to decide whether a tow should be counted in the grid or not. The threshold is an area ratio showing how much the area of a grid is covered by a fibre tow. If the area of a tow in a grid occupies more than the set area threshold, the tow is counted within this grid square (Figure 5.15 (b)). To calculate the area covered by a tow in a grid, in this thesis, each node is assigned to a certain area, so the number of nodes of a tow in a grid can be converted to the area of the tow. Furthermore, there are two further assumptions: nodes in a tow are evenly distributed, and every node represents the same tow area. In order to calculate the nodal area, a tow model with a certain width (W) and length

(L) for each type of fibre was generated and the number of nodes (N_n) in one tow was counted. Since element type STIR65 was used (a 6 noded triangular element), there were 3 nodes at the vertices and 3 mid-side nodes. The distribution of nodes in a part tow is schematically illustrated in Figure 5.16. It was assumed that each node represented an identical surface area of the tow, where the nodal area (NA) was calculated by:

$$NA = (W + \frac{1}{2}S_{seed})(L + \frac{1}{2}S_{seed})/N_n \quad \text{Equation 22}$$

where S_{seed} is the seed size in the fibre architecture generation programme. Half a seed size is added to both the length and width due to the presence of nodes on the fibre edges.

Hence, once the nodal number of a tow in a grid and the average node area are known, then the area of the tow in the grid can be calculated. If the area of the tow in the grid is larger or equal to the area threshold (grid area * threshold value (50%, for example)), the tow is counted as occupying the whole grid area. If not, the tow is not deposited within this grid element.

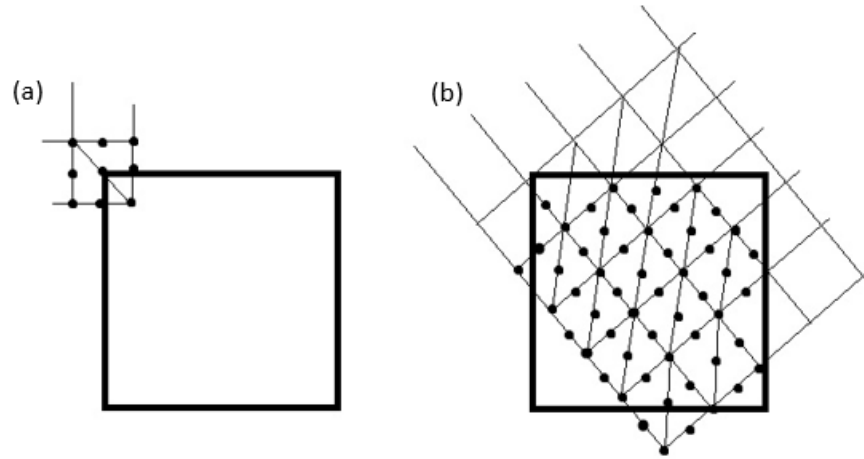


Figure 5.15 Schematics showing different area percentages of a tow in a grid. (a) if only small percentage of a tow locate in a grid, it does not equate the grid is filled with the tow, so this tow will not be counted in this grid; (b) if the area percentage of a tow in a grid is larger than an area threshold, it can be counted as the tow locates in this grid.

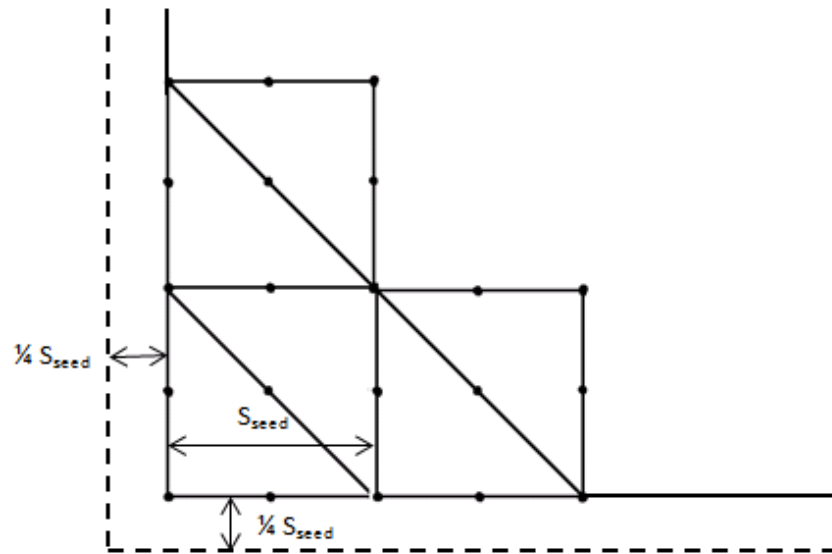


Figure 5.16 Schematic of nodes and elements distributions in a part of fibre bundle

In order to determinate the threshold value, three tow sizes of T700 carbon fibres were selected for investigation: 24K, 12K, and 6K. The mesh

information for all of the fibre architectures generated in this work are listed in Table 5.6. The width for each tow size was measured from the actual fibre.

Table 5.6 Fibre architectures generated in this work and their meshing information

No.	Tow size	Cell size (mm*mm*mm)	Fibre width (mm)	Fibre length (mm)	V _f	Seed size (mm)	Grid size (mm)	Nodal area (mm ²)
1	24K	280*110*2	9.4	50	10%	1.13	2.5	0.333
2	24K	280*110*2	9.4	50	31%	1.13	2.5	0.333
3	24K	280*110*2	9.4	50	50%	1.13	2.5	0.333
4	24K	280*110*2	9.4	30	31%	1.13	2.5	0.333
5	24K	280*110*2	9.4	100	31%	1.13	2.5	0.333
6	24K	140*55*2	9.4	50	50%	0.79	1.2	0.155
7	24K	140*55*2	9.4	50	50%	0.79	1.8	0.155
8	24K	140*55*2	9.4	50	50%	0.79	2.5	0.155
9	24K	140*55*2	9.4	50	50%	0.79	3.2	0.155
10	24K	140*55*2	9.4	50	50%	0.79	5.0	0.155
11	12K	140*55*2	4.6	50	40%	0.55	1.2	0.079
12	12K	280*110*2	4.6	50	20%	1.13	2.5	0.326
13	6K	140*55*2	2.4	50	20%	0.29	0.6	0.022
14	6K	280*110*2	2.4	50	10%	1.13	2.5	0.337

- 4) Finally the vertical spacings are calculated between the fibre tows. The vertical position of a tow is represented by the average Z coordinate values of all nodes of the tow in the grid. When the height positions of all the tows in the grid are known, the spacing between tow height positions (D_h) is simply calculated by subtracting one by one. In addition, the thickness of the tow (0.1646 mm) was also considered. If the spacing between heights are less or equal to the tow thickness, the tow spacing will be 0. Otherwise, the true spacing between tows (D_{tow}) is:

$$D_{tow} = D_h - 0.1646$$

Equation 23

The spacing between lower and upper mould surfaces was 2 mm. If the sum of the tow thickness in a grid was above 2 mm, all of the vertical inter-tow spacings are set to 0, assuming all fibres are touching and the filaments are distributed homogenously [94].

The output information of the fibre geometry analysis programme was written into a text file using the format as follows:

17 1 3 0.087266 1.25664 1.32645 0 0.668382 0.296616 0.472604

(1) (2) (3) (4)

- (1) Coordinate of the grid (X, Y)
- (2) Number of tows in this grid
- (3) Orientations of the tows in the grid (in radians)
- (4) Spacing between tows or between tow and mould wall (in mm)

When the output file was generated, it was imported into the permeability calculation programme to calculate permeability values for each element using Equation 14 – Equation 19.

5.3.4 Local permeability calculation

The local permeability calculation programme was initially developed by Endruweit et al. [105] to calculate the permeability of each element using assumed spacings between fibre bundles. This programme was modified to directly read in the spacing data output from the geometry analysis programme and then apply it in to Equation 14 – Equation 19 to calculate the permeability of each element in a PAM-RTM model.

The parameters used in the permeability calculation programme are listed in Table 5.7. Fibre density and diameter data come from T700 carbon fibre, while the c_1 , c_2 and V_{fmax} values are determined by the typical quadratic fibre packing. The k_1 and k_2 permeabilities of a fibre tow are reduced by the corresponding ratio listed in Table 5.4, when the effect of binder is included in the model.

Table 5.7 Parameters used in the Permeability calculation programme

Fibre density (kg/m³)	Fibre diameter (mm)	C₁	C₂	V_{fmax}
1800	0.007	1.78	0.40	78.5%

5.3.5 Flow simulations using PAM-RTM

The sizes of the finite element models created in PAM-RTM are listed in Table 5.6. One example (280 mm × 110 mm) is shown in Figure 5.17. The cavity height (H) was set as 2 mm. The left and right edges are the inlet and outlet respectively, whilst the top and bottom edges are set as the rigid mould wall. The five pink points, which are 250 mm from the inlet (left edge), are set as pressure sensors. A constant injection pressure of 1 bar is set on the inlet edge, while the pressure at the outlet is 0 bar to create a pressure differential ΔP . The viscosity of the resin (η) is set to 0.1 Pa.s

The time when the resin (indicated in red in Figure 5.17) reaches the five pressure sensors from the inlet is counted, and the average time is recorded and applied to Equation 17 to calculate the global permeability.

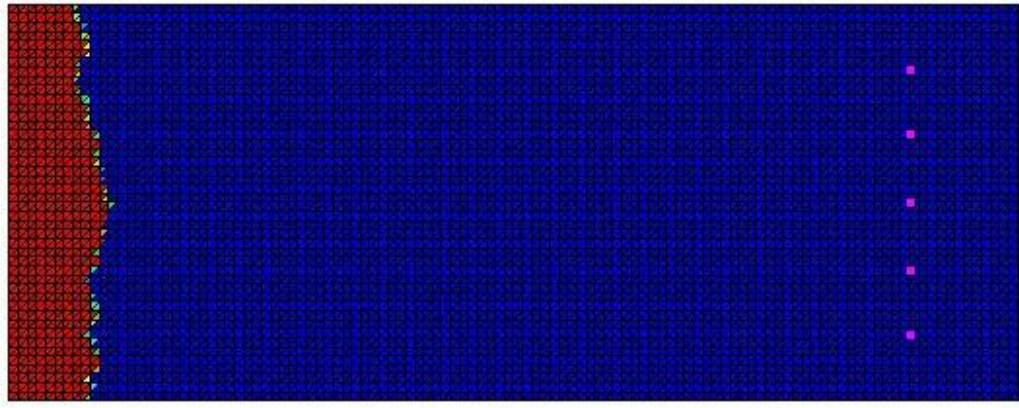


Figure 5.17 FE model in PAM-RTM (280 mm ×110 mm)

5.4 DCFP permeability model validation

Validation of the permeability model is presented in two stages: At the first stage, the fibre geometry analysis programme is validated to ensure that the pre-processor is able to produce accurate representations of the DCFP fibre architecture. At the second stage, the permeability simulation results from PAM-RTM are compared with the experimental DCFP permeability measurements.

5.4.1 Validation of fibre geometry analysis programme

The previous DCFP permeability model discussed in the literature [105] assumed the through-thickness spacings between the fibre bundles were uniform, which yielded unrealistic permeability predictions (over-predicted the experimental values by over 100% [94]). A 3D pre-processing tool has been used in the current work to generate more realistic random inter-bundle spacings. However, when converting this 3D architecture into a 2D architecture to facilitate the flow simulation in PAM-RTM, it is important to make sure the local fibre volume fraction is preserved. A regular square grid is projected onto the plan view of the 3D representative volume element (RVE)

and an algorithm determines how many tow segments are in each grid and also records the relative through-thickness tow spacings. Since this is a binary method, an area threshold value is set to establish if partial tow segments should be counted, as discussed in Section 5.3.3. The global V_f values from different area threshold values are illustrated in Figure 5.18 for different DCFP fibre architectures. The target global V_f was set as 31%, as indicated by the red horizontal line in Figure 5.18. The error between the actual recorded volume fraction and the target volume fraction is at its largest when no area threshold is used. The global fibre volume fraction is over-predicted by approximately 40% ($V_f=44\%$ rather than 31%). The magnitude of the error is also a function of the fibre length, with shorter fibre lengths (30mm) resulting in larger errors due to more tow segments per unit volume than longer fibre lengths. As the area threshold value increases, the error is reduced and the global fibre volume fraction approaches the target value. Figure 5.18 indicates that an area threshold of 70% is required to achieve a representative fibre volume fraction for all three fibre lengths investigated (30mm, 50mm, and 100mm).

In order to validate this value, the volume fraction for the range of fibre architectures listed in Table 5.6 were calculated and the results are listed in Table 5.8 below.

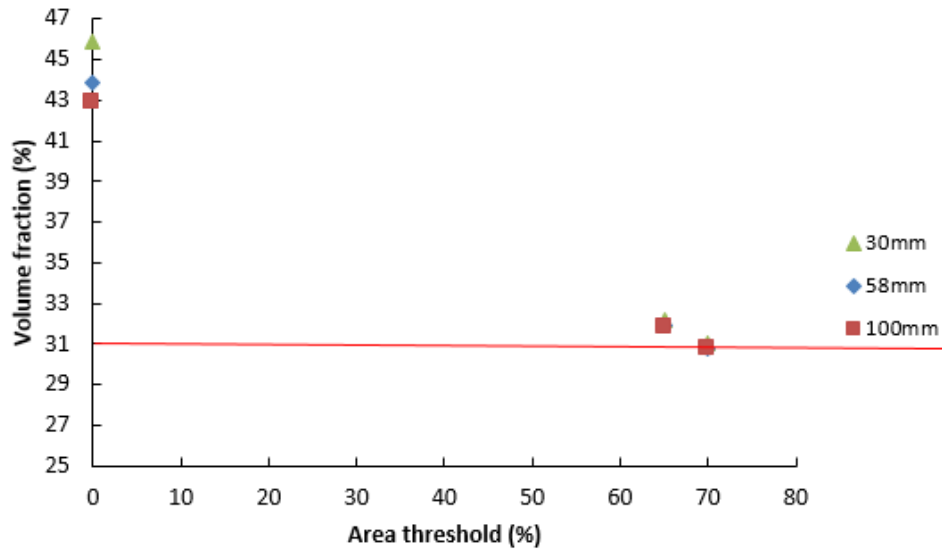


Figure 5.18 Global V_f of a 280mm×110mm×2mm 24K fibre DCFP preform. The target V_f (red line) is 31% for a range of fibre lengths (30mm, 50mm and 100mm) using different area threshold values

Table 5.8 Calculated V_f for different DCFP architectures by using 70% threshold value

Fibre architecture No.	Fibre type	Seed size (mm)	Grid size (mm)	Grid size / Seed size ratio	Global volume fraction (target)	Calculated volume fraction with 70% threshold	Error
1	24K	1.13	2.5	2.2	10%	9.8%	2.0%
2	24K	1.13	2.5	2.2	31%	30.8%	0.6%
3	24K	1.13	2.5	2.2	50%	51.5%	3.0%
6	24K	0.79	1.2	1.5	50%	48.7%	2.6%
7	24K	0.79	1.8	2.2	50%	50.0%	0.0%
8	24K	0.79	2.5	3.2	50%	48.2%	3.6%
9	24K	0.79	3.2	4.1	50%	47.2%	5.6%
10	24K	0.79	5.0	6.3	50%	41.5%	17.0%
11	12K	0.55	1.2	2.2	40%	40.9%	2.3%
12	12K	1.13	2.5	2.2	20%	20.5%	2.5%
13	6K	0.29	0.6	2.1	20%	21.0%	5.0%
14	6K	1.13	2.5	2.2	10%	15%	50.0%

The calculated error for most of the architectures is less than 5% if the area threshold value is set to 70%. The error values for fibre Architectures 1 to 3 indicate that the threshold is independent of the global volume fraction. The 70% threshold value works well when the Grid Size to Seed Size ratio is between 1.5 and 3.2, as the error

for the calculated volume fraction is less than 5%. The error for Architecture 14 is 50%, as the seed size (1.13mm) is too large in comparison to the width of the 6K tow (2.4mm). Consequently, only two or three nodes are located across the fibre width, which leads to a poor mesh quality as shown in Figure 5.19. When a finer seed size (0.29mm) and grid size (0.6mm) are used for the 6K fibre architecture (Architecture No.13), the error is back within the acceptable range ($\leq 5\%$).

A similar situation occurs for Architecture 10, with a reported error of 17% between the simulated fibre volume fraction and the target value. This is also due to the large grid seed size (5 mm) in comparison to the width of the 24K tow (9.4 mm), causing the area of the tow to be underestimated (Figure 5.20 (b)). The error is reduced to 3.6% when the grid size is reduced by 50% to 2.5mm (Architecture No. 8), which indicates the importance of selecting the correct seed size and grid size. Whilst smaller grid sizes improve accuracy, they consequently increase computation time. From Table 5.9, it can be seen that the CPU time varies significantly with different grid sizes. For instance, the computing time increases by almost a factor 10 times (from 28s to 267s) when the grid size is reduced from 2.55mm to 1.2mm.

A relationship among seed size (S_s), grid size (S_g), and width of fibre tow (W) can be expressed as:

$$C_1 \times S_s \leq S_g \leq \frac{W}{C_2} \quad \text{Equation 24}$$

where C_1 and C_2 are both constants. This equation ensures that the selected grid size can provide good resolution for each fibre tow and the seed size can provide sufficient detailed information of fibre to each grid. Based on the results discussed

above, the recommended values for C_1 and C_2 are 2.2 and 3.8 respectively through considering accuracy and computing time.

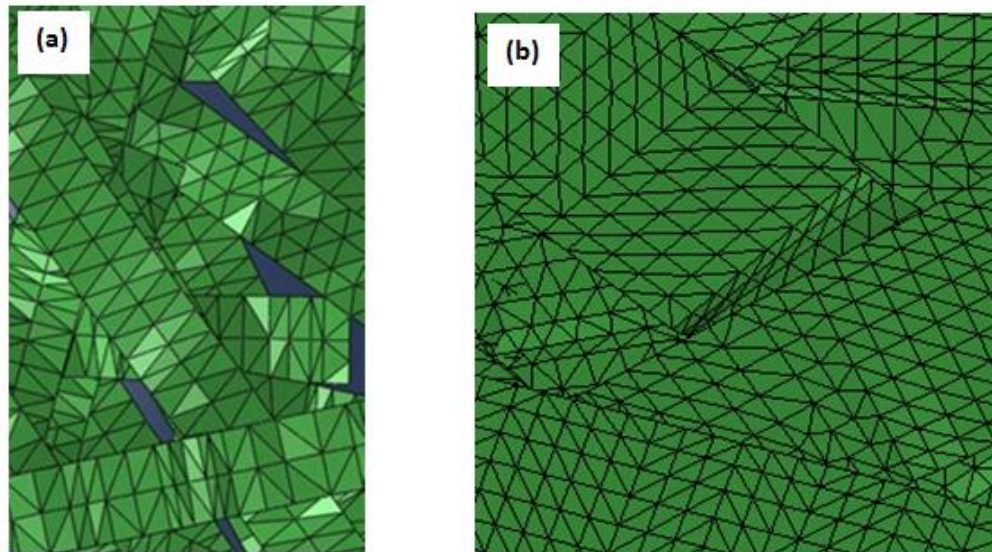


Figure 5.19 Node distributions and element shapes in (a) 6K fibre architecture (b) 24K fibre architecture. The seed size is 1.13mm and grid size is 2.5mm for both architectures

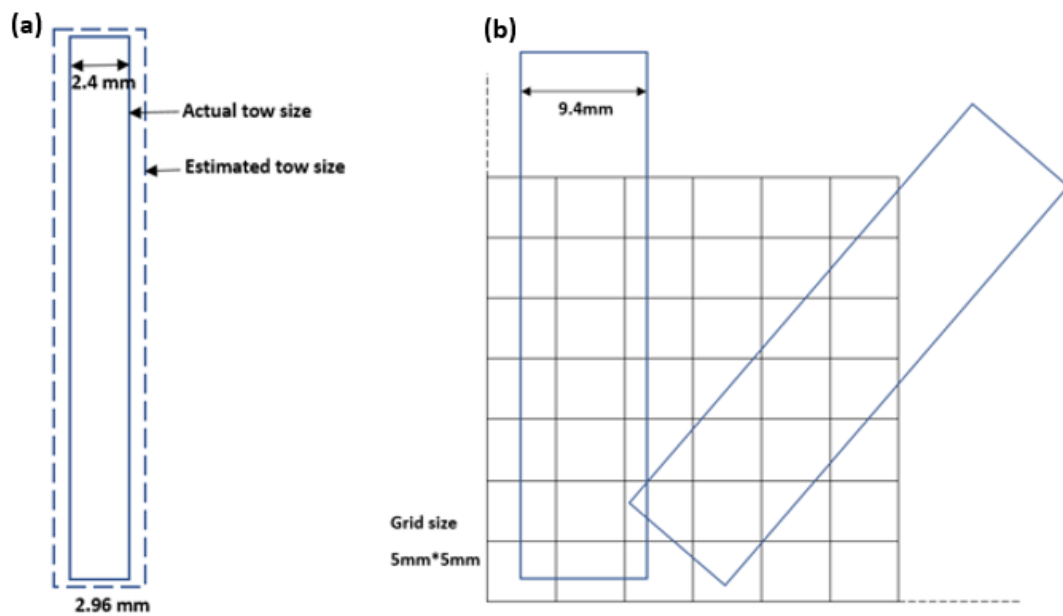


Figure 5.20 Schematics showing the main errors in Architecture No.14 (a) (over-estimation) and Architecture No.10 (b) (under-estimation)

Table 5.9 Computing time at different grid sizes for the 24K fibre (9.4mm wide) architectures (Architecture No. 6 – 10 in table)

Grid size (mm)	1.2	1.8	2.5	3.2	5.0
Fibre tow width to grid size ratio	7.8	5.2	3.8	2.9	1.9
Computing time (s)	267	55	28	17	7

Note: The specification for the computer used in this work is: CPU Core i3-4130 3.4GHz and RAM 32GB.

The next step is to check whether the flow simulation results in PAM-RTM are able to correctly reflect the variation of the fibre bundles in the permeability value for the different DCFP architectures. Firstly, a 3D DCFP model was generated in the Architecture Generation Programme. Then the local areal mass of fibres was plotted using a grey-scale (darker places indicate higher local fibre content). This fibre map was imported into PAM-RTM to perform resin flow simulations for calculating the simulated permeability, which was introduced in Section 5.3.5. Figure 5.21 shows that the flow front is irregular and is influenced by the local fibre distribution within the preform. Flow is hindered by the high fibre content regions, encouraging the resin to flow faster through the low V_f regions as observed experimentally in Figure 5.7.

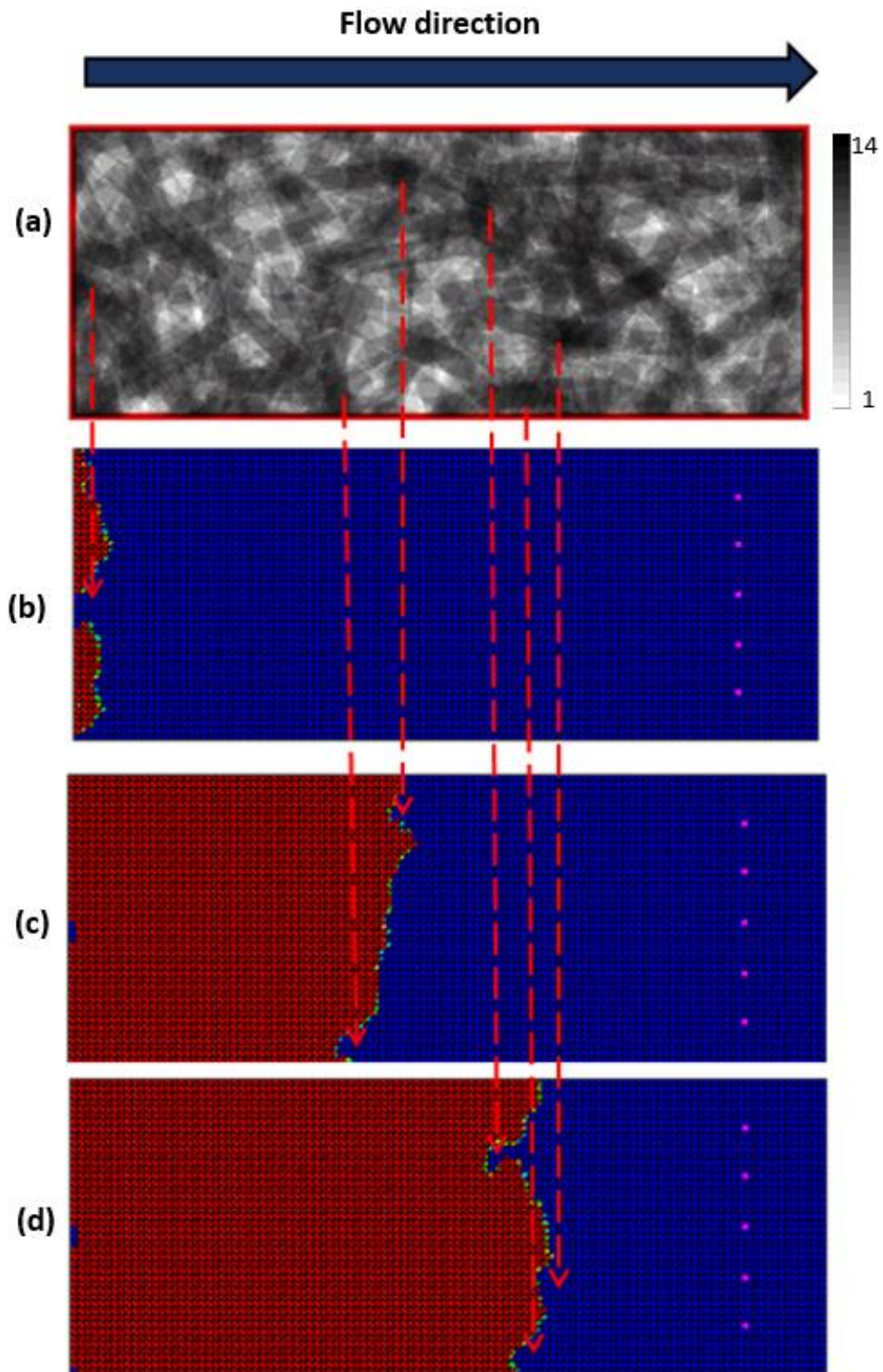


Figure 5.21 Fibre distribution of a DCFP model (a) and profiles of flow front during advancing process in PAM-RTM (b) – (d); Cell size 280 mm * 110 mm

5.4.2 Predicted DCFP permeability results

Figure 5.22 shows the simulation results of the cumulative average permeability values for a 12K 45mm V_f 31% 5wt.% DCFP architecture. A new DCFP model was created using the same material parameters for each iteration. Since the 3D DCFP architecture generation programme does not generate the same level of variability as found in experimental specimens, the simulation results converged quickly after 3 iterations, and all of the values were in a narrow range ($15 - 16 \times 10^{-10} \text{m}^2$). This is because the target fibre volume fraction of 31% was always achieved for the simulation specimens (280 mm x 110 mm), whilst the V_f of the experimental specimens was more variable in the range of 30% - 32%.

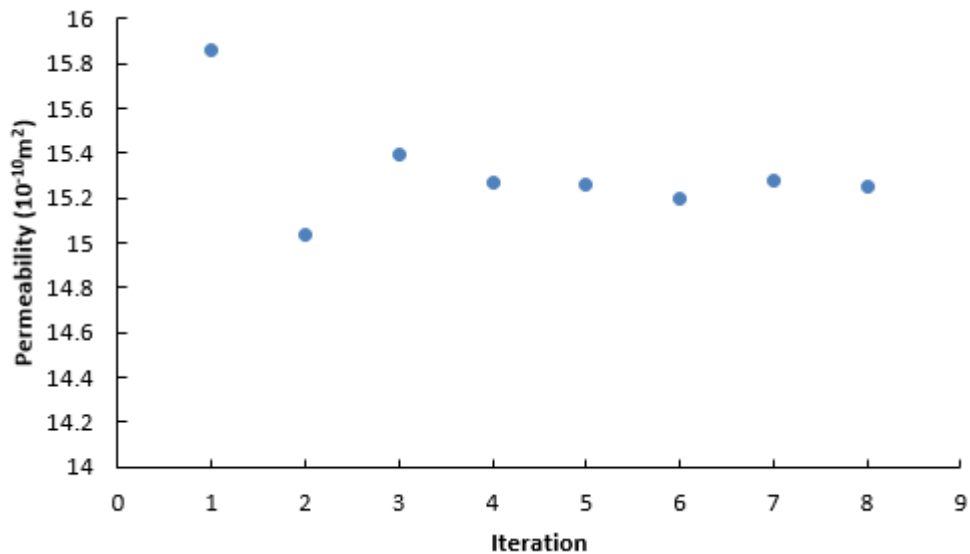


Figure 5.22 Cumulative average DCFP permeability values from FE simulation in PAM-RTM

Table 5.10 compares the results of the permeability simulation for the DCFP structures at two V_f levels (31% and 46%) using different two modelling methods, against the experimental data. It can be seen that the simulation values using both the 2D beam element model (assuming fibre bundles are evenly distributed in

thickness direction) [105] and the 3D model (with random spacing between fibre bundles in thickness direction) developed in this thesis have large errors compared to the experimental values. The 2D fibre model with even spacing between bundles underestimated the permeability of DCFP by ~40%, while the 3D model overestimated the permeability by ~100%.

The inaccuracy of the 2D beam model can be attributed to assuming all fibre bundles are evenly distributed through the thickness of the preform. The expression for the permeability of the inter-bundle spacings in Equation 19 indicates that, if the number of fibre bundles is constant, increasing the number of spacing between bundles by assuming there are no touching bundles (even spacings) reduces the spacing-related permeability factor $(\sum_{j=1}^M \frac{h_j}{T_m} \frac{h_j^2}{12})$, which leads to a lower permeability.

The simulated permeability values from the 3D models are approximately twice as high as the experimental data. However, the trend for the effect of binder content on the permeability at different carbon fibre volume fractions was correctly accounted for in the simulation, supporting the experimental data. The effects of binder content at different V_f have been explained in Section 5.2.3. The reason for the overestimation from the 3D model can be attributed to 2 things: assuming the fibre distribution is planar (overlooking out-of-plane fibre angles), and the homogeneity of the binder.

The out-of-plane fibre angles were overlooked in the fibre geometry analysis programme, therefore the resin flow is not hindered by fibres passing through the thickness of the preform. Furthermore, in this model, the negative effect of binder on permeability from the experimental data of NCF was applied to the input values

for the tow permeabilities, k_1 and k_2 , but this does not account for local agglomerations on the surface of the bundles, as shown in Figure 4.15. Hence, the binder can block inter-bundle spacing, which results in lower permeability.

Table 5.10 Comparison of permeability values of the DCFP (12K 45mm) with different V_f and binder content from experimental measurement, 2D and 3D models

Permeability γ $\times 10^{-10} \text{ m}^2$	Experimental	3D model*	2D model*	Experimental	3D model*	2D model*
Binder content V_f	5 wt.%			10 wt.%		
31%	6.32 ± 1.92	12.25 ± 0.48	3.93 ± 0.22	4.59 ± 1.13	9.67 ± 0.51	2.94 ± 0.19
46%	1.34 ± 0.45	3.41 ± 0.43	0.83 ± 0.13	1.13 ± 0.33	2.82 ± 0.45	0.75 ± 0.12

*The 3D model was developed in this thesis to account for the random spacings between the fibre bundles in the through-thickness direction. Whilst the 2D model assumes the fibre bundles were evenly distributed through the thickness [88].

5.5 Conclusions

In this chapter, thirty permeability measurement repeats were conducted for a single type of DCFP (T700 12K 45mm EPS620 10wt.% V_f 31%), and it was found that at least ten measurements should be taken to achieve an average permeability value to overcome the statistical effects of areal mass variability. The presence of powder binders significantly influences the permeability of DCFP preforms, when typical amounts are added to overcome preform distortion during high pressure RTM. The distribution of coarse binders is less homogenous than that of fine binders, which influences the resin flow front in high fibre content regions of the preform. At a binder content of 5 wt.% and a carbon fibre V_f of 31%, the permeability of the DCFP with EPS620 (particle size 100 μm) was approximately half that of a DCFP preform with Neoxil940 (particle size 900 μm): $6.32 \times 10^{-10} \text{ m}^2$ VS $11.49 \times 10^{-10} \text{ m}^2$. When the

binder content was increased to 10 wt.%, the permeabilities of preforms produced with EPS620 and Neoxil940 reduced by 27% and 55% respectively. However, when the V_f increased to 46%, the effect of binder content on permeability was less significant. A 15% reduction in permeability was observed for DCFP preforms with 5wt.% and 10 wt.% EPS620 binders.

A permeability model was developed with the consideration of realistic inter-bundle spacing created by a 3D DCFP architecture generation programme. The aim of this model was to account for 3D fibre architecture features (e.g. fibre tow location, number of tows, orientation, and spacing) in a simplified 2D permeability calculation to achieve a representative global permeability value for DCFP. It was found that an area threshold of 70% was required to ensure the V_f in the 2D model was the same as the V_f originally specified in the 3D model.

Whilst the results of the flow simulation in PAM-RTM showed that the model developed in this chapter successfully simulated the irregular flow front observed in the experiments, the simulated global permeability values were 100% higher than the experimental data. The error in the permeability simulation using the 3D DCFP model can be attributed to ignoring the effect of out-of-plane fibres and assumptions about the binder distribution. The simulation results from the newly developed 3D model and the previous 2D model provide effective upper and lower bounds respectively for the permeability of DCFP preforms.

Chapter 6 Structural investigations of DCFP using high strength and high modulus carbon fibres

Previous experimental studies for DCFP have highlighted that fibre homogeneity (local areal mass distribution) dominates in terms of mechanical properties [64, 65]. Homogeneity can be improved by reducing the fibre length, but this increases the likelihood of bundle fragmentation, which limits the maximum achievable fibre volume fraction due to increased preform loft. The other option is to reduce the tow size, but this has a significant impact on fibre cost, which increases exponentially as tow size reduced. This chapter investigates the possibility of using higher performance fibres, other than the industrial grade fibres typically used, to see if higher mechanical properties can be realised for DCFP.

6.1 Materials

Five types of carbon fibre tow were selected to investigate the effect of fibre properties on the mechanical performance of discontinuous fibre reinforced components. The fibre modulus ranged from 230GPa to 760GPa and the ultimate strength ranged from 3200MPa to 5490Mpa. The objective of this study was to understand the implications of using higher performance fibres in discontinuous fibre composites to see if there was an optimum in terms of cost (ranging from 24 €/kg – 270 €/kg). Detailed specifications of the fibres used and the preforms designed to achieve a 50% fibre volume fraction are listed in Table 6.1. The preform areal density was dependent on the fibre type, as each fibre had a different linear density due to

different filament diameters and tow sizes. The target areal densities are listed in Table 6.1 for all fibre types investigated.

A homogeneity factor was calculated for each fibre type, based on the target areal density of the preform and the linear density of the tow. Equation 25 was used to calculate the number of fibre bundles in an area of 1 cm² and the results are presented in Table 6.1.

$$\text{Homogeneity factor (tows/cm}^2\text{)} = \frac{\text{Areal density of preform (gsm)}}{10000 \times \text{Linear density of fibre } \left(\frac{\text{g}}{1000\text{m}}\right) \times 0.045} \quad \text{Equation 25}$$

Three hybrid plaques were also produced using different ratios of Fibre 1 and Fibre 5. Hybrid preforms were all sprayed with alternating layers of Fibre 1 and Fibre 5 (6 layers and 5 layers in total respectively), but the areal mass of each layer was adjusted to achieve the desired fibre ratio and to maintain a 50% V_f. The specifications for these plaques are also listed in Table 6.1.

Table 6.1 Specification of fibre types and corresponding DCFP preforms

	Fibre type	Manufacturer	Precursor	Tensile strength (MPa)	Tensile Modulus (GPa)	Filament Diameter (μm)	Density (g/cm^3)	Yield ($\text{g}/1000\text{m}$)	Cost ($\text{€}/\text{kg}$)	Target preform areal density (gsm)	Homogeneity factor (tows/cm^2)
Fibre 1	T700-50C-12K	Toray	PAN	4900	230	7	1.80	800	24	2430	6.8
Fibre 2	T800HB-12K	Toray	PAN	5490	294	5	1.81	445	147	2444	12.2
Fibre 3	K13312-12K	Mitsubishi	Pitch	3200	420	9.5	2.06	1560	75	2781	4.0
Fibre 4	M46J-6K	Toray	PAN	4210	436	5	1.84	223	270	2484	24.8
Fibre 5	K13916-16K	Mitsubishi	Pitch	3200	760	9.5	2.15	2200	80	2903	2.9
	Fibre combination			Volume ratio			Nominal density (g/cm^3)	Nominal yield ($\text{g}/1000\text{m}$)	Nominal fibre cost ($\text{€}/\text{kg}$)	Target preform areal density (gsm)	
Hybrid 10	K13916/T700			10:90			1.84	940	30.6	2477	
Hybrid 25	K13916/T700			25:75			1.89	1150	40.0	2548	
Hybrid 50	K13916/T700			50:50			1.98	1500	54.5	2666	

6.2 Effects of fibre properties on strength and stiffness of DCFP

Representative stress-strain curves are presented in Figure 6.1 for DCFP plaques manufactured from the five fibre types listed in Table 6.1. All materials exhibit a linear stress/strain response up to failure. DCFP plaques manufactured from Fibre 2 and Fibre 4 have the highest tensile strength (~ 300 MPa) and stiffness (~ 60 GPa) respectively among all the fibre types selected. Compared to Fibre 2, the Fibre 1 DCFP plaque offers similar properties, but with slightly lower strength and stiffness. Although the stiffness of Fibre 5 DCFP is comparable with the Fibre 2 DCFP, the strength is the lowest (lower than 100 MPa). The Fibre 3 DCFP plaques do not show any significant advantages in terms of strength and stiffness, compared to the DCFP plaques manufactured from other fibre types. The magnitude of the strength and stiffness will be discussed in the two following sections.

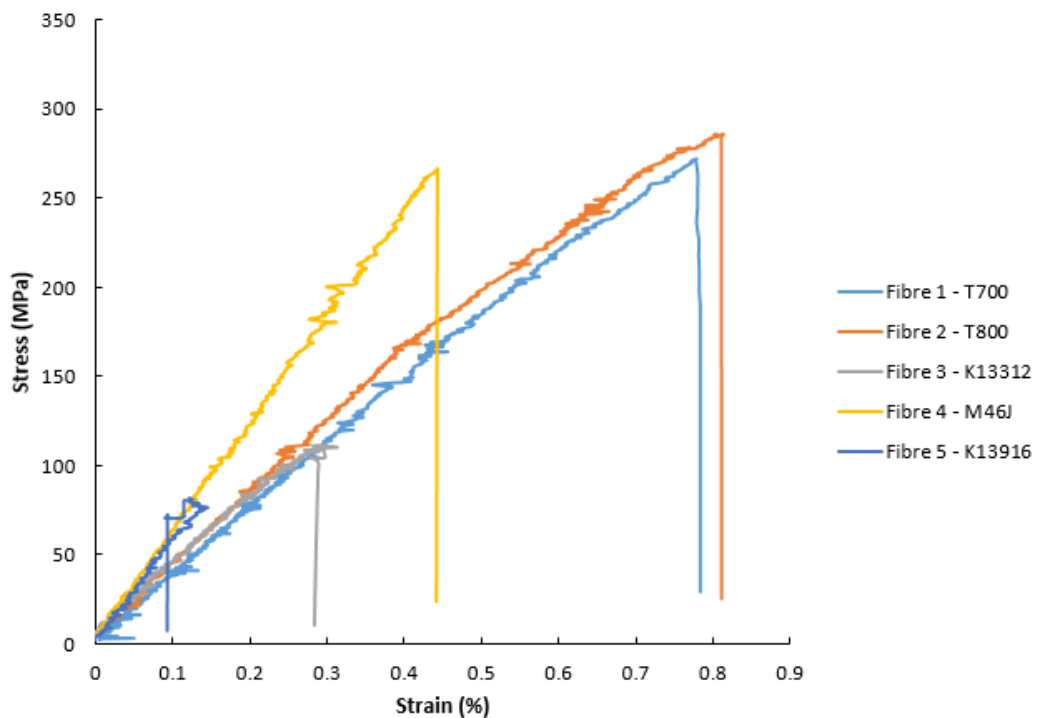


Figure 6.1 Representative stress-strain curves of DCFP plaques manufactured from different fibre types selected to investigate

6.2.1 Strength

Figure 6.2 shows the tensile and compressive strengths of DCFP plaques moulded by RTM as a function of the ultimate tensile strength of the fibre, for the five different fibre types. In general, there is very close agreement (<5% difference) between the composite tensile strength and compressive strength values for all fibre types. The coefficient of variation is also less than 8% in each case.

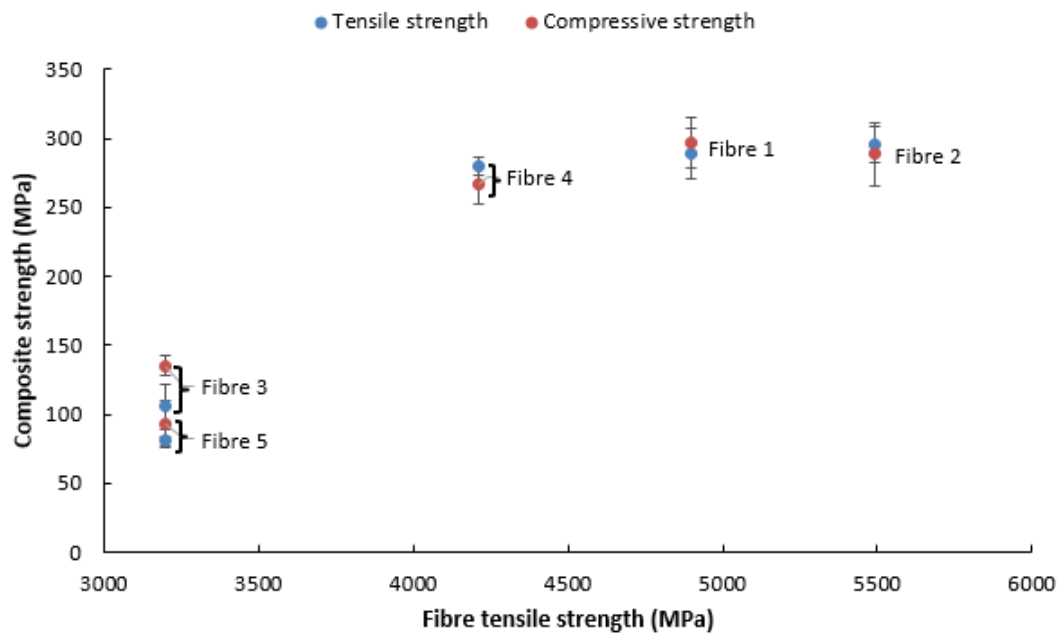


Figure 6.2 Strength of RTM moulded DCFP parts using various fibre types with different tensile strengths

The composite strengths are similar for Fibre 5 and Fibre 3, since they are both manufactured with Pitch-based fibres with the same tensile strength (3200 MPa). The composite tensile strength of these plaques however is low, being the same order of magnitude as the ultimate tensile strength of the epoxy resin [110]. The difference in composite strength of plaques made with Fibre 5 and Fibre 3 is due to

the tow size, which is reflected in the homogeneity factor presented in Table 6.1. Fibre 5 has the largest tow size of all fibre types tested (16K), but also has the largest filament diameter (9.5 μm), resulting in only 2.9 tows/ cm^2 for a 50% V_f plaque moulded in a 2.7mm thick cavity. The tow size for Fibre 3 is 12K, resulting in 4.0 tows/ cm^2 , which helps to improve the homogeneity of the fibre distribution, as previously discussed in [87].

Because of the low homogeneity of the Fibre 5 architectures, the variation in V_f of the moulded plaques is high (13.2%), as indicated in Table 4.9. Hence, there are more low fibre content regions and resin-rich areas in these plaques, leading to lower strength values. The tensile specimens start to fail in the resin rich regions and then propagate around fibre boundaries of neighbouring bundles. From Figure 6.3 (a) the outline shape of fibre bundles are evident at the fracture surface of the tensile specimens. Micrographs in Figure 6.3 (b) confirm that tensile failure of Fibre 5 specimens is by fibre pull-out, as individual filaments are exposed without any surrounding matrix material. Conversely in compression, specimens manufactured from Fibre 5 failed due to buckling (Figure 6.3 (c)) due to the asymmetry of the specimens caused by the presence of resin rich regions.

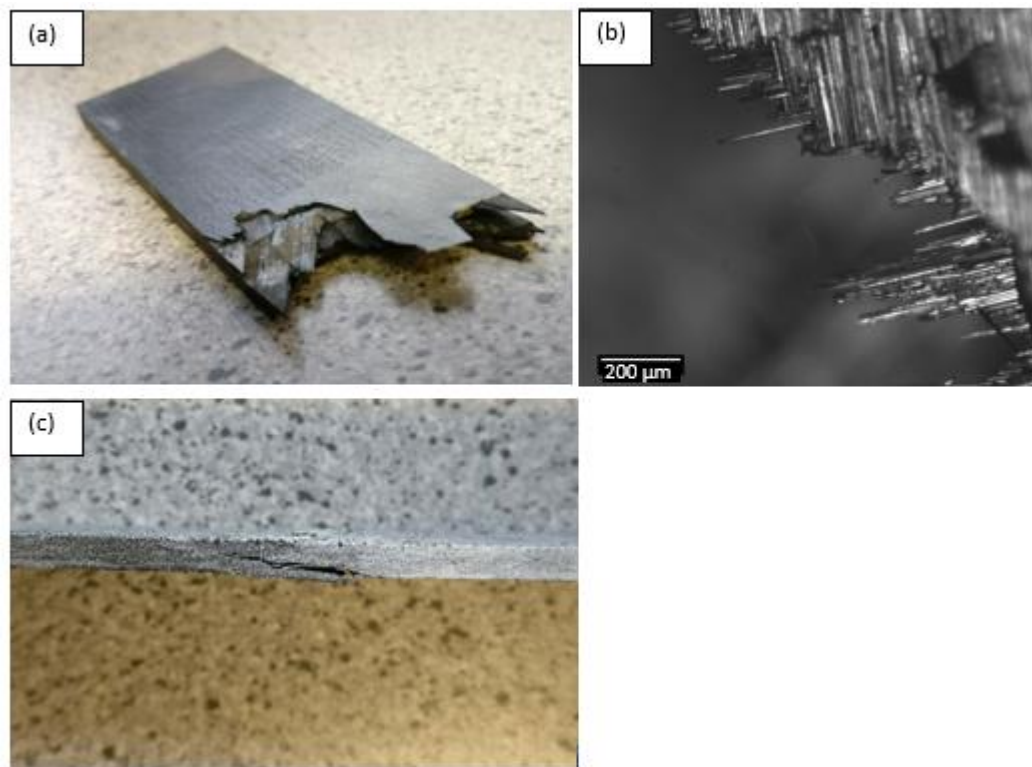


Figure 6.3 Morphology of fracture surface for tensile specimen made with Fibre 5 (a); Photograph of the fracture site (b) Micrograph of the fracture surface (c); fracture site of Fibre 5 specimen in compression

The composite strength increases by $\sim 180\%$ (from $\sim 100\text{MPa}$ to 280MPa) when the tensile strength of the carbon fibre increases by 32% from 3200MPa (Fibre3 and Fibre5) to 4210MPa (Fibre4). Fibre 4 has the highest homogeneity factor (24.8tows/cm^2) of all the fibres tested, but this does not result in the highest composite strength recorded, as the composite strengths of Fibre 1 and Fibre 2 are higher. The fibre strengths for Fibre 1 and Fibre 2 are higher than Fibre 4, which suggests that fibre strength dominates the composite properties over the homogeneity of the fibre distribution. In addition, the void content is higher for Fibre 4 ($\sim 1.0\%$) than Fibres 3 and 5 according to Figure 6.4. These are macroscale voids, as shown in Figure 6.5, which are situated between bundles and at fibre ends. Macroscale voids are formed because the inter-bundle spacing is smaller due to the higher homogeneity number,

which reduces the resin velocity during injection and therefore reduces the capillary number [111-114].

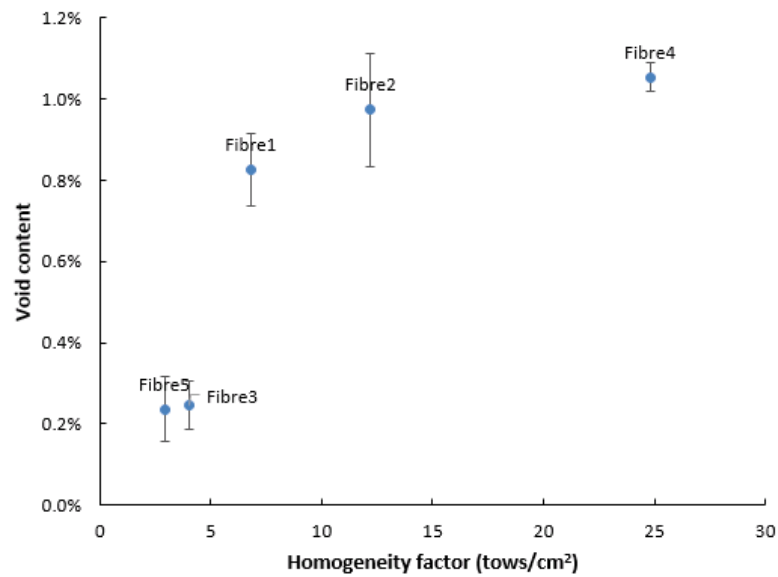


Figure 6.4 Void content of RTM moulded DCFP plaques as a function of homogeneity factor

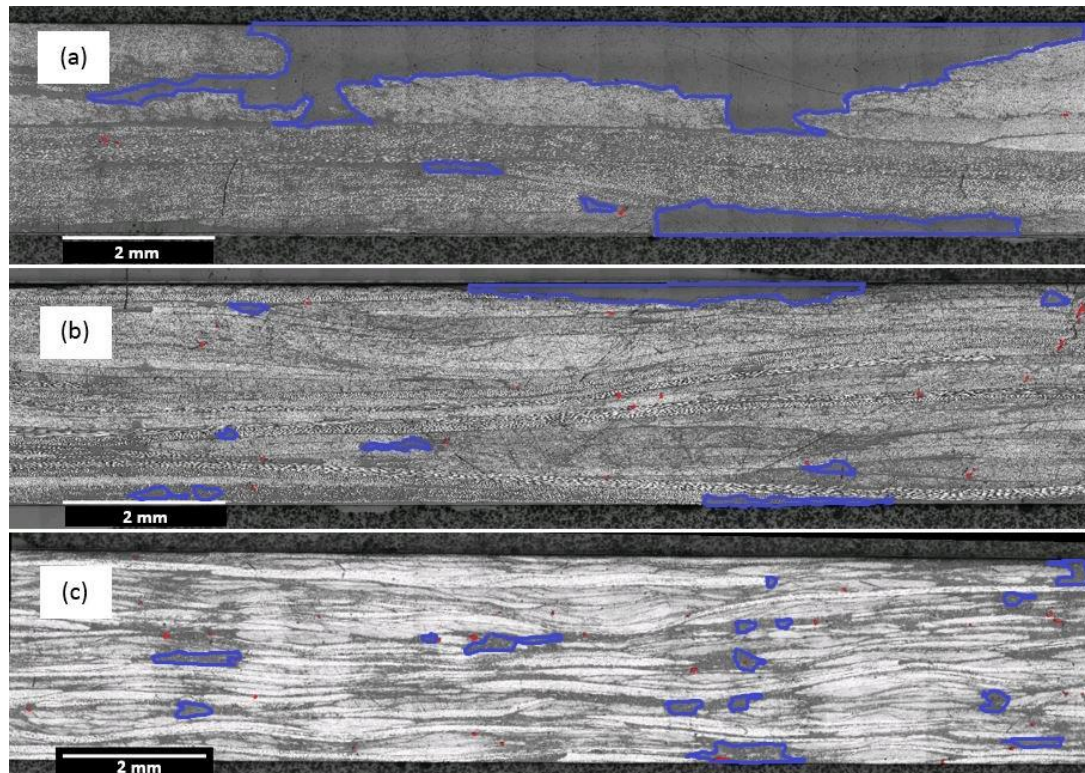


Figure 6.5 Microscopy images ($\times 5$ magnification) showing fibre distribution for RTM moulded DCFP plaques manufactured from (a) Fibre 5 - K13916 (b) Fibre 1 - T700 and (c) Fibre 4 - M46J; Blue lines and red dots indicate the resin rich regions and voids

There is a marginal increase (3%) in composite strength between Fibre 4 and Fibre 1, as the fibre strength increases from 4210 MPa to 4900 MPa, with a further 2% increase in composite strength as the fibre strength increases further to 5490 MPa for Fibre 2. The maximum composite strength converges to ~300 MPa, which is similar to other values reported in the literature [54, 62] for random carbon fibre plaques containing 50% V_f . The strength of a discontinuous fibre material will rarely exceed 70% of the strength of an equivalent continuous fibre system [115], but the discontinuous fibre plaques made from Fibres 1, 2 and 4 here are just 30 – 35%. In [115], the tensile strength doubles when fibre bundle aspect ratio (length/width) increases from 100 to 500, and then reaches a plateau as the aspect ratio increase further. However, the bundle aspect ratio is between 10 and 30 for the DCFP materials tested here, which suggests that the full potential of the fibres was not fully used. Furthermore, a higher-stiffness matrix may be required to reduce the overall stiffness ratio of fibre/matrix, as Kardos [115] previously demonstrated that this can improve the overall strength of the composite by reducing the large stress gradient at bundle ends.

6.2.2 Stiffness

Figure 6.6 shows the composite moduli as a function of the fibre tensile modulus for the different fibre types. An analytical model [87, 116] has been used to predict the theoretical stiffness, which is based on a Mori-Tanaka approach [117]. The PAN-based fibres (Fibre1, Fibre2, and Fibre4) follow the analytical trend, as the composite stiffness increases with increasing homogeneity factor and increasing fibre tensile modulus. However, the discrepancy between the prediction and the experimental

data increases as the fibre stiffness increases. The Pitch-based fibres (Fibre 3 and Fibre 5) yield similar composite moduli, despite the fibre modulus for Fibre 5 being almost double that of Fibre 3. There is also much greater variability for the measured moduli for these plaques and the compressive stiffness is only ~60% of the tensile stiffness. During the preforming stage, Fibre 3 and Fibre 5 are easy to break to create shorter and smaller bundles when the fibre tows pass through the chopping system, as they are brittle and have a very low strain to failure (~0.4%). Therefore, the fibre bundle aspect ratio will become smaller, which causes a significant reduction in the composite stiffness [115].

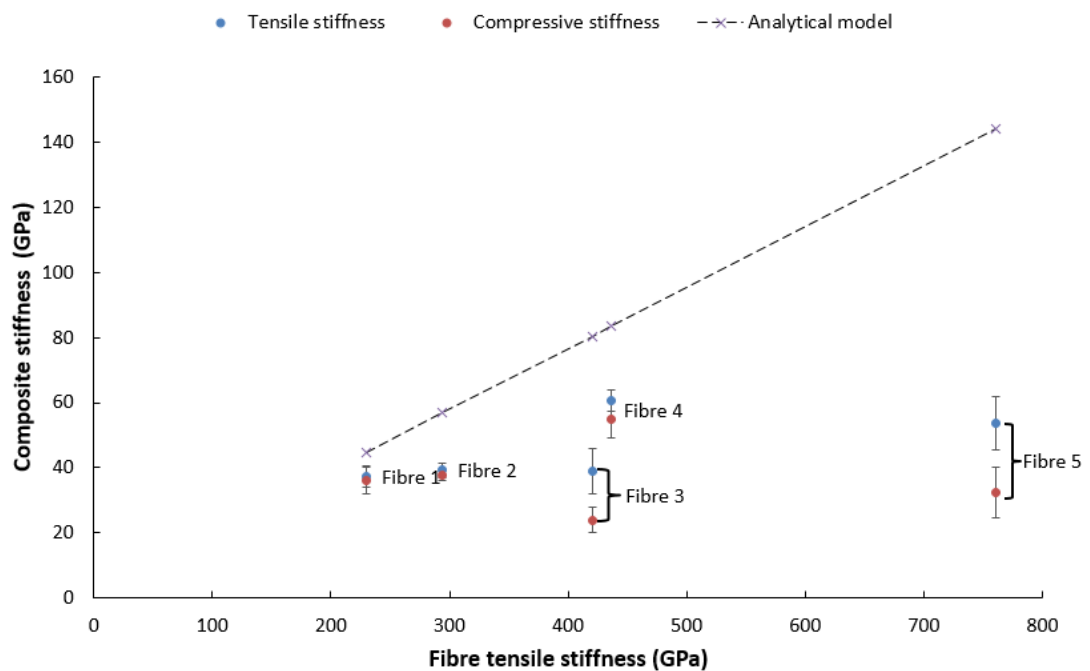


Figure 6.6 Stiffness of RTM moulded DCFP plaques consisting of different fibre types

6.3 Effects of fibre hybridisation

According to the strength data presented in Figure 6.2, the ultimate strength converges to approximately 300 MPa as the fibre strength increases, when combined

with the current matrix system. An obvious trend cannot be distinguished for the stiffness however, with high stiffness fibres such as Fibre 5 (760 GPa) yielding a lower composite modulus than lower stiffness Fibre 4 (436 GPa). Some hybrid fibre plaques have been manufactured using a combination of Fibre 1 and Fibre 5, to try to achieve a compromise between composite stiffness and cost.

Figure 6.7 and Figure 6.8 show the composite strengths and moduli of DCFP plaques manufactured with different ratios of Fibre 1 and Fibre 5 respectively. The properties of the hybrid DCFP plaques are dominated by two factors: the properties of the fibres and the degree of dispersion [68, 118], related to the homogeneity factor. Low homogeneity levels will limit the potential of the fibres with higher properties, as discussed in the previous section. According to Figure 6.7, the composite strength follows a near-linear relationship with increasing levels of Fibre 5, reducing from 300 MPa at 0% to ~100 MPa at 100%, since Fibre 5 has lower fibre tensile strength (3200 MPa). The trend is similar for both tensile and compressive data. When the content of Fibre 5 increases from 25% to 50%, there is a significant reduction in composite strength, because of the difference in strain to failure of the two fibres (0.4% for Fibre 5 and 2.1% for Fibre 1). A similar reduction in strength was observed in [72], when two fibres (M40/T300) with different failure strains were blended together with equal volume fractions (50%:50% in a hybrid composites).

The trend for the composite stiffness in Figure 6.8 however is distinctly different. There is no obvious hybridisation effect for the compressive modulus, exhibiting a straight line for different hybridisation levels, since the stiffness of the pure Fibre 1 and Fibre 5 DCFP plaques are the same. The tensile modulus initially increases by 31%

(from 38 GPa to 50 GPa) as the Fibre 5 content increases from 0 to 10%. A further 10% increase in composite stiffness is observed as the Fibre 5 content increases to 25%, yielding a peak composite stiffness of 56 GPa. The composite stiffness plateaus beyond the 25% hybrid level, with an average stiffness of 54 GPa.

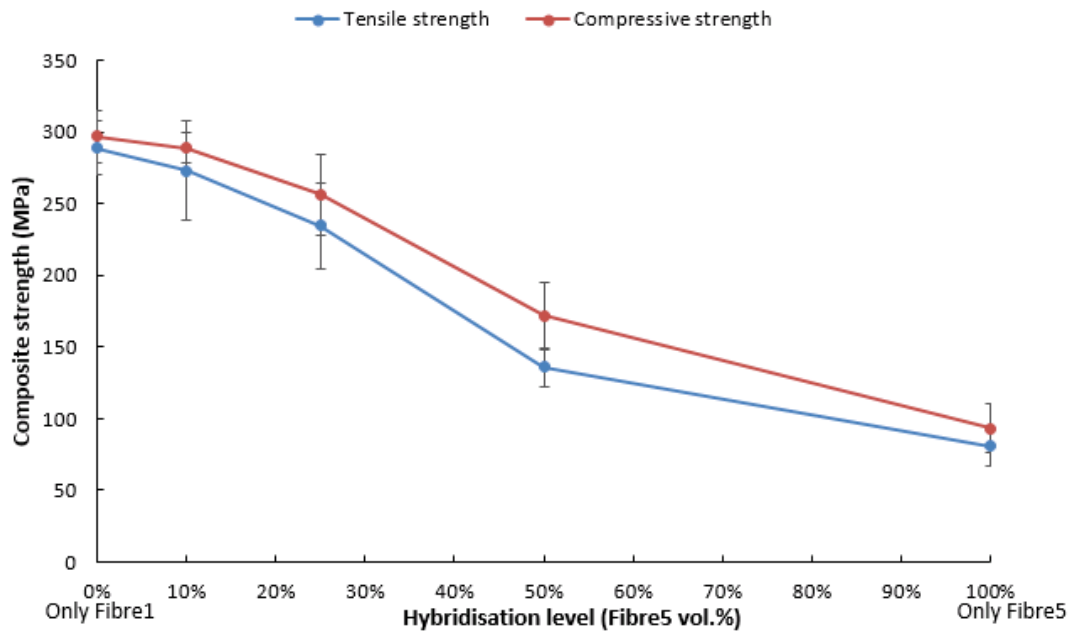


Figure 6.7 Ultimate strength of DCFP hybrid fibre plaques at various hybridisation levels

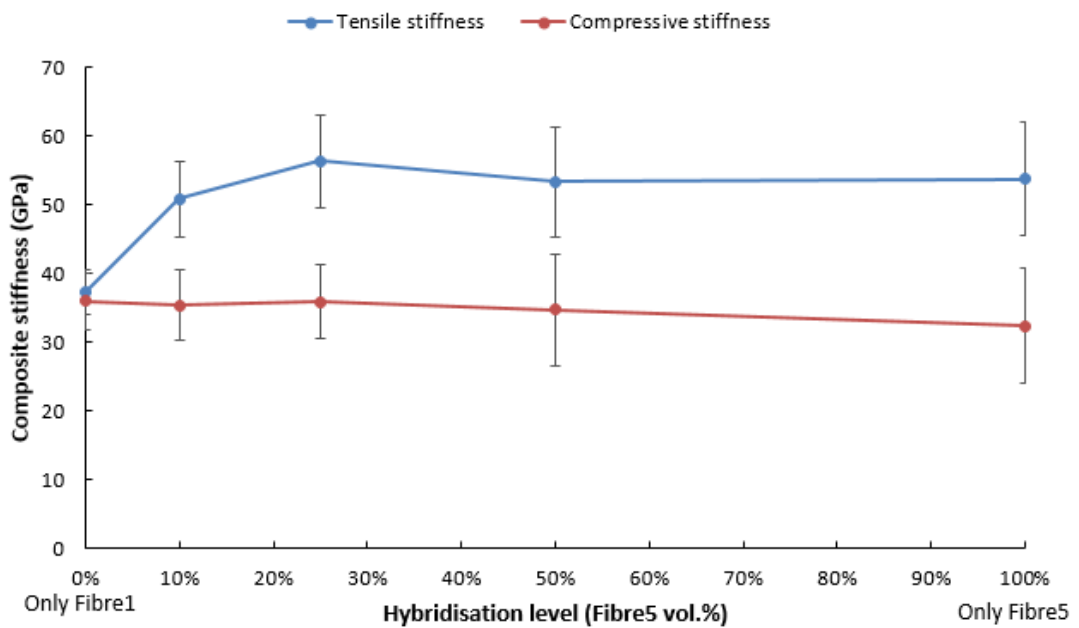


Figure 6.8 Composite stiffness of DCFP hybrid fibre plaques at various hybridisation levels

The key design objective for an automotive structure is stiffness, therefore an optimal combination of density, Young's modulus, and cost is required to make new material developments attractive. The 'cost per unit of function' needs to be favourable if composites are to replace metallics. The density of the plaques manufactured in the current study were all similar, since they all had the same target fibre volume fraction. The tensile stiffness and strength values have been normalised with respect to fibre cost to identify the most cost effective solution in each case, also taking into consideration the hybrid fibre options. The objective was to establish if it would be more cost effective to use a small volume of a high performance material with a high purchase cost, compared to using larger volumes of industrial grade fibres. The tensile stiffness data presented in Figure 6.6 and Figure 6.8 and the tensile strength data presented in Figure 4.10 and Figure 6.7 have been normalised with respect to the fibre costs presented in Table 6.1 and are presented in Figure 6.9.

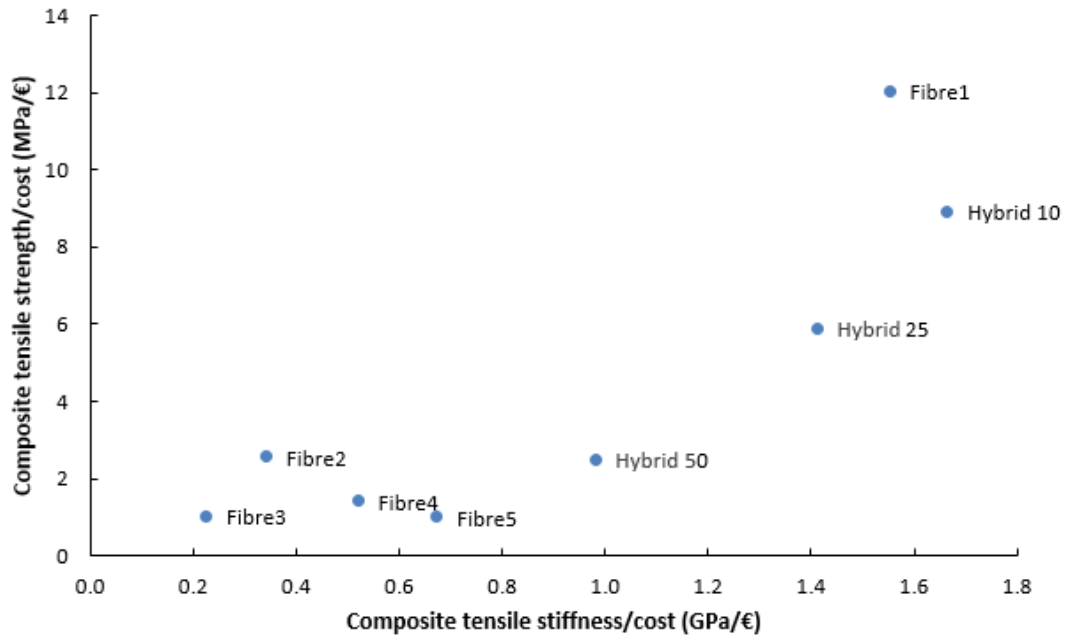


Figure 6.9 Tensile stiffness and strength values for moulded DCFP plaques normalised wrt. fibre cost

Fibre 3 is the least cost effective material in terms of the stiffness and strength values attained, whereas Fibre 1 is the most cost effective single fibre solution (12 MPa/€ and 1.55 GPa/€). The stiffness per cost and strength per cost of Fibres 2 to 5 are approximately 85% lower than Fibre 1. The hybrid plaques generally sit within the cost bounds of Fibre 1 and Fibre 5, since they are weighted averages. However, the stiffness per cost of Hybrid 10 is actually higher than Fibre 1, demonstrating the opportunity for increasing composite stiffness by adding a small quantity of high performance fibre (10% of Fibre 5) without having a detrimental effect of the component cost. It is important to remember however, that this trend may change if a higher performance resin system is used to effectively reduce the fibre / matrix stiffness ratio, as there is further potential to increase the efficiency factor of the fibres.

6.4 Effect of fibre selection on impact properties

Table 6.2 summarises the Charpy impact strengths for the RTM moulded DCFP parts. Both Fibre1 and Fibre2, which yield high tensile strength, also offer high impact strengths of approximately 108 kJ/m². However, the impact strength for Fibre4 DCFP plaque is just 36.2 kJ/m². Figure 6.10 shows the fracture sites for Fibre1, Fibre2, and Fibre4 DCFP parts after Charpy impact test. For specimens manufactured with high failure strain fibres (Fibre1 is 2.1% and Fibre2 is 1.9%), failure tends to be resin dominated therefore cracks tend to circumvent the fibre bundles (Figure 6.10 (a) and (b)), resulting in large failure zones. Hence, high levels of impact energy can be absorbed in this way. In contrast, the failure strain of Fibre 4 is 1.0%, therefore impact failure tends to be fibre dominated. This enables cracks to propagate quickly through the thickness of the specimen (Figure 6.10 (c)), yielding low impact strength. DCFP plaques using Fibre3 and Fibre5 also have low impact strengths of ~30 kJ/m². Failures are resin dominated, but the poor fibre distribution causes unreinforced resin rich regions, which unhinder crack propagation during impact, minimising the size of the damage zone.

In contrast, Hybrid10 DCFP offers an impact strength is 106.6 kJ/m², with a slightly lower tensile strength compared to Fibre1, but with significantly higher tensile stiffness (Figure 6.7 and Figure 6.8).

Table 6.2 Charpy impact strengths of RTM moulded DCFP parts (V_f 50%)

DCFP	Fibre1	Fibre2	Fibre3	Fibre4	Fibre5	Hybrid 10	Hybrid 25	Hybrid 50
Impact strength (kJ/m²)	108.9 ±8.8	108.0 ±6.7	30.3 ±5.7	36.2 ±3.1	26.4 ±2.7	106.6 ±10.4	96.4 ±25.0	78.5 ±23.8

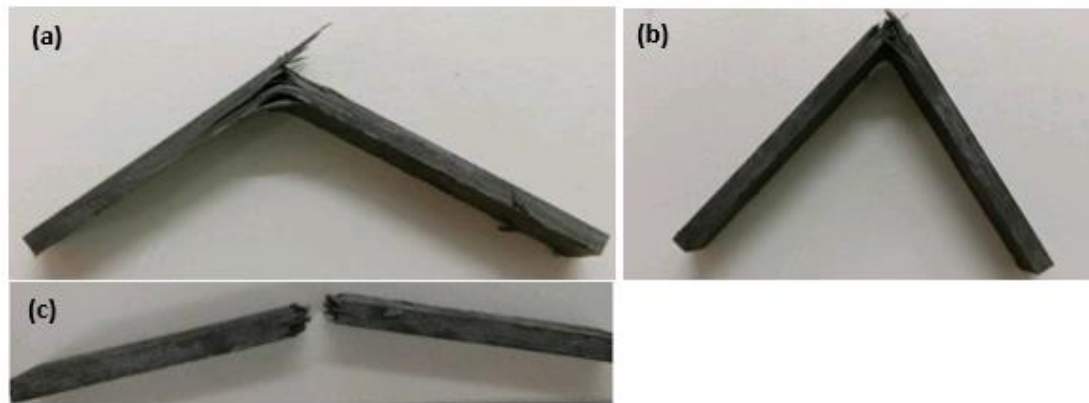


Figure 6.10 Fractures of RTM moulded DCFP parts after Charpy impact test: Fibre1 (a); Fibre2 (b); and Fibre4 (c) (Original specimen size: 80mm×10mm×2.7mm)

6.5 Overview of structural investigations of DCFP using high strength and high modulus carbon fibres

A series of discontinuous fibre plaques were manufactured with a range of different carbon fibres, with fibre strength values ranging from 3200 MPa to 5490 MPa and modulus values ranging from 230 GPa to 760 GPa. The ultimate strength of the DCFP plaques increases monotonically with increasing fibre strength, converging at 300 MPa for a fibre volume fraction of 50%. Higher strengths are difficult to achieve for the current fibre / matrix combinations due to the presence of resin rich region in DCFP component. Although the high stiffness/strength Fibre 2 offers an architecture with a higher homogeneity factor (12.2 tow/cm²) compared to Fibre 1, its void content (~1.0 %) was ~20% higher, which limited the tensile strength improvement.

The effect of increasing the fibre stiffness on the DCFP composite stiffness is less clear, with no obvious trend and experimental values far from the theoretical values predicted by an analytical equivalent inclusion model. The DCFP plaques manufactured from high-stiffness fibres (e.g. Fibre 3 and Fibre 5) have poor fibre distribution leading to large V_f variability (13%) in the moulded parts, so the stiffness values are less than half of the theoretical values due to the presence of many low V_f regions.

A hybrid DCFP plaque consisting of Fibre1/Fibre5 provides a useful compromise between mechanical properties and material cost. A plaque with 90% Fibre 1 and 10% Fibre 5 yields similar tensile strength (290 MPa) and impact strength (106 kJ/m²) to neat Fibre 1 DCFP plaques. However, its stiffness (50 GPa) is 31% higher, which makes it comparable to the stiffness of the more expensive Fibre 4 plaque, which also has a very low impact strength. The large amount of Fibre1 in Hybrid10 DCFP ensures the homogeneity factor is still high to avoid resin rich regions. When fibre cost is considered, the Hybrid 10 achieves the most cost effective component stiffness (1.6 GPa/€) and the second most cost effective strength (9 MPa/€) of all the fibre combinations tested.

Chapter 7 Impulse excitation measurement for rapid Young's modulus determination of DCFP components

7.1 Background

The Impulse Excitation Technique (IET) is a non-destructive testing method to determine material properties (e.g. Young's modulus and damping) through measuring resonant frequency. It has been applied to Young's modulus measurement for various materials, such as metals, ceramics, and composites, and provides an error of generally less than 1% against the data from tensile testing [119-122]. According to ASTM E1876-15, the Young's modulus of a specimen is expressed as follows:

$$E = 0.9465 \left(\frac{m f_f^2}{b} \right) (L^3 / t^3) T \quad \text{Equation 26}$$

where E is Young's modulus, m is mass, b is width, L is length, t is thickness, f_f is flexural resonant frequency, and T is correction factor, which can be simplified as $T = 1 + 6.585(L/t)^2$ (if $L/t > 20$).

IET has been applied to composite materials in the past, but these were generally metallic or ceramic matrices with particulate reinforcements that were relatively homogeneous. There is little literature about measuring the Young's modulus of fibre reinforced composites. Viens et al. [123] and Song et al [124] demonstrated that the error between IET measurements and tensile testing was less than 5% for laminated carbon fibre composites. However, it is uncertain whether IET is applicable to DCFP with random discontinuous fibres and a heterogeneous architecture. The objective of this chapter was to investigate if IET could be used to produce fast and simple

measurements to determine the Young's modulus of discontinuous fibre components.

7.2 Impulse excitation measurement setup

An RFDA Basic (manufactured by IMCE) was used to measure the modulus of RTM moulded DCFP specimens, which were the same specimens used for tensile testing, according to the ASTM E1876-15. However, impulse excitation measurements were taken before the tabs were bonded to the ends of the specimens prior to tensile testing. The testing rig (Figure 7.1) has three parts: a universal wire support, a USB-microphone (10Hz – 16kHz) connected to a PC, and a manual excitation unit (a small hammer). The measurement process was performed according to the following procedure:

- Place a 250mm-long DCFP specimen according to the position illustrated in Figure 7.1.
- Input the measurements of the specimen into the software: length/width/thickness/mass.
- Activate the microphone. Then use the excitation unit to hit the centre of the specimen.
- Record the modulus and damping data from the resonant frequency.

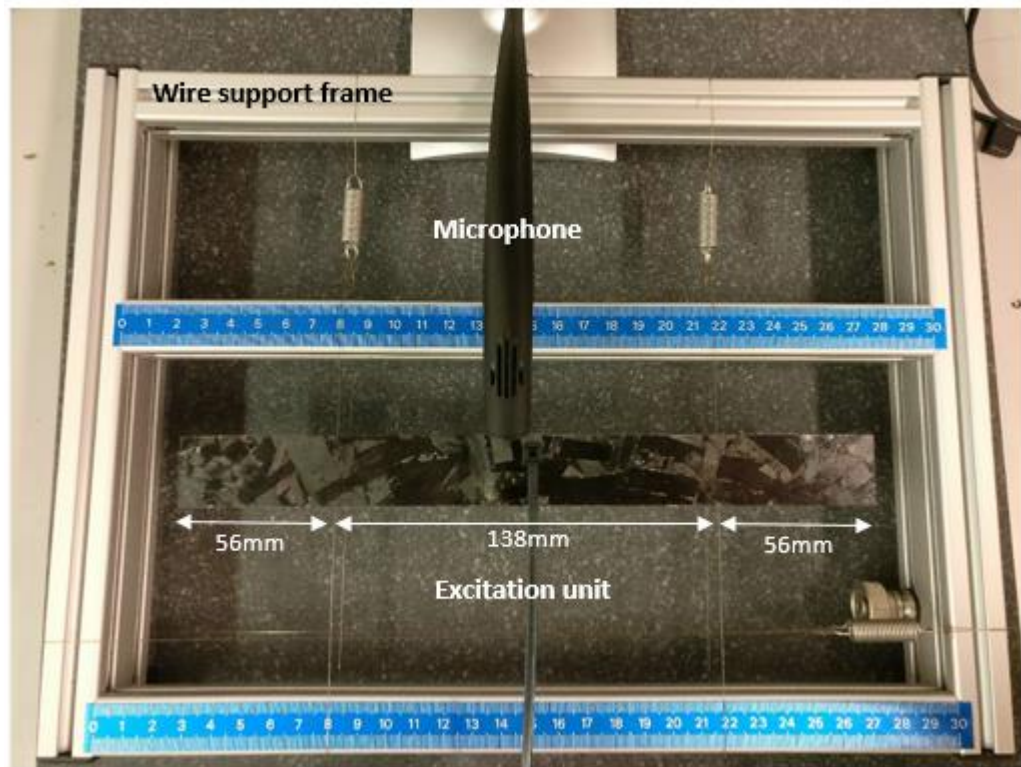


Figure 7.1 RFDA Basic testing rig

7.3 Comparison of modulus measurement between IET and tensile testing

Figure 7.2 compares DCFP stiffness values from tensile tests and the impulse excitation measurement. The stiffness achieved from the impulse excitation measurement is generally within 3% of the mechanical tensile test, especially for Fibre 1, Fibre 2, and Fibre 4 DCFP specimens which have high homogeneity factors ($> 6.8 \text{ tow/cm}^2$). The $< 3\%$ error is generally less than the intra-plaque stiffness variation ($\sim 5\%$). For the DCFP specimens manufactured from Fibres 3 and 5, there is over 20% difference in the stiffness values between the two measurement methods, since their architectures have low homogeneity levels. The presence of large resin rich regions (Figure 6.5) will influence the resonant frequency of the material under excitation by absorbing energy and inhibiting wave propagation. Hence, the recorded acoustic wave does not accurately represent the material tested, which leads to an erroneous

modulus value. Based on the experimental data in this work, the impulse excitation method offers accurate stiffness measurement for the DCFP specimens with high homogeneity level. Hence, potentially it could be applied in industry to provide a rapid stiffness measurement method and a convenient quality check tool to identify problematic DCFP components with poor fibre distribution.

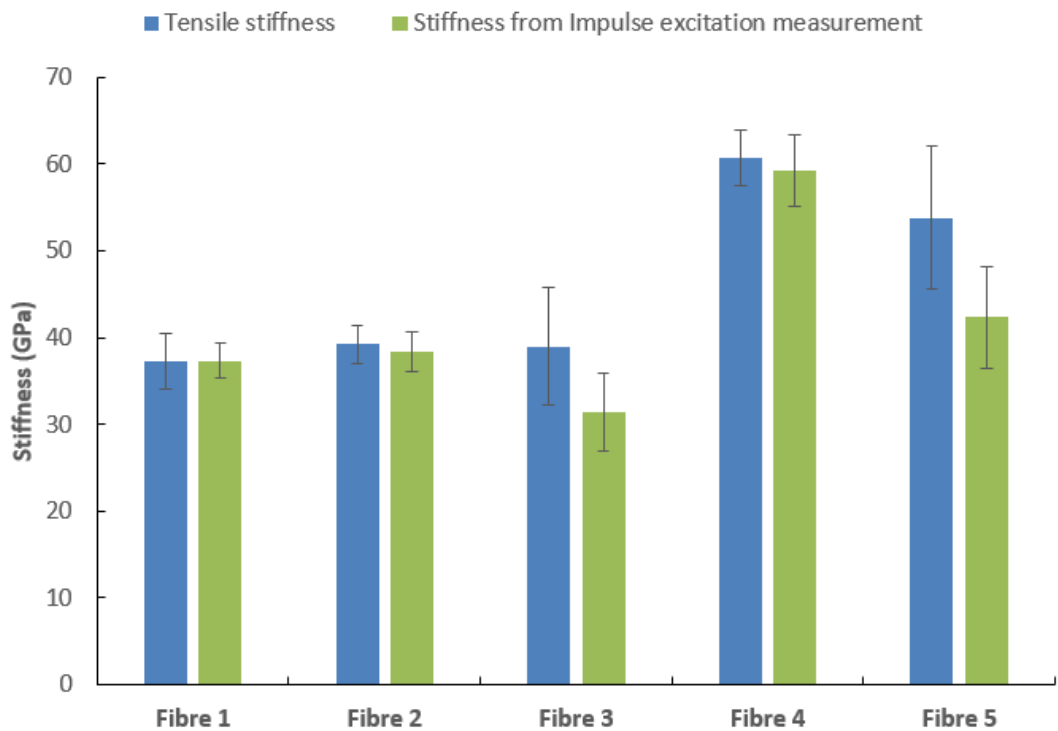


Figure 7.2 Stiffness values of DCFP parts from tensile test and impulse excitation measurement

Chapter 8 A water-soluble core material for manufacturing hollow composite sections

8.1 Introduction

This chapter investigates the potential for using water soluble salt (NaCl) cores, similar to the ones that are used to produce high pressure die castings [125], to produce hollow carbon fibre composites. The cores consist of NaCl and a water-soluble and environmentally friendly binder, trehalose sugar, which can be hot pressed into shape. They can be simply washed out after the composite moulding cycle using water and the NaCl content can be recovered through evaporation. A study is presented to define a processing window for the NaCl core to achieve suitable mechanical properties for use in high pressure moulding processes (100-150 bar), whilst ensuring the core can still be removed from the composite, post moulding. The influences of binder content, processing pressure, temperature and time are all investigated.

8.2 Background

Compared to foam cores, which normally remain within the final composite component after the moulding process, a removable core is able to provide more design flexibility to achieve the ultimate lightweight design for composites structures. Hollow inner cavities can be used to position wiring harnesses or other services, which can help improve packaging and increase space in the passenger cell. Removable cores can also be used to mould re-entrant geometries, which could not otherwise be moulded with rigid tooling. The following criteria has been identified to ensure the core material is suitable for high pressure composite moulding processes:

- Sufficient compressive strength (typically 15 MPa) at elevated mould temperatures (typically 120 °C)
- Impermeable to low viscosity resins
- Fully removable and within the Takt time of the moulding process (typically 5-30 minutes)
- Easily removable without inducing damage to the composite structure
- Machineable or castable to produce complex geometries
- Low cost
- Recyclable and environmentally friendly

Inorganic salts are an appropriate material choice for removable cores, as commercial salt cores are reported to have flexural strengths of over 18MPa [125] and have been used for high pressure die casting (HPDC) at temperatures and pressures exceeding 690°C [39] and 60MPa [126] respectively. Different compositions have been investigated in the literature, including KCl based cores for high bending strength at elevated temperatures [39, 127], NaCl cores containing mica powder for cost reduction [42], NaHCO₃ based cores for accelerating core removal [128], and four binary systems (NaCl-Na₂CO₃, KCl-K₂CO₃, KCl-NaCl and K₂CO₃-Na₂CO₃) for increasing mechanical properties compared with NaCl cores [126]. The material is readily available and inexpensive and can be dissolved in water to enable the core to be washed out from the composite structure. There is also the potential to recover some salt from the waste solution.

There are typically three binding mechanisms for salt cores. These include 1) mechanical deformation of grains by sintering, 2) melting followed by consolidation

and 3) adhesives (see Table 8.1). For sintering, salt particles are typically pressed at over 100MPa and then thermally treated at 650°C to increase the bending strength from 5 MPa to 9 MPa [39]. Whilst sintered cores have good mechanical properties and low porosity (reported as 2%-6% [39]), they are limited to producing simple geometries because a non-isostatic pressure is generated in the tool. The magnitude of the processing pressure is also an issue for larger scale components, due to the high capital costs for tooling and a hydraulic press. For the same reasons, casting liquid salt cores is not appropriate for large composite components. In addition, the energy consumption for producing cast liquid salt cores is high due to the melting point of salt (800 °C) and the shrinkage of the core can be significant (>15%.vol) following solidification [39, 126]. The dissolution rate is also very slow, requiring high pressure water jets (600 bar) to remove the core [129].

Table 8.1 Salt cores made by different processes and their mechanical property

Manufacturing process	Core material	Flexural strength (MPa)	Comments
Sintering	KCl NaCl	>9.0	Pressed at 104MPa; Additives: ZrSiO ₄ , Al ₂ O ₃ , SiO ₂ , Fe ₂ O ₃ ; Heat treatment at 650°C [39]
Binder	NaCl	2.1	Binder: water glass; Pressure: 7.5-8 bar [39]
	NaCl	6.6	Binder: polyethylene glycol and 10wt.% plasticizer; Pressure: 4-5 bar [42]
Liquid casting	NaCl	>18.0	[129]
	NaCl Na ₂ CO ₃	>30.0	NaCl-70mol% Na ₂ CO ₃ [126]

Using a binder to stabilise the salt core can effectively reduce the required consolidation pressure to less than 1 MPa [42], as a high level of mechanical interlocking of the salt grains is not required to achieve acceptable properties. The

mixture can also be pressed warm or cold, depending on the binder used [39, 42, 127, 128]. Binders used for salt cores are often sodium silicate (water glass), synthetic resins, and polyethylene glycol [39, 42, 127, 128]. Compared to sintered cores, more complex shapes can be produced but the porosity level is much higher (up to 30% [39]), and therefore mechanical properties are lower. Depending on the binder type, the addition of such a parasitic material can have a negative effect on the dissolution rate [39].

8.3 Water-soluble core development methodology

An extra fine NaCl powder with an average particle size of 0.59 mm was used to manufacture water-soluble cores, referred to here as NT Cores. Trehalose sugar was used as the binder material, which had a powder particle size of <0.30mm. Trehalose is a non-reducing sugar formed from two glucose units joined by a 1-1 alpha bond. It is therefore water-soluble and compatible with NaCl and does not appear to affect the fibre reinforced composite. Both powders were mechanically mixed to the required ratio and then poured into a preheated cylindrical mould with an inner diameter of 150mm. The mould surface was coated with Frekote 700-NC mould release to aid removal of the core. The salt/sugar mixture was hot compacted and held at temperature before the tool was cooled in the press at a rate of 5°C/min. The core was demoulded when the tool temperature had reduced to 30°C. Test coupons were machined from the round disc, typically 13mm thick, using a 3mm wide diamond tipped circular saw (see cutting plan in Figure 8.1). Before machining, the dimensions and mass of each core were recorded to calculate the density.

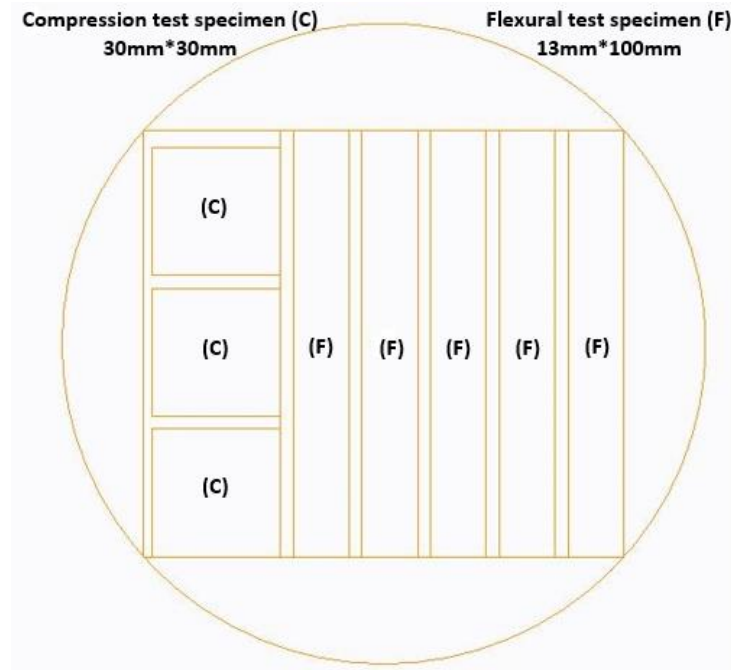


Figure 8.1 Cutting plan of test specimens from a circular disc, 150mm diameter, 13mm thick

8.3.1 Design of experiment

A Taguchi study was conducted to establish the relative significance of a range of processing variables on the strength of the NT Core at ambient temperature, and the dissolution behaviour in water. The independent variables and their associated levels are summarised in Table 8.2. Processing pressure directly influences the cost of the tooling and capital expenditure and therefore should be minimised to produce cost effective cores for high volume applications. The effect of binder content, processing temperature and processing time were all investigated as possible ways to compensate for lower processing pressures.

With a broad “processing window” defined, a more detailed second study was conducted to determine the effect of elevated in-service mould temperatures, with tests conducted at 80°C and 120°C. Two widely-used core materials were also tested

as benchmarks: a structural closed cell foam (A Core) and a water-soluble material containing ceramic microspheres (B Core). The B Core material was moulded in the same circular tool as the NT Cores at a pressure of 17bar at room temperature. The demoulded cores were subsequently dried in an oven at 125°C for 1.5 hours.

Table 8.2 Parameters and associated levels in the Taguchi study

Parameters	Levels		
Binder content (wt.%)	3	5	8
Processing pressure (bar)	55	85	170
Processing temperature (°C)	120	150	190
Processing time (min)	10	30	60

8.3.2 Experimental methods

8.3.2.1 Mechanical testing of core

Both 3-point bend and compression tests were conducted on an INSTRON 5985 universal testing machine. For 3-point bending tests, five 13 × 13 × 100 mm specimens were prepared for each material and a constant span of 60 mm was used between Ø10 mm support rollers for all specimens. Tests were performed at a speed of 1 mm/min. The applied force was recorded by a 25 kN load cell and the central deflection of the specimen was recorded by an LVDT positioned on the underside of the specimen. Three compression test specimens were prepared for each material configuration, which were cut to 30 × 30 × 13 mm and compressed between Ø50 mm platens at a speed of 1 mm/min. A 100 kN load cell was used to record the applied compressive force.

8.3.2.2 Microscopy

The cross-sections of the core materials were observed by optical micrographs at 5x magnification. The specimens were cut from the ends of the flexural test specimens after the bending test was finished, and machined into 13 × 13 × 13 mm cubes. The faces of interest were polished unmounted, using silicon carbide paper (P240, P400, P800, P1200, P2500, and P4000) but without using any fluids.

8.3.2.3 Thermoanalytical testing

Coefficient of thermal expansion (CTE) measurements were conducted on a Q400 TMA from TA Instruments. CTE measurements were performed on the microscopy specimens, across the temperature range from 20°C to 120°C at a rate of 5°C/min.

Differential scanning calorimetry (DSC) was conducted for the trehalose binder on a Q100, supplied by TA Instruments. For the as-received trehalose powders, a full profile scan was performed at a rate of 5°C/min from 20°C to 230°C. To represent the core manufacturing conditions, the trehalose was heated at 5°C/min from 20°C to 150°C and held at 150°C for 1 hour, before being cooled to 20°C. Subsequently, the same sample was reheated up to 150°C at the same ramp rate to identify whether the trehalose had experienced a phase change after the core had been made.

8.3.2.4 Core dissolution rate measurements

An ultrasonic water bath (Sonic 3000 from James Products Ltd) and a conductivity meter (HANNA HI8733) were used to measure the dissolution rate of the core. A calibration line was created by measuring the conductivity of known quantities of NaCl in one litre of distilled water at 25 °C. NT Core specimens of 13 × 13 × 20 mm

were used for the dissolution rate measurements. Each specimen was weighed and then positioned in the middle of the water bath inside a wire basket. The conductivity of the water was recorded from the point at which the specimen was placed in the water until it reached a constant value (indicating that the sample had fully dissolved). The change in conductivity was converted into the change of NaCl concentration using the reference line. The dissolution rate of the core material, d_n (g/min), was calculated using the gradient of the concentration change curve. The specific dissolution rate, d_s (g/(min·m²)), was calculated by:

$$d_s = \frac{d_n}{A} = \frac{\Delta C \cdot V}{A \cdot \Delta t} (1 + \epsilon) \quad \text{Equation 27}$$

where Δt is the time period, ΔC is the concentration change during time period Δt , V is the volume of water, ϵ is the binder content of each sample, and A is the total surface area of each specimen.

8.3.2.5 Core removal trials

Water jet removal trials were conducted for a B Core sample and an NT Core sample (same composition as used for the machining trials). Both core materials were machined into trapezoidal columns, shown in Figure 8.2 (a). To ensure a direct comparison, all cores were coated with 3 layers of Aquaseal 3818 coating (made by Advanced Ceramics Manufacturing). Each layer of Aquaseal was sprayed on the core, which was then allowed to dry in an oven at 40°C for 30min before the next layer was applied. Cores were then wrapped with two plies of MTM 49 – 3/CF1218 twill weave T800 carbon fibre prepreg from Cytac, keeping one end open to facilitate the removal

of the core (Figure 8.2 (b)). This whole arrangement was placed on a metallic plate, vacuum bagged and put into an autoclave at 100°C and 6 bar for 4 hours to cure.

The cured samples were removed from the autoclave and clamped into a fixture to maintain a constant 10mm distance between the open end of the sample and the water jet (Figure 8.2 (c)). The nozzle had an elliptical orifice (the lengths of the semi-major and semi-minor axes were 1mm and 0.75mm respectively) and a 25° spray angle. A water temperature of 40°C and a pressure of 8 bar were used for all tests. Each test was stopped after 10 second intervals to record the amount of core removed. The residual water in the hole was poured into a measuring cylinder to record the volume, to indicate the volume change of the core.

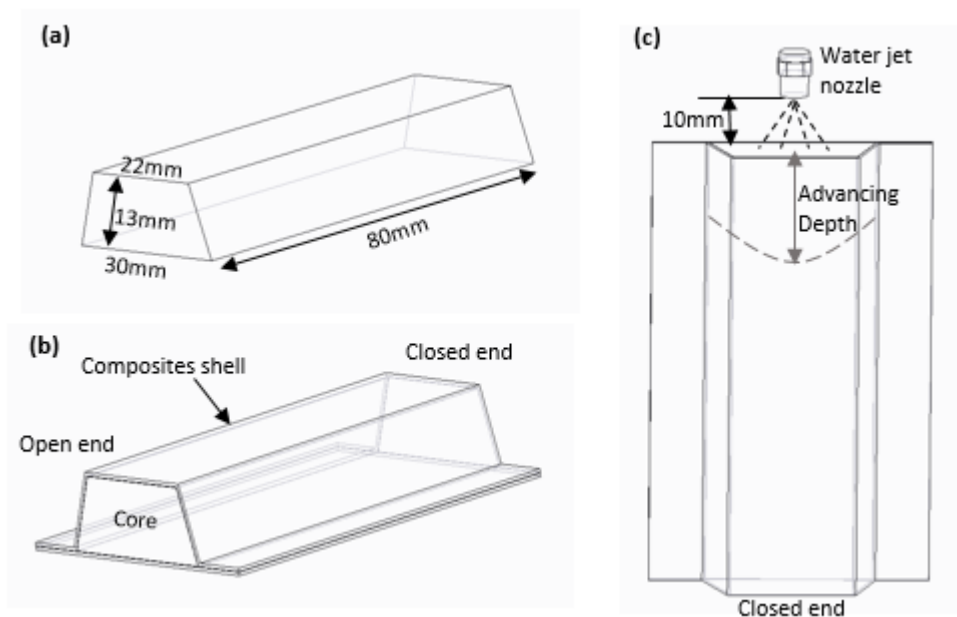


Figure 8.2 Schematics of core dimensions (a), core wrapped with composites shell (b), and positions of water jet nozzle and wrapped core (c) in water removal trial

8.3.2.6 Core machining trials

Machining trials were performed to observe the effects of cutter type on the quality of the machined surface. A 4-flute ball nose cutter and a 4-flute flat end mill, both with a diameter of 10mm, were selected to make slots in core specimens. A spindle speed of 1400rpm was used with a feed speed of 200mm/min to produce a 1mm deep cut. Five consecutive cuts were completed to produce a 5mm deep slot. Surface roughness profiles were measured at different locations along the slots using a Talysurf CLI 1000 mounted with an inductive gauge. Figure 8.3 indicates the locations of the measurements along the two different shaped slots.

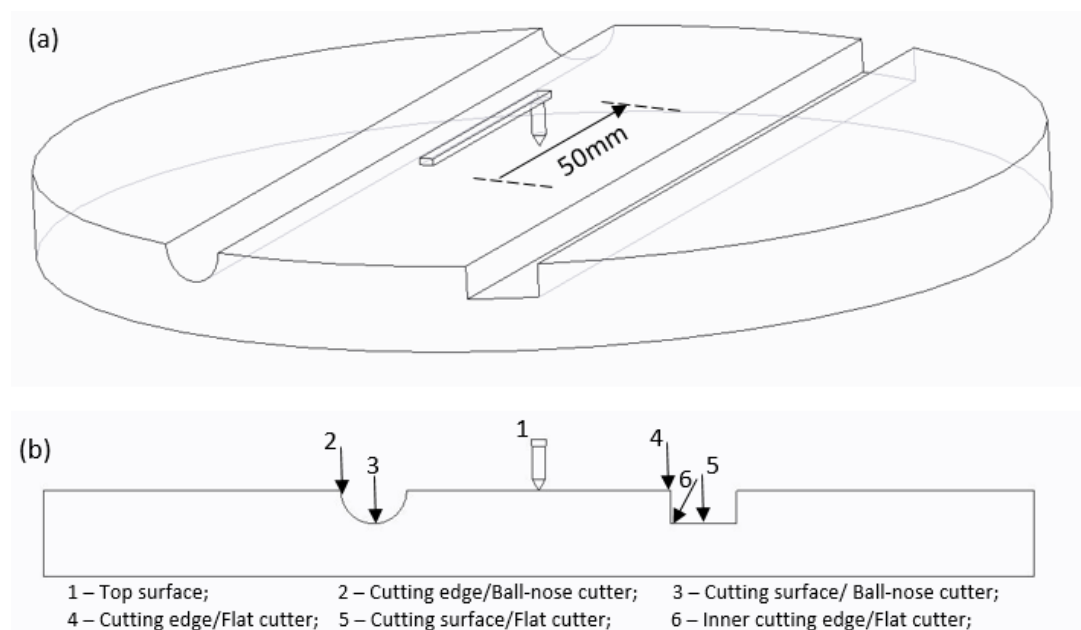


Figure 8.3 Schematics of two types of cutting slots, scanning direction and range of 50mm (a); 6 locations where the inductive gauge places (b) on a round sample disc with 150mm diameter

8.4 Core strength at ambient

Compression and three point bend tests were conducted on a range of cores manufactured with different binder content levels, processing pressures, processing

temperatures and tool times. Both the compressive and flexural strengths of the NT Core follow similar trends as the four main parameters are increased, as shown in Table 8.3. The most significant variable affecting both strengths was the applied pressure during the compaction process. The average compressive strength was 17 MPa for all samples moulded at a pressure of 55 bar. An increase in moulding pressure from 55 bar to 85 bar increased the compressive strength on average, by 19%. A further increase in moulding pressure to 170 bar increased the compressive strength by 144% over the average value observed at 55 bar. Increasing the processing pressure reduces the free space between the powder particles, strengthening the mechanical interlocking of the angular salt grains.

Table 8.3 All experimental results in Taguchi study showing the mean effects of four independent variables (pressure, temperature, time and binder content) on four dependent variables (compressive strength, flexural strength, density and SDR)

Mean	Processing pressure (bar)			Binder content (wt.%)			Processing temperature (°C)			Processing time (min)		
	55	85	170	3	5	8	120	150	190	10	30	60
Density (g/cm ³)	1.48	1.54	1.77	1.59	1.60	1.61	1.55	1.61	1.64	1.56	1.60	1.64
Change ratio	-	4%	20%	-	0.6 %	1.2 %	-	4%	6%	-	3%	5%
Comp strength (MPa)	16.9 2	20.1 6	41.2 2	22.7 8	26.4 2	29.1 0	23.3 7	26.1 9	28.7 4	23.9 9	25.7 2	28.6 0
Change ratio	-	19%	144 %	-	16%	28%	-	17%	28%	-	7%	19%
Flexural strength (MPa)	3.92	4.96	7.92	4.74	5.75	6.30	5.20	5.81	6.34	4.62	5.58	6.48
Change ratio	-	27%	102 %	-	21%	33%	-	10%	22%	-	18%	37%
SDR (kg/(min.m ²))	0.71	0.63	0.42	0.64	0.62	0.50	0.84	0.58	0.34	0.80	0.61	0.35
Change ratio	-	- 11%	- 41%	-	-3%	- 22%	-	- 31%	- 60%	-	- 24%	- 56%

Adding binder significantly improves the mechanical performance of these core materials, as the binder provides some adhesion. Dispersion of the binder improves

as the binder content increases, increasing the number of salt to binder contact points. The average compressive strength increased by 16% as the binder content was increased from 3wt% to 5wt%, and by 28% as the binder content increased to 8wt%. A similar increase in flexural strength was observed with increasing binder content. Figure 8.4 shows compressive and flexural stress/strain curves for cores with different binder levels. The shape of the compression curves are similar for increasing binder content, but the shape of the flexural curves changes as the core becomes more brittle (lower tensile properties compared to compressive properties) with increasing binder levels (when processed at 190°C). This demonstrates that the binder content influences the failure mode. Mechanical inter-locking of the salt particles is responsible for binding the core together at low trehalose levels. The salt particles can slip relative to each other when a load is applied, exhibiting plastic-like behaviour. The strain to failure decreases as the trehalose content increases and a linear stress/strain curve is observed for an 8wt% loading, as the failure of the core is due to binder fracture.

The failure mode also changes as the core is processed at different temperatures, as the binder goes through different phases. Figure 8.4 (b) shows that cores manufactured at over 150°C exhibit brittle behaviour in bending, compared to a more ductile failure mode when processed at lower temperatures. According to Table 8.3, the mechanical properties of the cores were improved with increasing processing temperature and time, since different phases of the binder were formed and the level of phase transformation was higher, as evidenced by the changes in colour of the samples. Phase characterisation of the trehalose is discussed in detail in the following section.

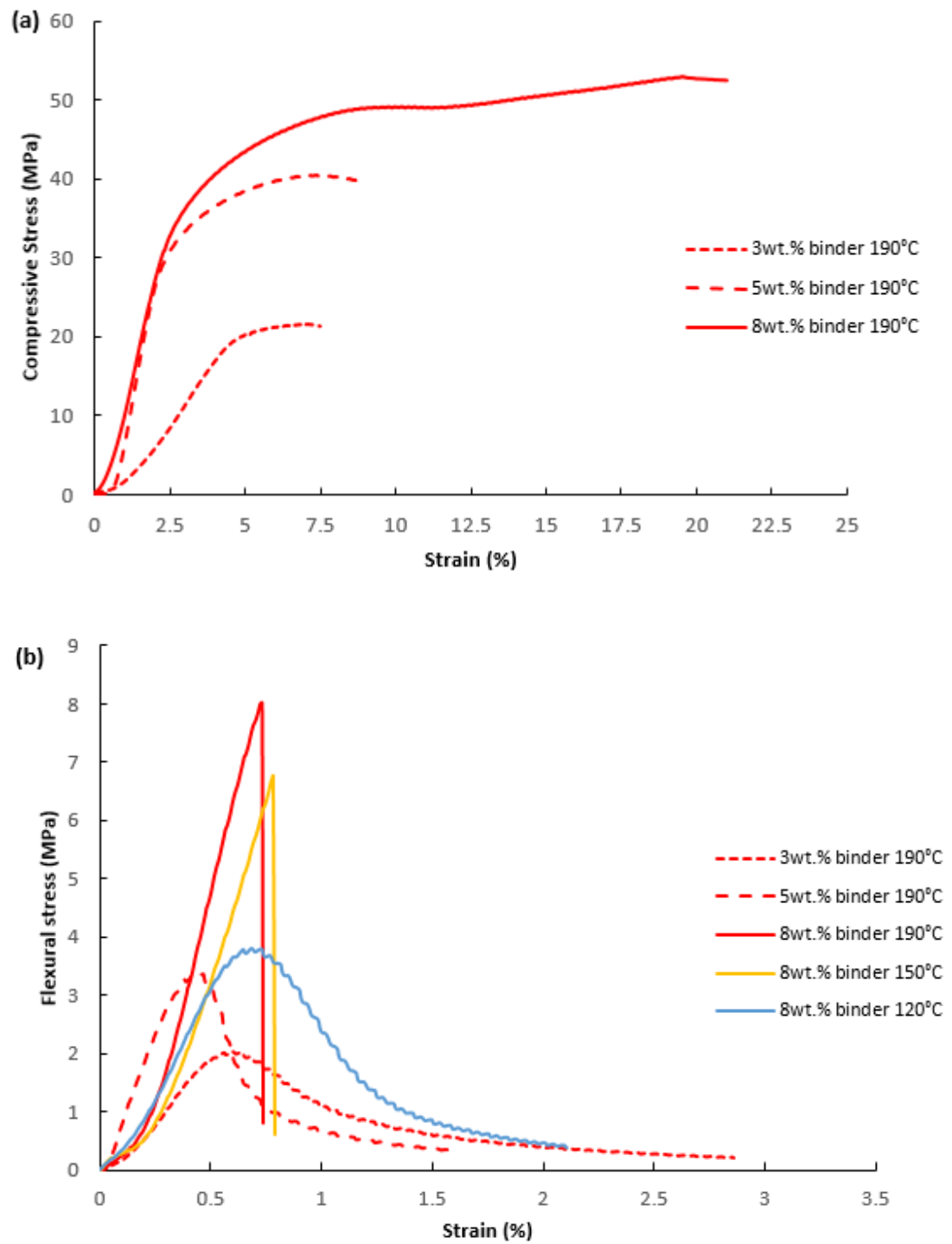


Figure 8.4 Compressive (a) and flexural (b) stress/strain curves for NT Cores with different binder levels and processing temperatures (manufactured at 170bar for 10min)

8.5 Phase characterisation of trehalose

Figure 8.5 shows a DSC curve for the trehalose binder, indicating heat flow in the temperature range of 20°C – 230°C, which is consistent with data in the literature [130, 131]. Two endothermic peaks were observed in the thermal profile at 100°C and 125°C, and a twin-peak was found at 185°C - 210°C. All peaks were labelled according to Sussich et al. [131]. Trehalose has three crystalline forms during the core moulding cycle, as the ramp rate is over 5°C/min: T_h (as-received, dihydrate), T_γ (metastable anhydrate) and T_β (stable anhydrate). This is in agreement with Sussich et al. [131], who reported the formation of a stable anhydrate (T_β) during the amorphous state between 150°C – 180°C when a fast heating rate was used (>10°C/min). This phase transformation explains the observed change in bending behaviour of the cores (shown in Figure 8.4 (b)), as a more brittle failure occurs as the processing temperature increases from 120°C to 150°C. Figure 8.6 demonstrates that there are no further phase changes when the core is reheated to 150°C, which implies that the binder is stable during the composite moulding process. This is because the trehalose becomes amorphous or a stable anhydrate at 150°C (see Figure 8.5) and any water is fully removed during the 1 hour processing time. According to Furuki et al. [132], these two phases are both stable in a dry environment. Based on the mechanical test results, the stiffness of the cores is significantly improved when the trehalose is processed at >150°C, indicating that the amorphous and stable anhydrate states have a positive effect on the mechanical properties.

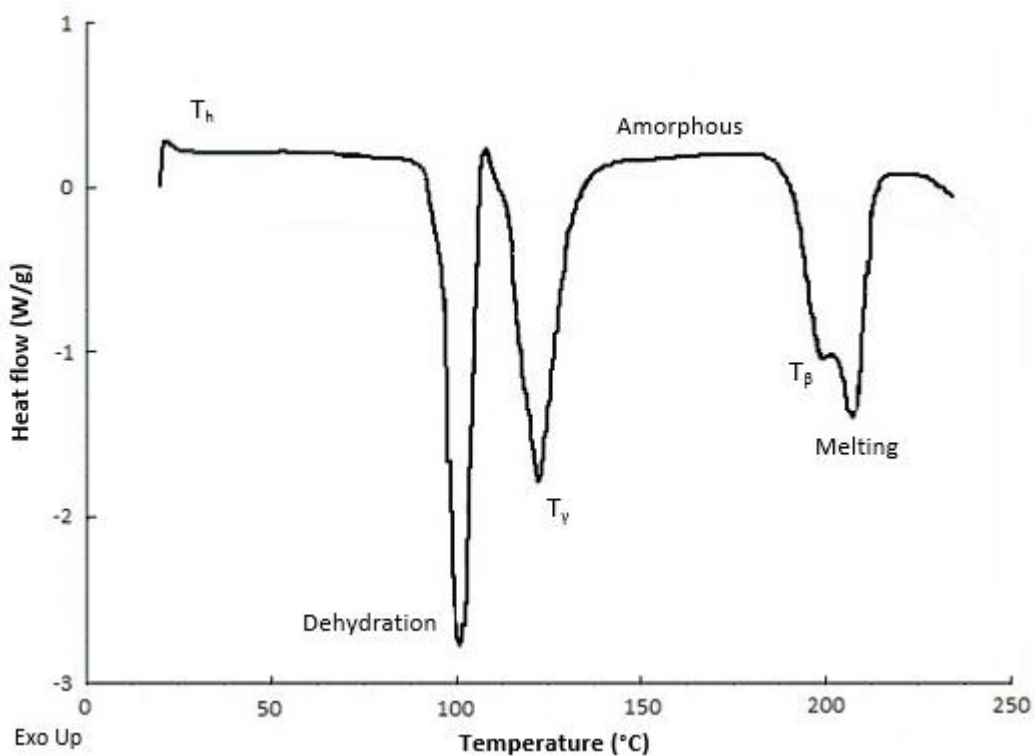


Figure 8.5 DSC profile of trehalose from 20°C – 230°C (heating rate 5°C/min)

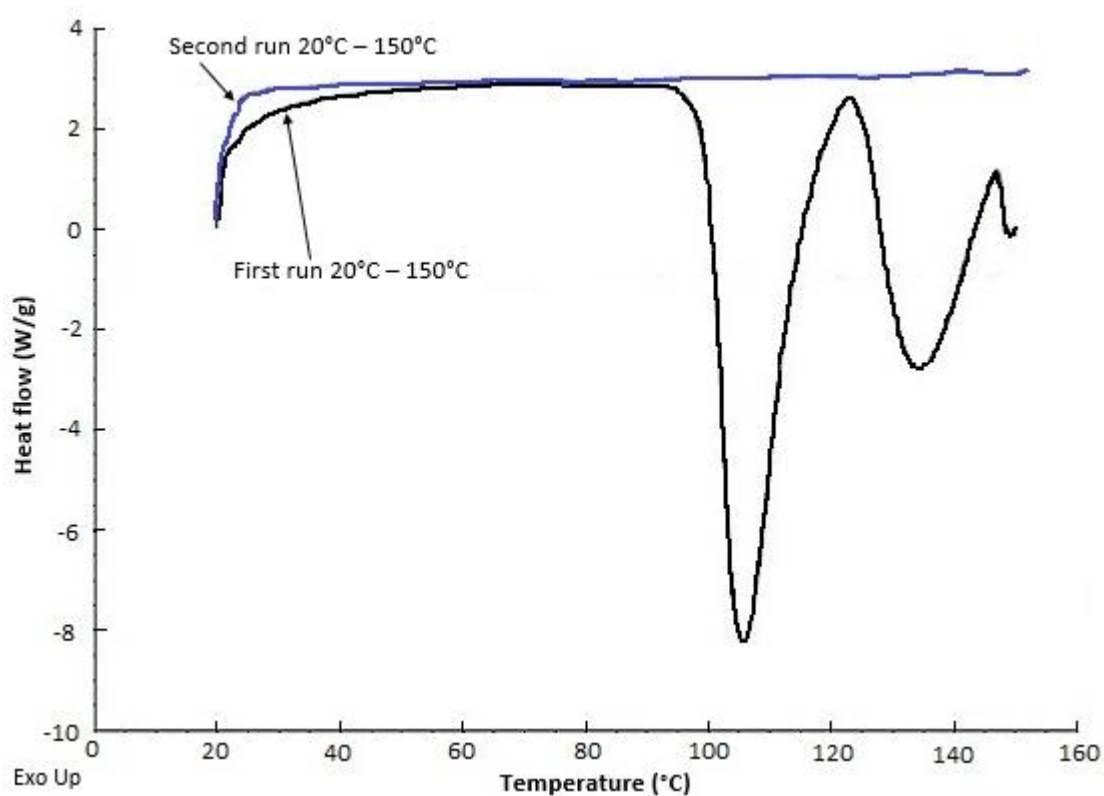


Figure 8.6 DSC profiles of trehalose from two heating process in succession within 20°C-150°C

Taylor et al. [130] and Sussich et al. [131] observed a state change for the dihydrate trehalose during heating. The trehalose is a solid when the applied temperature is below 120°C, but it starts to become tacky as the temperature exceeds 140°C and dehydration occurs. The trehalose turns to a fully liquid state at approximately 200°C. Figure 8.7 shows the distribution and morphology of the trehalose binder relative to the salt for an 8wt% loading, processed at two different temperature levels. The binder remains in a granular state at low processing temperatures and porosity is clearly visible. Conversely, at higher processing temperatures the softened binder migrates into the voids between the salt particles, which results in a reduction in porosity. Furthermore, this explains why the mechanical performance improves when processing temperature increases.

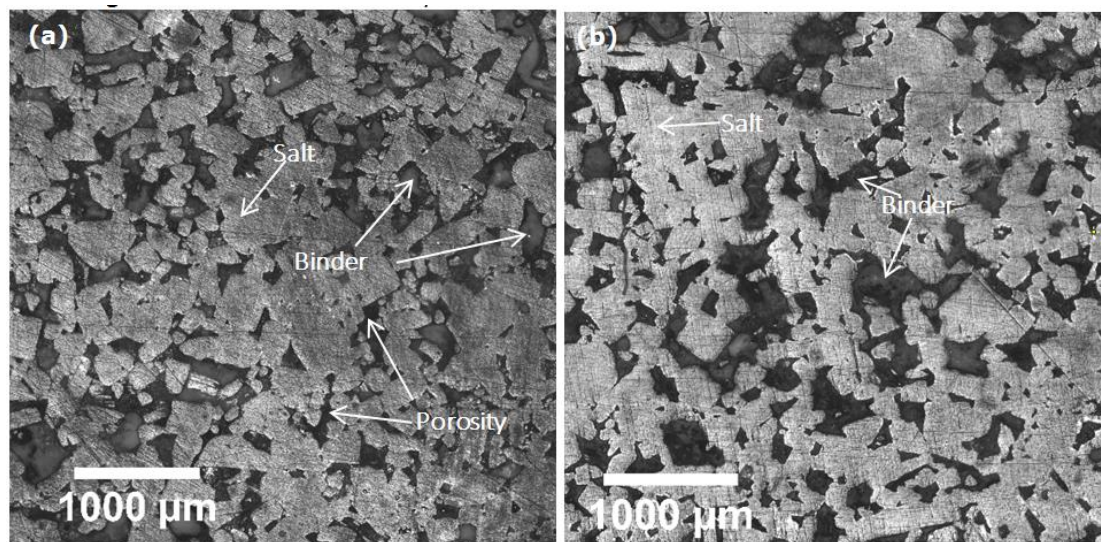


Figure 8.7 Optical microscope images of cross sections of the NT Cores having 8wt% binder content and processed under 170bar at (a) 120°C for 10min (porosity:16%) and (b) 190°C for 10min (porosity: 10%)

8.6 Core density

The density of the NT Core follows a similar trend to the mechanical properties, as the four independent variables are increased (Table 8.3). The density of the core is also dominated by the applied pressure during processing, which increases the mechanical inter-locking and reduces the free-space between the salt particles. The density of the core increases by 20% as the pressure is increased from 55 bar to 170 bar. Reducing the void content reduces the likelihood of undesirable resin penetration into the core during the composite moulding process, reducing the amount of residual material left within the composite part. Resin wicking into the core also increases the risk of dry spots forming in the composite laminate if a pre-impregnated fibre system is used, as the reinforcing fibres become starved of resin. Density calculations indicate that the average residual porosity of NT Cores pressed at temperatures higher than 150°C and pressures below 170 bar is approximately 10%, which is likely to be interconnected at this level. The target porosity level for avoiding resin infiltration into the core is 7% according to German [133]. It may therefore be difficult to avoid resin penetration without a large increase in core processing pressure or binder content, and consequently it may be necessary to coat the soluble core with an impervious layer prior to use. Increasing the binder content from 3wt.% to 8wt.% has a limited effect on the density of the core, which increases by only 1.2%. This is because of the relative densities of these two materials (2.16 g/cm³ compared to 1.58 g/cm³).

8.7 CTE measurement

Thermal expansion of the NT Cores is linear within the range of 20°C - 120°C, with CTE values reported to be $42 - 44 \times 10^{-6}/\text{K}$. According to Rao et al. [134], the CTE of pure NaCl increases from 39.80×10^{-6} to $42.90 \times 10^{-6}/\text{K}$ over the same temperature range, which indicates that the CTE of the cores is dominated by the NaCl rather than the trehalose binder. Therefore, the four independent variables (pressure, temperature, time and binder content) do not significantly affect the CTE of the core. The CTE range for the NT Core is close to that of commercially available sandwich panel cores [135]. High levels of thermal expansion are beneficial for generating in-mould pressures to improve the consolidation of closed sections.

8.8 Specific dissolution rate (SDR) measurement

The degree of dissolution as a function of time has been plotted for each NT Core sample, based on the conductivity change, as shown in Figure 8.8. It can be seen that the dissolution rate is approximately linear between 1-5min, which equates to approximately 50% dissolution for most samples. The gradient of the line within this time range can be used to calculate the specific dissolution rate (SDR) using Equation 26.

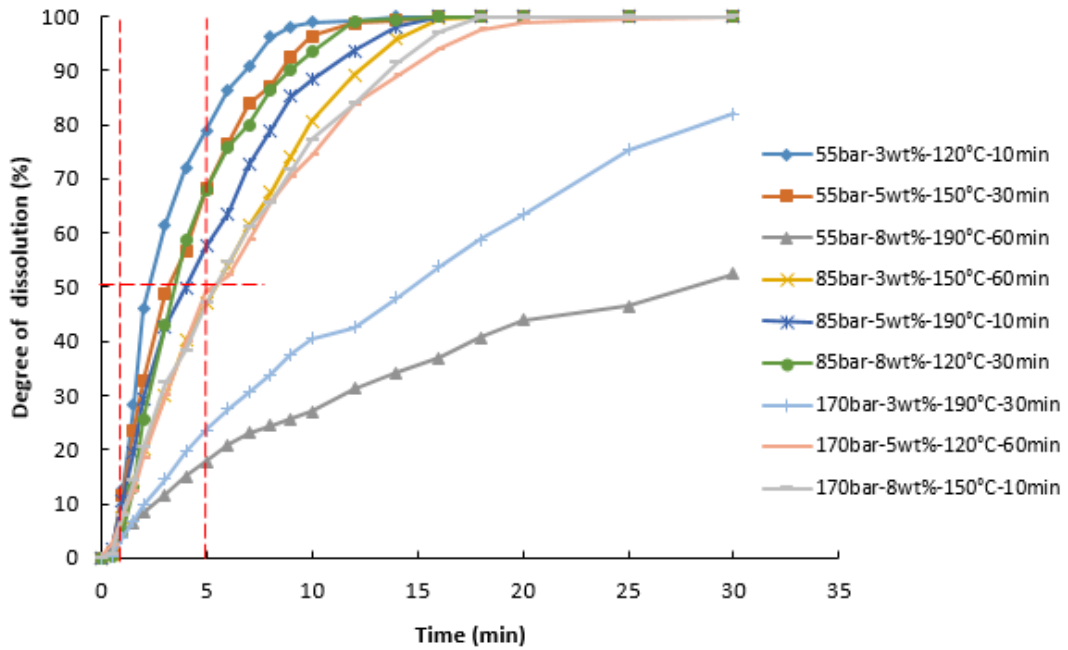


Figure 8.8 Degree of dissolution for NT Core samples in the Taguchi study (legend shows: processing pressure-binder content-processing temperature-processing time)

From both Figure 8.8 and Table 8.3, it can be seen that the SDR of the NT Core decreases with increasing levels of all four of the main parameters listed in Table 8.2. All SDR values are in the range of 0.14 – 1.23 kg/(min·m²). The SDR of the core which attained a flexural strength of 10.0 MPa ((170bar and at 150°C for 30min, 8wt.% binder) is 0.25 kg/(min·m²), which is ~5 times faster than the SDRs of the NaCl/mica/polyethylene glycol core developed by Jiang et al. [42], which had a flexural strength of just 4.1MPa. It is also ~140 times faster than the NaCl/mica/polyethylene glycol core with 10wt.% plasticiser, which exhibited a flexural strength of 6.6 MPa [42]. Increasing the processing pressure and binder content both increase the density of the NT Core, causing a reduction in the interconnected porosity and therefore reducing the SDR. Processing temperature is the most significant variable in terms of changes to SDR, closely followed by

processing time. The SDR of the core decreased by 60% when the temperature increased from 120°C to 190°C and 56% when the processing time increased from 10min to 60min. Increasing either processing temperature or time can lead to an increase in the density of the core as discussed above, which reduces the dissolution rate in water.

8.9 Elevated temperature testing

The main observations from the Taguchi study have been used to design a full-factorial study to understand the influence of in-service temperatures on the flexural and compressive strengths of the NT Cores. A processing pressure of 170 bar and binder content of 8wt% were selected, based on the discussion above. Figure 8.9 and Figure 8.10 show the compressive and flexural strengths of the NT Cores made using various processing temperatures and times, tested at 20°C, 80°C and 120°C. The ultimate strengths were highest when the cores were tested at ambient temperature; 57.3 MPa for the compressive strength and 10.2 MPa for the flexural strength. This flexural strength value is ~2.5 times higher than the value presented by Jelinek et al. [39] for a NaCl-based core pressed at 104 MPa, which is ~6 times higher than the pressure used in this work (17MPa). Mica powder is commonly used as a reinforcement for NaCl [136] and was used by Jiang et al. [42] to increase the strength of salt cores. However, the flexural strength was limited to just 6.7 MPa, 35% lower than the current NT Core system.

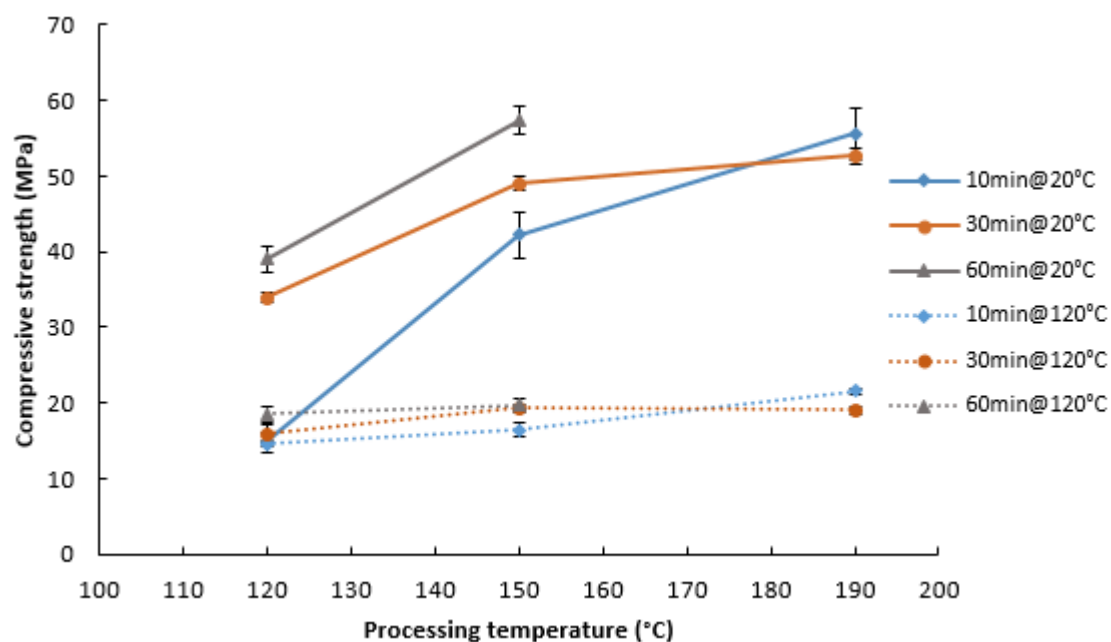


Figure 8.9 Compressive strengths of NT Cores manufactured using different temperatures and times (different line colours) and tested at 20°C (solid line) and 120°C (dotted line)

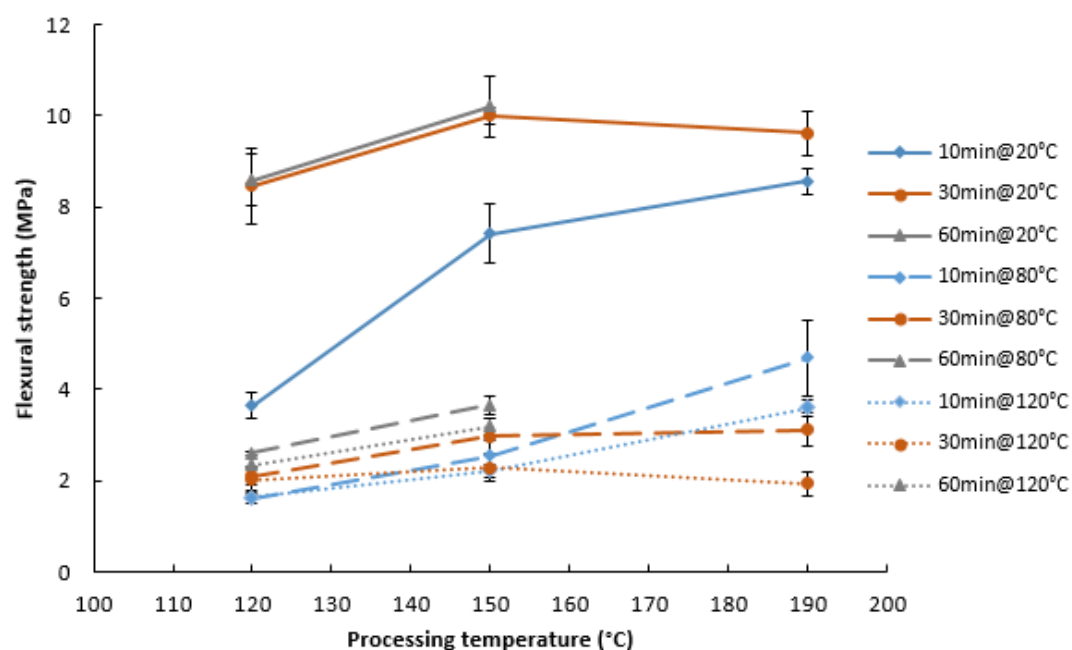


Figure 8.10 Flexural strengths of NT Cores made at various temperatures and times (different line colours) and tested at 20°C (solid line), 80°C (dashed line) and 120°C (dotted line)

The general trends for the ambient temperature data in Figure 8.9 and Figure 8.10 are consistent with the data presented in the Taguchi study in Table 8.3. Both the flexural and compressive strengths increase with increasing processing temperature. However, there is a dramatic reduction in both the flexural and compressive strengths as the test temperature increases to 120°C. (The reduction between 80 °C and 120 °C is less significant). The peak compressive strength is reduced from 57.3 MPa to 19.7 MPa and the peak flexural strength is reduced from 10.2 MPa to 3.7 MPa. Whilst there is a significant drop in mechanical performance at this temperature, the compressive properties of the core (15-20 MPa) are still sufficient for the application in HP-RTM and compression moulding.

The ultimate strengths are shown to increase between processing temperatures of 120 °C and 150 °C, even when tested at elevated temperatures. However, there is a reduction in properties as the processing temperature increases further to 190 °C and the processing time increases to 30 minutes. The flexural strength of the sample manufactured using a processing temperature of 190 °C for 30 minutes, and tested at 120 °C, is lower than the same sample processed at just 120 °C. This can be attributed to decomposition of the binder at elevated temperatures, particularly when the test temperature is close to the melting temperature of trehalose and longer processing times are used. At 190°C the trehalose sugar starts to 'caramelize', i.e. the fructose and glucose in the sugar decompose, which can be seen by the change in colour of the core specimens in Figure 8.11. The coupon manufactured at 190°C for 60min was unable to be tested, due to cracks caused by solidification shrinkage. The surface of this specimen was also tacky from the heavily caramelised binder.

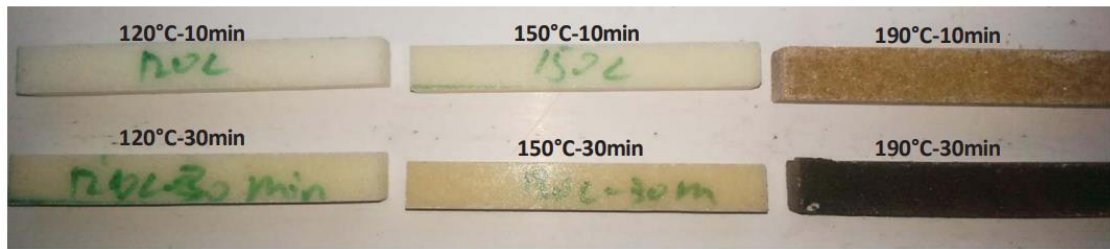


Figure 8.11 Different colours of NT Cores made at various temperatures for different time

From all of the mechanical test data available, it can be concluded that 150°C is an optimal processing temperature for the current study. The trehalose binder is amorphous at this temperature, producing a dense core body with high mechanical properties that can resist resin penetration. However, in order to achieve further improvements in mechanical properties for cores manufactured at 150°C, the processing time could be extended to 1 hour without causing property degradation.

Table 8.4 compares the strengths of the NT Core (processing pressure 170bar, binder content 8wt%, processing temperature 150°C, and processing time 60min) and two commercial core materials at both 20°C and 120°C. Although the strengths of all materials drop at elevated temperatures, the NT Core has higher flexural and compressive properties compared to both benchmark materials, making it a potential alternative for industrial applications.

Table 8.4 Comparison of strengths of the NaCl based core (NT) and other widely-used core materials

	Test temperatures	NT Core	A Core	B Core
Compressive strength (MPa)	20°C	57.3±1.8	1.6±0.1	5.1±0.2
	120°C	19.7±0.9	0.6±0.1	4.6±0.3
Flexural strength (MPa)	20°C	10.2±0.6	2.8±0.1	4.8±0.3
	120°C	3.2±0.2	1.4±0.1	3.6±0.3

8.10 Post moulding operations

The geometry of moulded cores is limited by the non-isostatic pressure generated during the compression moulding process, as the salt/sugar mix does not flow when pressed. Large variations in mechanical properties can occur in complex cores due to different local compaction ratios. One solution is to cast a large block and then machine it to the final required geometry. This also creates opportunities for using this water-soluble core for lower volume applications, where the high cost of capital equipment and tooling cannot be amortised over the lifetime of the component. Trials have been conducted to demonstrate the feasibility of machining cast blocks of the NT Core material using two types of cutter: a ball-nose and an end mill. Only one configuration of the NT Core material was tested during this study, which was the configuration that gave the highest mechanical properties in Section 8.4 (The processing parameters for producing the NT Cores for this study were; pressure 170bar, binder content 8wt%, temperature 150°C and processing time 30min).

Figure 8.12 (a) shows that chipping was evident after milling the NT Core with a flat end mill. Damage occurred on the upper cut edges (Figure 8.12 (b)), which is indicated by the surface roughness value, R_a , in Table 8.5. The R_a values taken at Position 4 (which corresponds to the corner between the cut face and moulded face as shown in Figure 8.3), are the only ones that significantly differ to the R_a values taken from the as-moulded surface (Position 1) - $\sim 108\mu\text{m}$ VS $\sim 8\mu\text{m}$. Damage at this location occurs only during the first few cuts, as the flat end mill has a fixed and relatively small rake angle, which causes high cutting forces to be applied to the top surface of the core [137]. Chips therefore occur since there is no support for the

surrounding material. However, cuts tend to become cleaner as the depth of the end-mill cutter increases, as indicated by the surface roughness measurements at Position 6 in Figure 8.12 (b).

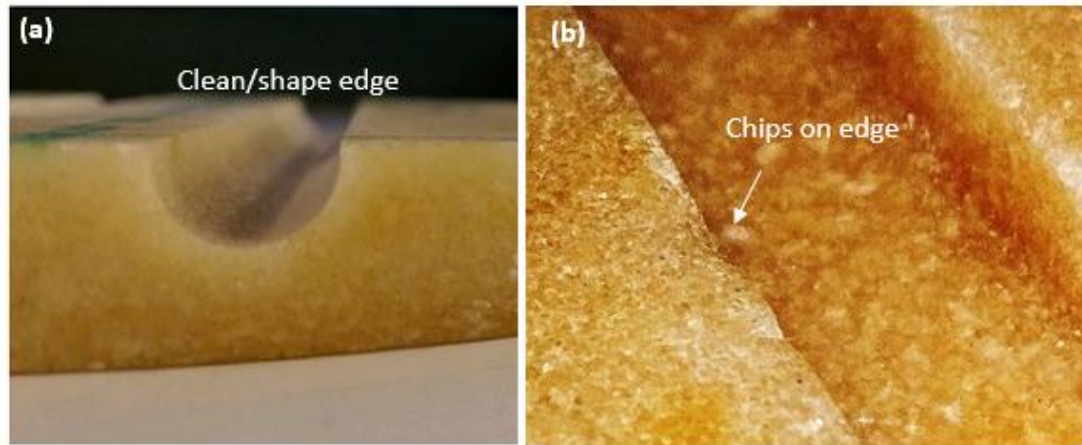


Figure 8.12 The NT Core after end-milling with a Ø10mm ball-nose cutter (a), a Ø10mm flat cutter (b)

Table 8.5 Roughness Ra at 6 locations (1 – Top surface; 2 – Cutting edge/Ball-nose cutter; 3 – Cutting surface/ Ball-nose cutter; 4 – Cutting edge/Flat cutter; 5 – Cutting surface/Flat cutter; 6 – Inner cutting edge/Flat cutter;)

Location	1	2	3	4	5	6
Ra (µm)	8.19	9.08	4.99	108.62	5.81	2.91

Conversely, a clean cut can be produced with a ball-nosed cutter of a similar diameter, with no chipping during breakout. The contact area of the ball-nose cutter is initially lower and the rake angle increases gradually with increasing cutter depth. Therefore, for the same spindle speed, there is less cutting torque applied on the cutting edge and the cutting force increases more gradually for subsequent cuts as the contact areas increases. More in-depth machining trials are required to be more conclusive, but this initial study has demonstrated the feasibility of machining large cast billets for producing complex geometries if casting net-shaped cores is not cost effective for low production volumes.

Post composite moulding core removal trials have also been conducted to compare the removal rate of the NT Core material with that of the commercial B Core. Figure 8.13 compares core removal rates for the NT Core and the B Core, using a water jet at 8 bar and 40°C. The B Core has a faster removal rate than the NT Core (fully removed after 15 seconds compared to 30 seconds) due to its low strength (5.1MPa for the B Core versus 49.0 MPa for the NT Core). For the case shown in Figure 8.14 (b), the 50.1g NT Core (27 cm³) was fully removed from the blind hole (open area of 338 mm²) in approximately 30 seconds, hence, the average removal rate was 54 cm³/min or 100.2 g/min, leading to a specific removal rate of 296 kg/(min·m²). The pressurised water therefore significantly improves the removal speed of the core compared with the SDR recorded by the water bath method (0.25 kg/(min·m²)), as the pressurised water provides some mechanical assistance to remove the core rather than solely relying on the dissolution of the salt and sugar.

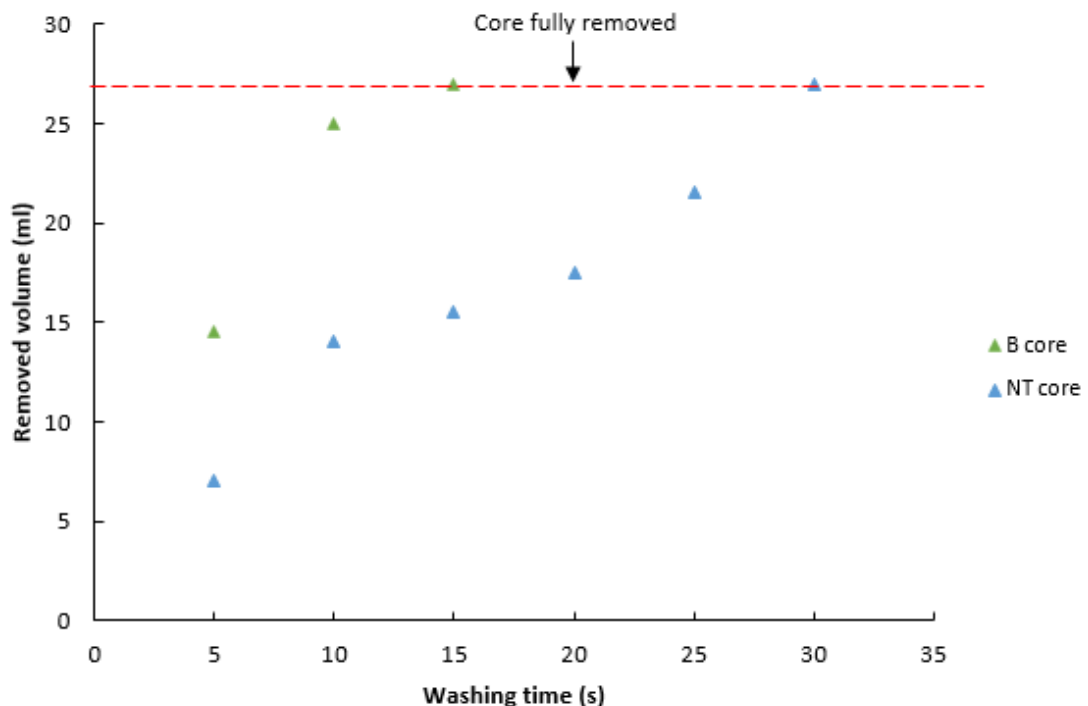


Figure 8.13 The change in volume of B Core and NT Core (8wt.% binder content, pressed at 150°C and 170bar for 30min) during water jet trials

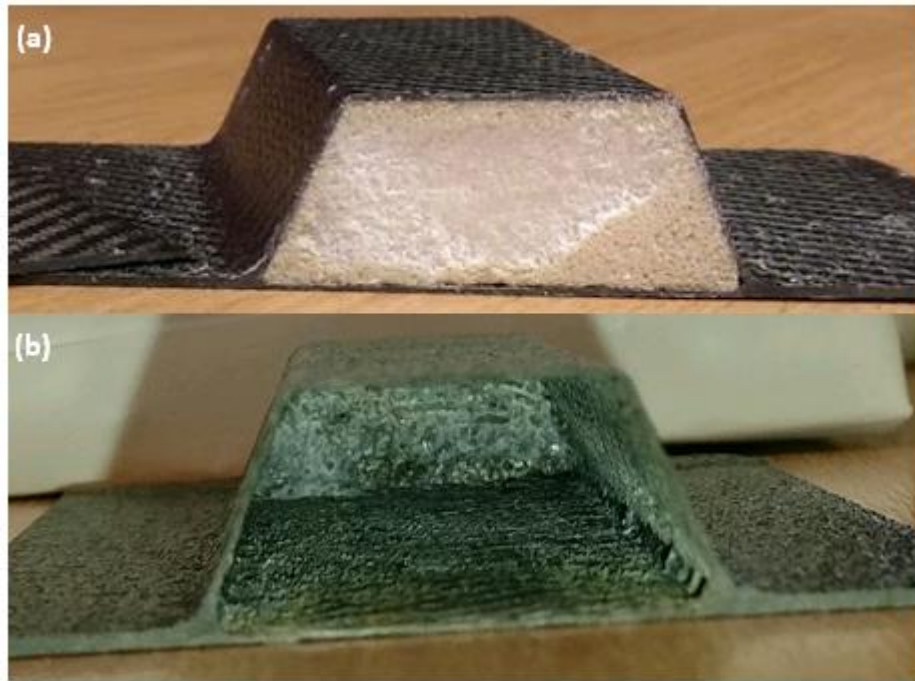


Figure 8.14 An open-ended integrally-stiffened prepreg panel (a) NT Core in position and (b) after NT Core removal, showing blind hole

8.11 Conclusions

A water-soluble NaCl-based core (NT Core) has been developed to enable complex hollow composite structures to be manufactured. Mechanical testing has shown that a compressive strength of 57.3 MPa and a flexural strength of 10.2 MPa can be achieved at ambient temperature. Although there is a clear reduction in mechanical properties at temperatures up to 120 °C, the results indicate that the core is suitable for high pressure moulding processes, such as compression moulding or HP-RTM, where in-mould pressures can exceed 100 bar. According to a statistical study, the mechanical performance of the core increases with increasing binder content, processing pressure, processing temperature, and processing time. However, the optimal processing temperature was found to be 150 °C, as the trehalose binder undergoes a phase change to a stable anhydrate and a state change to a liquid,

enabling the binder to flow into the pores between the salt grains. Degradation of the binder was observed if the processing temperature was too high (190 °C) for long periods (over 30 min), significantly reducing the mechanical performance of the core.

Integrally-stiffened composite panels produced using the NT Core demonstrate that this material can be successfully removed by pressurised water through a blind hole, in order to produce hollow carbon fibre structures. Compared to other NaCl-based cores reported in the literature, the specific dissolution rate of the newly developed NT Core (170 bar and at 150 °C for 30 min, 8 wt% binder) is approximately 5 times faster ($0.25 \text{ kg}/(\text{min}\cdot\text{m}^2)$), since a water soluble binder has been used instead of relying on heavy mechanical interlocking of the salt grains. However, the overall removal rate ($54 \text{ cm}^3/\text{min}$) is around half that of the commercial benchmark (B Core) because of higher mechanical properties (flexural strength of 10 MPa vs. 4.8 MPa). The main removal mechanism of the core is fracture by the kinetic energy of the water-jet, rather than dissolution. However, this is an inevitable compromise, as the superior mechanical performance is key to utilising this material for high-pressure composite moulding processes.

Chapter 9 Thesis conclusions

Due to strict emission regulations, there is an increasing need for lightweight materials in the automotive industry. Carbon fibre composites are applied in modern vehicle designs, because they offer low density ($\sim 1.6 \text{ g/cm}^3$) and high specific strength and stiffness. The DCFP process is a rapid (5 – 10 min cycle time) manufacturing technique that generates low material wastage ($< 5\%$). High material areal mass variability ($\pm 20\%$) is a major drawback however, which leads to lower mechanical properties. The present work investigates the source of the variability in terms of the preforming process, the moulding process and the selection of the constituent materials for DCFP components.

9.1 Fibre volume fraction variability reduction

In the first part of the work, the fibre deposition path was characterised. It was found that there was a bias between the fibre preforming path and the robot path, because of the inertia of fibres falling from the chopper gun. Additionally, the wide fibre deposition path makes it difficult to accurately control the local and global areal mass of preforms. Reducing the Tool Centre Point (TCP) height yielded the most significant reduction in the path bias and the width of the fibre preforming path. The robot path was shifted in the x-y plane to compensate for the path bias and TCP height was lowered down to improve preforming resolution and accuracy. By using this optimisation strategy, a low areal mass variability ($< 5\%$) was achieved for 2D preforms. According to the tensile results from 2D moulded DCFP plaques, the low error between tensile properties at 0° and 90° ($< 3\%$) and low inter-plaque variability

(< 3%) demonstrate that the changes to the fibre deposition strategy have improved the preforming process to ensure repeatability and quasi- isotropic properties.

9.2 Complex 3D component manufacturing

The preforming optimisation strategy was also applied during the development of a complex 3D automotive preform, achieving an areal mass variation of less than 5%. However, the poor fibre chopper gun spray cone resolution compared to the scale of the component meant that overspray on the sharp corners and sloping sides was difficult to avoid, increasing fibre wastage compared to planar components, such as automotive closure panels.

9.3 High pressure DCFP moulding

DCFP preforms are typically moulded by conventional RTM. At the start of this work it was unclear whether DCFP was suitable for moulding processes with high in-mould pressures (>100 bar). Three moulding processes (RTM, HP-RTM, Compression moulding) were selected to investigate the compatibility of DCFP and high pressure processes, by considering the mechanical properties of DCFP components. Compared to RTM, HP-RTM and compression moulding reduce the manufacturing cycle by approximately 60%. In addition to improving production rate, HP-RTM helps to achieve lower void content (0.6%), while compression moulding improves the homogeneity of the fibre distribution through in-mould charge flow. Consequently, higher moulding pressures yield higher tensile strength values for DCFP plaques.

The high resin injection pressure in HP-RTM challenges the integrity of the random discontinuous fibre architecture, as fibre washing can occur. Powdered binders are

typically applied to DCFP preforms to retain the fibre structure during handling and moulding. However, from previous studies, the effect of binder on integrity of preforms and mechanical properties are not well understood. In this work, two types of binders (Momentive EP05390 (unreactive) and EPS620 (reactive)) were selected for investigation. When the binder level is increased from 5wt.% to 15wt.%, the EPS620 binder provides a higher bonding strength compared to the EP05390 binder, ranging from 210N to 1625N for dry preforms (versus 102 N to 388 N). The EPS620 binder penetrates deeper within the fibre tows when heated to 90 °C rather than forming droplets on the surface, encapsulating more filaments. The EPS620 binder successfully prevented fibre washing during HP-RTM injection at 150 bar. Whereas, a large degree of fibre distortion was observed in the moulded DCFP plaques when the EP05390 binder was used, because the bulk resin temperature was the same as the binder melt temperature at 80°C for this unreactive system. This fibre distortion led to a reduction in tensile strength of 12MPa, compared to the non-fibre-distortion plaques with the strength of 306MPa. There was a negligible effect (~1%) on tensile strength when the EPS620 binder content increased from 5 wt.% to 10 wt.% for DCFP plaques.

Although the binder content does not significantly influence the tensile properties of DCFP plaques, it significantly affects preform permeability, which governs the moulding process time. When the EPS620 binder content increased from 5 wt.% to 10 wt.%, the permeability of DCFP preforms with a fibre volume fraction of 31% reduced by 27%, since binders obstruct the fluid flow. When the V_f increased to 46%, the inter and intra bundle spacings reduced, therefore the negative effect of higher binder content on permeability became less significant (16%). This indicates that the

inter-bundle spacings dominate the permeability more than the binder content for DCFP preforms.

9.4 Numerical permeability modelling

Due to the areal mass variability of DCFP preforms, at least 10 permeability measurements were needed to achieve a representative mean value, which was time consuming. Hence, a numerical permeability model was developed in this work, aiming to provide an accurate and time-efficient prediction. A DCFP architecture programme was used to create realistic three dimensional fibre architectures with random inter-bundle spacing. In order to accurately transfer the geometry information from the 3D model to PAM-RTM for permeability simulation, a fibre architecture analysis programme was developed. It was used to project the fibre position, orientation, and random inter-bundle spacing onto the mesh of a PAM-RTM model. The model successfully simulated the irregular flow front, which is typically observed in experimental permeability measurements.

The newly developed permeability model not only includes the effect of realistic fibre distributions but also the effect of binder. The model indicates realistic reductions in permeability when the binder content is increased from 5 wt.% to 10 wt.%, for the two fibre volume fractions studies (V_f of 31% and 46%). The permeability reduced by 22% at a V_f of 31% and 16% at a V_f of 46%, which is comparable to the reductions observed experimentally. However, the magnitude of the simulated permeability values were approximate 100% higher than the experimental values. This overestimation can be ascribed to ignoring the out-of-plane angle of fibre bundles within the fibre architecture generation model. The new 3D model provides an

effective upper bound for the permeability of DCFP preforms, whereas the previous 2D model provides a lower bound values when assuming evenly distributed tows through the thickness of the laminate.

9.5 Mechanical property improvement using high strength and high modulus fibres

An experimental study was conducted to investigate the effect of carbon fibre properties on the mechanical performance of DCFP components. It was found that the ultimate strength of DCFP plaques converged to ~300 MPa, regardless of the fibre type, which is consistent with data collated from previous studies. The presence of resin-rich region limited achieving higher strengths. Hence, 300 MPa is the upper bound for tensile strength when designing a DCFP component at a V_f of 50% for standard (non-toughened) liquid epoxy resin systems. The homogeneity of the fibre distribution significantly influences the strength and stiffness of DCFP components. The low homogeneity factor of 2.9 tow/cm² corresponds to local areal mass variability values of up to 13%. Hence, the tensile strength value is less than 100MPa and the measured stiffness value is less than half of the analytical stiffness value.

Hybrid fibre structures were investigated to provide a compromise between mechanical performance and cost. Two carbon fibres, T700 (Fibre 1) and K13916 (Fibre 5), were selected to manufacture a hybrid DCFP performs with homogenous distribution to avoid large stress concentration regions. The T700 fibre has high strength (4900 MPa), while the K13916 fibre has high modulus (760 GPa). The Hybrid fibre DCFP plaque (T700 90 vol.% and K13916 10 vol.%) offers similar tensile strength

and stiffness to fibres that cost 9 times more (30 €/kg VS 270 €/kg). The hybrid fibre architecture also absorbs three times more impact energy (106 kJ/m² VS 36 kJ/m²).

9.6 Rapid Young's modulus measurement technique

Sample preparation and tensile testing are time consuming. The impulse excitation technique (IET) is a fast and simple Young's modulus measurement method typically used for homogenous materials (e.g. metals). In the present work, IET was selected to investigate whether it is suitable for DCFP components with inherent material variability. The results indicated that the difference between the stiffness values from IET and conventional tensile testing was within 3%. Therefore, this method offers a rapid stiffness measurement method that can potentially be applied to the DCFP production line to check quality of components in real time.

9.7 Novel water-soluble core development for manufacturing hollow composite sections

The DCFP study in this thesis indicates that discontinuous fibre preforms can be successfully moulded by high pressure moulding processes, such HP-RTM and compression moulding, to provide low-cost materials for high volume production of lightweight carbon fibre composite components. To complement these developments, a novel water-soluble NaCl-based core was investigated to produce complex hollow composite structures by HP-RTM and compression moulding. The core was composed from salt grains and a trehalose sugar binder (NT Core).

With compressive strengths of 57.3 MPa and 19.7 MPa at ambient temperature and at 120 °C respectively, the NT core is considered to be suitable for high pressure moulding processes where in-mould pressures can exceed 100 bar. A statistical

experimental study was conducted which showed that increasing binder content, processing pressure, processing temperature and processing time maximised the mechanical properties of the core. However, there is an optimal processing temperature at 150 °C, as the trehalose binder undergoes a phase change to a stable anhydrate and a state change to a liquid, enabling the binder to flow into the pores between the salt grains to enhance bonding. When the processing temperature was too high (190 °C) for long periods (over 30 min), degradation of the binder was observed, causing significant reduction in the mechanical properties of the core. In addition to superior mechanical properties, the NT core (170 bar and at 150 °C for 30 min, 8 wt% binder) also offers a 5 times faster specific dissolution rate ($0.25 \text{ kg}/(\text{min}\cdot\text{m}^2)$) than other commercial NaCl-based cores. With the aid of pressurised water at 8 bar, an overall removal rate of $54 \text{ cm}^3/\text{min}$ was achieved, which equates to a specific removal rate of $296 \text{ kg}/(\text{min}\cdot\text{m}^2)$.

In the case of integrally-stiffened composite panels produced using the NT Core, it was successfully demonstrated that this material can be removed by pressurised water from a blind hole to create hollow carbon fibre structures. Machining trials of the core also demonstrate the ability of this NT core to produce complex geometries by post machining.

9.8 Future work

Based on the work has been done in this thesis, future work could include the following:

1. Advanced 3D DCFP model with CFD for permeability prediction. Current permeability modelling method is projecting a 3D DCFP model to a 2D plane, so some information was incorrectly transferred or missed, such as out-of-plane angle of a tow. This causes inaccurate prediction. In future, a fibre tow model should use 3D solid elements rather than using 2D shell elements to give a more realistic fibre architecture and flow channels. Additionally, the morphology of the binders on fibre tows can be included in the new model. The new model then can be input into CFD for accurate flow simulation. Although this is a time-consuming process, the prediction will be more accurate.
2. Further development of the water-soluble core. In this thesis, the characterisations for the mechanical properties of the core have been conducted. The resistance to humidity of the core also needs to understand, as the materials are water-soluble. Furthermore, the heat transfer of the core also need to investigate, as the properties of trehalose, the binder, are related to temperature. When manufacturing a core with large size, it needs to make sure all the materials from centre to the edge can reach to the designed temperature as soon as possible to reduce manufacturing cycle.

Appendices

Appendix A List of publication

1. **'A water-soluble core material for manufacturing hollow composite sections'**, Z. Xiao, L. T. Harper, A. R. Kennedy, N. A. Warrior, Composite Structures, Volume 182, 2017
2. **'Characterisation of random carbon fibre composites from a directed fibre preforming process: The effects of moulding process and fibre type'**, Z. Xiao, A.D. Evans, T.A. Turner, L. T. Harper, N. A. Warrior
Awaiting submission

Appendix B Matlab code of the Fibre Architecture Analysis Programme

```
gs=input('Grid size is ','s');
tgs=str2num(gs);
ch=input('Cavity Height is ','s');
CH=str2num(ch);
bc=input('Binder weight % is ','s');
BC=str2num(bc);
%% Load data and build matrix
NodesFileName=sprintf('Nodes.txt');
ElementsFileName=sprintf('Elements.txt');
OriFileName=sprintf('Ori.txt');
load(NodesFileName);
load(ElementsFileName);
load(OriFileName);

mgx = fix(280/tgs);
mgy = fix(110/tgs);
Matrix=cell(mgy,mgx);
for n=1:mgy
    for m=1:mgx;
        Matrix{mgy-n+1.,m}=0;
    end
end

%%Orientation
LOri=length(Ori(:,1));

for e=1:LOri;
    newX=Ori(e,1)-Ori(e,7);
    newY=Ori(e,2)-Ori(e,8);
    Ori(e,10)=acos(newX./sqrt(newX.^2+newY.^2));
end

%% Locating
ttn = max(Nodes(:,5)) + 1;
TowLengthE=zeros(1,ttn);
TowLengthN=zeros(1,ttn);
for i=0:ttn-1.;
    s=sum(Nodes(:,5)==i);
    TowLengthN(1,i+1)=s;
end

for n=1:mgy;
    for m=1:mgx;
        for v=0:ttn-1.;
            if (v == 0)
                X=Nodes(1:TowLengthN(1,v+1),2);
                Y=Nodes(1:TowLengthN(1,v+1),3);
                gridxN=fix(X./tgs+1);
                gridyN=fix(Y./tgs+1);
```

```

        l=length(gridxN);
        Count = 0;
        for j=1:l
            a=gridxN(j,1);
            b=gridyN(j,1);
            if (n==b && m==a)
                Count = Count + 1;
            end
        end
        if (Count >= ((tgs*tgs)*0.70/0.333));
            Matrix{mgy - n + 1.,m}(1,1)=Matrix{mgy - n +
1.,m}(1,1)+1;

            Matrix{mgy - n + 1.,m}(1,2)=Ori(v+1.,10);

            end

        else

            LN=sum(TowLengthN(1,1:v));
            LE=sum(TowLengthE(1,1:v));

            X=Nodes((LN+1.): (LN+TowLengthN(1,v+1)),2);
            Y=Nodes((LN+1.): (LN+TowLengthN(1,v+1)),3);
            gridxN=fix(X./tgs+1);
            gridyN=fix(Y./tgs+1);
            l=length(gridxN);
            Count = 0;
            for j=1:l
                a=gridxN(j,1);
                b=gridyN(j,1);
                if (n==b && m==a)
                    Count = Count + 1;
                end
            end
            if (Count >= ((tgs*tgs)*0.7/0.333));
                Matrix{mgy - n + 1.,m}(1,1)=Matrix{mgy - n +
1.,m}(1,1)+1;

                Ml=length(Matrix{mgy - n + 1.,m});
                Matrix{mgy - n + 1.,m}(1,Ml+1.)=Ori(v+1.,10);

                end

            end

        end

    end

    end

%% Spacing
Nodes(:,2)=fix(Nodes(:,2)/tgs+1.);
Nodes(:,3)=fix(Nodes(:,3)/tgs+1.);
l1=length(Nodes(:,4));
for n=1:mgy;
    for m=1:mgx;
        if (Matrix{mgy - n + 1.,m}(1,1) ~= 0);

```

```

        if (Matrix{mgy - n + 1.,m}(1,1)*(0.1646+BC*0.0012*2) <
2);
    GridZ=zeros(0);
    for ii=1:11;
        if (Nodes(ii,2)== m && Nodes(ii,3)== n);
            GridZ=[GridZ;Nodes(ii,4),Nodes(ii,5)];
        end
    end

    GL=length(GridZ(:,1));
    TLengthGrid=zeros(0);
    for v=0:(ttn-1.);
        s=sum(GridZ(:,2)==v);
        if (s >= ((tgs*tgs)*0.7/0.333));
            TLengthGrid(1,v+1)=s;
        else
            TLengthGrid(1,v+1)=0;
        end
    end

    TLengthGrid(TLengthGrid==0)=[];
    LT=length(TLengthGrid);

    LocationZ=zeros(0);
    Spacing=zeros(0);

    for vj=1:LT;

        if (vj == 1);
            LocationZ(1,vj) =
mean(GridZ(1:TLengthGrid(1,vj),1));

        else
            LGZ=sum(TLengthGrid(1,1:(vj-1.)));
            LocationZ(1,vj) =
mean(GridZ((LGZ+1):(LGZ+TLengthGrid(1,vj))),1));
        end
        end
        LocationZ = sort(LocationZ);

        for ii=2:(length(LocationZ));
            if (LocationZ(1,ii) - LocationZ(1,ii-1) <=
(0.1646+BC*0.0012*2));
                LocationZ(1,ii) = LocationZ(1,ii-1) +
(0.1646+BC*0.0012*2);
            end
        end

        if (LocationZ(1,length(LocationZ)) >= CH);
            LocationZ(1,length(LocationZ)) = CH - 0.001;
        end

        LLZ = length(LocationZ);
        if (LocationZ(1,LLZ) >= (CH - 0.0823 - BC*0.0012));
            LocationZ(1,LLZ) = CH - 0.0823 - BC*0.0012;
            LocationZ(1,(LLZ-1)) = LocationZ(1,LLZ) -
0.1646 - BC*0.0012*2;

```

```

        for ii=1:(LLZ-2);
            if (LocationZ(1,(LLZ-ii)) - LocationZ(1,(LLZ-
ii-1)) <= (0.1646+BC*0.0012*2));
                LocationZ(1,(LLZ-ii-1)) = LocationZ(1,(LLZ-ii))
- (0.1646+BC*0.0012*2);
            end
        end
    end

    for uu=1:length(LocationZ);
        if (uu == 1);
            Spacing(1,uu) = LocationZ(1,1);
        else
            LGZ=sum(LocationZ(1,1:(uu-1)));
            Spacing(1,uu) = LocationZ(1,uu) -
LocationZ(1,(uu-1));
        end
    end
    Spacing(1,length(Spacing)+1.) = CH - max(LocationZ) -
0.0823 - BC*0.0012;

    if (Spacing(1,1) <= (0.0823 + BC*0.0012))
        Spacing(1,1) = 0;
    else
        Spacing(1,1) = Spacing(1,1) - 0.0823 - BC*0.0012;
    end

    for u = 2:(length(Spacing) - 1);
        if (Spacing(1,u) <= (0.1646+BC*0.0012*2))
            Spacing(1,u) = 0;
        else
            Spacing(1,u) = Spacing(1,u) -
(0.1646+BC*0.0012*2);
        end
    end

    if (Spacing(1,length(Spacing)) <= (0.0823 +
BC*0.0012))
        Spacing(1,length(Spacing)) = 0;
    else
        Spacing(1,length(Spacing)) =
Spacing(1,length(Spacing)) - (0.0823 + BC*0.0012);
    end

    for u = 1:length(Spacing);
        Ml=length(Matrix{mgy - n + 1.,m});
        Matrix{mgy - n + 1.,m}(1,(Ml+1))=Spacing(1,u);
    end
end

end

end

end

%% Output file

```

```

OutPut=cell(0);
for n=1:mgY;
    for m=1:mgX;

        OutPut=[OutPut;m,n,Matrix{mgY - n + 1.,m}];

    end
end

fid = fopen( 'OutPut.txt', 'w' ) ;
for cId = 1 : numel( OutPut )
    fprintf( fid, '%g', OutPut{cId} ) ;
    fprintf( fid, '\r\n' ) ;
end
fclose( fid ) ;

```

References

1. *Paris Agreement*. 2016: Paris.
2. *Reducing CO2 emissions from passenger cars*. [cited 2017; Available from: https://ec.europa.eu/clima/policies/transport/vehicles/cars_en#tab-0-0.
3. Roper, L.D. *Musings about electric vehicles (EVs)*. 2016 [cited 2017; Available from: <http://www.roporld.com/science/ElectricCarsMusings.pdf>.
4. Helms, H. and Lambrecht, U., *The Potential contribution of light-weighting to reduce transport energy consumption*. Int J LCA, 2006. **7**: p. 1-7.
5. Kochan, A., *Audi moves forward with all-aluminium cars*. Assembly Automation, 2000. **20**(2): p. 132-135.
6. Taylor, K.C. and Sanchdev, A., *Energy and Transportation: Challenges for the Chemical Sciences in the 21st Century*. 2003, Washington: The National Academy Press.
7. Norris, R.E., Lomax, R.D., Xiong, F., Dahl, J.S., and Blanchard, P.J., *Advanced high speed programmable preforming*. Oak Ridge National Laboratory (ORNL), 2010.
8. Harper, L.T., *Discontinuous Fibre Composites for Automotive Applications*. 2006, University of Nottingham.
9. *Sharper, lighter and more powerful – the all-new Audi R8 heads for Geneva*. 2015 [cited 2017; Available from: <https://www.audi.co.uk/about-audi/latest-news/sharper-lighter-and-more-powerful-the-all-new-audi-r8-heads-for-geneva.html>.
10. Lukaszewicz, D.H.J.A., Ward, C., and Potter, K.D., *The engineering aspects of automated prepreg layup: History, present and future*. Composites Part B: Engineering, 2012. **43**(3): p. 997-1009.
11. Marsh, G., *Automating aerospace composites production with fibre placement*. Reinforced Plastics, 2011. **55**(3): p. 32-37.
12. Latorre, C. *BMW i3: carbon fiber body*. 2013 [cited 2017; Available from: <http://www.plastix-world.com/bmw-i3-carbon-fiber-body/>.
13. Howard, B. *How BMW weaves, bakes, and builds the carbon fiber 7 Series*. 2015 [cited 2017; Available from: <https://www.extremetech.com/extreme/209812-how-bmw-weaves-bakes-and-builds-the-carbon-fiber-7-series>.
14. Rybicka, J., Tiwari, A., Alvarez Del Campo, P., and Howarth, J., *Capturing composites manufacturing waste flows through process mapping*. Journal of Cleaner Production, 2015. **91**(Supplement C): p. 251-261.
15. Wood, K. *Carbon fiber reclamation: Going commercial*. 2010 [cited 2017; Available from: <https://www.compositesworld.com/articles/carbon-fiber-reclamation-going-commercial>.
16. *BMW i3: first mass produced composite car in production*. <http://www.drycomposites.com/bmw-i3-first-mass-produced-composite-car-in-production/>.
17. Kirupanantham, G., *Characterisation of discontinuous carbon fibre preforms for automotive applications*. 2013, University of Nottingham.
18. Helps, I.G., *lastics in European Cars 2000-2008: A Rapra Industry Analysis Report*. 2001: Rapra Technology.
19. Croizat, H. and B., B., *New possibilities with HexMC, a high performance molding compound*, in *Sixth International Seminar on Experimental Techniques and Design in Composite Materials*. 2003: Vicenza, Italy.

20. Giocosa, A., *Composite material parts in Renault cars: The past, the present and the future*, in *The 8th International Conference on Flow Processes in Composite Materials (FPCM8)*. 2006: Douai, France.
21. Jacob, A. *TenCate to supply carbon fibre prepreg for Alfa Romeo 4C monocoque*. 2014 [cited 2017; Available from: <http://www.materialstoday.com/composite-applications/news/tencate-to-supply-carbon-fibre-prepreg-for-alfa/>].
22. *Corvette sports a carbon composite bonnet*. Reinforced Plastics,, 2003. **47**(7).
23. Kaczmarczyk, M. and Langschwager, T., *Carbon fiber SMC technology for lightweight structures*. Vol. 1. 2013. 490-505.
24. Lamborghini. *Huracan Performante Racing Technology*. 2017 [cited 2017; Available from: <https://www.lamborghini.com/en-en/models/huracan/huracan-performante>].
25. Hexcel reports material use in 787 Dreamliner. 2011 [cited 2017; Available from: <https://www.compositesworld.com/news/hexcel-reports-material-use-in-787-dreamliner>].
26. Chavka, N.G. and Dahl, J.S., *P4: Glass fiber preforming technology for automotive applications*, in *44th International SAMPE Symposium*. 1999: Long Beach, CA.
27. Black, S. *High-Volume Preforming for Automotive Application*. 2008 [cited 2017; Available from: <http://www.compositesworld.com/articles/high-volume-preforming-for-automotive-application>].
28. Vaidya, U., *Composites for Automotive, Truck and Mass Transit: Materials, Design, Manufacturing*. 2011: DEStech Publications.
29. Gardiner, G. *Sixth Element: Lamborghini accelerates CFRP*. 2012 [cited 2017; Available from: <https://www.compositesworld.com/articles/sixth-element-lamborghini-accelerates-cfrp>].
30. Qian, C.C., *Structural optimisation of discontinuous carbon fibre composites*. 2013, University of Nottingham.
31. Harper, L.T., Turner, T.A., Martin, J.R.B., and Warrior, N.A., *Fiber Alignment in Directed Carbon Fiber Preforms - A Feasibility Study*. *Journal of Composite Materials*, 2009. **43**(57): p. 57-74.
32. Yu, H., Potter, K.D., and Wisnom, M.R., *A novel manufacturing method for aligned discontinuous fibre composites (High Performance-Discontinuous Fibre method)*. *Composites Part A: Applied Science and Manufacturing*, 2014. **65**(Supplement C): p. 175-185.
33. Corbridge, D.M., Harper, L.T., De Focatiis, D.S.A., and Warrior, N.A., *Compression moulding of composites with hybrid fibre architectures*. *Composites Part A: Applied Science and Manufacturing*, 2017. **95**(Supplement C): p. 87-99.
34. Evans, A.D., Harper, L.T., Turner, T.A., and Warrior, N.A. *Joint Design of Continuous/Discontinuous Hybrid Carbon Fibre Composites*. in *21st International Conference on Composite Materials*. 2017. Xi'an, China.
35. Rohacell IG/IG-F mechanical properties. Available from: <http://www.rohacell.com/sites/lists/PP-HP/Documents/ROHACELL-IG-IG-F-mechanical-properties-EN.pdf>.
36. Graf, M., Fries, E., Rehkl, J., Henning, F., R., C., and Thoma, B., *High pressure resin transfer moulding-Process advancements*, in *10th ACCE* 2010.
37. Ritter, K. *RTM advances facilitate mass production in the automotive market*. 2012; Available from: <http://www.materialstoday.com/composite-applications/features/rtm-advances-facilitate-mass-production-in-the/>.
38. Zajonz, A. and Stoger, W. *In-Mold Foamed Cores for Lightweight Design*. 2015; Available from: http://www.rohacell.com/sites/lists/PP-HP/Documents/KUint_2015_10%20In-Mold%20Foamed_.pdf.

39. Jelinek, P. and Adamkova, E., *Lost Cores for High-Pressure Die Casting*. Archives of Foundry Engineering, 2014. **14**(2/2014): p. 101-104.
40. Michels, H., Bunck, M., and Buhrig-Polaczek, A., *Suitability of lost cores in rheocasting process*. Trans. Nonferrous Met. Soc. China 2010. **20**: p. 948-953.
41. LaFay, V., *Application of No-Bake Sodium Silicate Binder Systems*. International Journal of Metalcasting, 2012. **6**(3): p. 19-26.
42. Jiang, W., Dong, J., Lou, L., Liu, M., and Hu, Z., *Preparation and Properties of a Novel Water soluble core material*. J. Mater. Sci. Technol., 2010. **26**: p. 270-275.
43. Sangeeta, D. and Niskayuna, N.Y., *Method of dissolving or leaching ceramic cores in airfoils*. 1998, General Electric Company.: US.
44. Amaro, A.M., Reis, P.N.B., Neto, M.A., and Louro, C., *Effects Of Alkaline And Acid Solutions On Glass/Epoxy Composites*. Polymer Degradation and Stability, 2013. **98**: p. 853-862.
45. Instructions - Aquacore WSC1024. Available from: http://www.northerncomposites.com/docs/default-source/data-sheets/instructions_aquacore.pdf?sfvrsn=2.
46. Turner, T.A., Harper, L.T., Warrior, N.A., and Rudd, C.D., *Low - cost carbon - fibre - based automotive body panel systems: a performance and manufacturing cost comparison*. Proceedings of the Institution of Mechanical Engineers, Part D: Journal of Automobile Engineering, 2008. **222**(1): p. 53-63.
47. Bodaghi, M., Cristóvão, C., Gomes, R., and Correia, N.C., *Experimental characterization of voids in high fibre volume fraction composites processed by high injection pressure RTM*. Composites Part A: Applied Science and Manufacturing, 2016. **82**(Supplement C): p. 88-99.
48. Khoun, L., Maillard, D., and Bureau, M.N. *Effect of process variables on the performance of glass fibre reinforced composites made by high pressure resin transfer moulding*. in *Proceedings of the 12th Annual Automotive Composites Conference and Exhibition (ACCE 2012)*. 2012.
49. Rosenberg, P., Chaudhan, R., Albrecht, P., Karcher, M., and Henning, F., *Effects of process parameters on cavity pressure and component performance in high-pressure RTM process variants*, in *SPE ACCE 2014*. 2014.
50. Endruweit, A., Harper, L.T., Turner, T.A., Warrior, N.A., and Long, A.C., *Random discontinuous carbon fibre preforms: Permeability modelling and resin injection simulation*. Composites Part A: Applied Science and Manufacturing, 2008. **39**(10): p. 1660-1669.
51. Bickerton, S. and Advani, S.G., *Characterization and modeling of race-tracking in liquid composite molding processes*. Composites Science and Technology, 1999. **59**(15): p. 2215-2229.
52. Zhou, F., Alms, J., and Advani, S.G., *A closed form solution for flow in dual scale fibrous porous media under constant injection pressure conditions*. Composites Science and Technology, 2008. **68**(3): p. 699-708.
53. Rudd, C., Long, A., Kendall, K., and Mangin, C., *Liquid Moulding Technologies*. 1997.
54. Luchoo, R., Harper, L.T., Bond, M.D., Warrior, N.A., and Dodworth, A., *Net shape spray deposition for compression moulding of discontinuous fibre composites for high performance applications*. Plastics, Rubber and Composites, 2010. **39**: p. 216-231.
55. Eckler, J.H. and Wilkinson, T.C., *Processing and designing parts using structural reaction injection molding*. Journal of Materials Shaping Technology, 1987. **5**(1): p. 17-21.
56. Mallick, P.K., *Processing of Polymer Matrix Composites: Processing and Applications*. 2017: CRC Press.

57. Gardiner, G. *HP-RTM on the rise*. 2014 [cited 2017; Available from: <https://www.compositesworld.com/articles/hp-rtm-on-the-rise>.
58. Chaudhari, R., Rosenberg, P., Karcher, M., Schmidhuber, S., Elsner, P., and Henning, F., *High-pressure RTM process variants for manufacturing of carbon fibre reinforced composites*, in *19th ICCM*. Montreal, Canada.
59. Rosenberg, P., Thoma, B., and Henning, F., *Investigation and validation of a new cavity pressure controlled HP-RTM process variant (PC-RTM)*, in *16th SPE Automotive Composites Conference & Exhibition*. 2016: Michigan, USA.
60. Hillermeier, R., Hasson, T., Friedrich, L., and Ball, C., *Advanced Thermosetting Resin Matrix Technology for Next Generation High Volume Manufacture of Automotive Composite Structures*. 2013, SAE International.
61. Cabrera-Ríos, M. and Castro, J.M., *An economical way of using carbon fibers in sheet molding compound compression molding for automotive applications*. *Polymer Composites*, 2006. **27**(6): p. 718-722.
62. Evans, A.D., Qian, C.C., Turner, T.A., Harper, L.T., and Warrior, N.A., *Flow characteristics of carbon fibre moulding compounds*. *Composites: Part A*, 2016. **90**: p. 1-12.
63. Harper, L.T., Turner, T.A., Warrior, N.A., Dahl, J.S., and Rudd, C.D., *Characterisation of random carbon fibre composites from a directed fibre preforming process: Analysis of microstructural parameters*. *Composites: Part A*, 2006. **37**: p. 2136-2147.
64. Harper, L.T., Turner, T.A., Warrior, N.A., and Rudd, C.D., *Characterisation of random carbon fibre composites from a directed fibre preforming process: The effect of fibre length*. *Composites: Part A*, 2006. **37**: p. 1863-1878.
65. Harper, L.T., Turner, T.A., Warrior, N.A., and Rudd, C.D., *Characterisation of random carbon fibre composites from a directed fibre preforming process: The effect of tow filamentisation*. *Composites: Part A*, 2007. **38**: p. 755-770.
66. Jacob, G.C., Starbuck, J.M., Fellers, J.M., and Simunovic, S., *Effect of Fiber Volume Fraction, Fiber Length and Fiber Tow Size on the Energy Absorption of Chopped Carbon Fiber–Polymer Composites*. *Polymer Composites*, 2005: p. 293-305.
67. Rondeau, R., Reeve, S.R., and Bond, G., *The effect of tows and filament groups on the properties of discontinuous fiber composites*, in *44th International SAMPE symposium & exhibition*. 1999: Long Beach (CA, USA).
68. Swolfs, Y., Gorbatiikh, L., and Verpoest, I., *Fibre hybridisation in polymer composites: a review*. *Composites Part A: Applied Science and Manufacturing*, 2014. **67**: p. 181-200.
69. Hayashi, T., *On the improvement of mechanical properties of composites by hybrid composition*, in *Proc 8th Intl Reinforced Plastics Conference*. 1972. p. 149-152.
70. Manders, P.W. and Bader, M.G., *The strength of hybrid glass/carbon fibre composites Part 1 Failure strain enhancement and failure mode*. *Journal of Materials Science*, 1981. **16**(8): p. 2233-2245.
71. Chang, D., *Hybrid-Fiber-Reinforced Sheet Molding Compound Composite*, in *Composite Materials: Testing and Design (6th Conference)*, I. Daniel, Editor. 1982. p. 85-100.
72. Ren, P., Zhang, Z., Xie, L., Ren, F., Jin, Y., Di, Y., and Fang, C., *Hybrid Effect on Mechanical Properties of M40-T300 Carbon Fiber Reinforced Bisphenol A Dicyanate Ester Composites*. *POLYMER COMPOSITES*, 2010: p. 2129-2137.
73. Diao, H., Bismarck, A., Robinson, P., and Wisnom, M.R., *PSEUDO-DUCTILE BEHAVIOR OF UNIDIRECTIONAL FIBRE REINFORCED POLYAMIDE-12 COMPOSITE BY INTRA-TOW HYBRIDIZATION* in *15TH EUROPEAN CONFERENCE ON COMPOSITE MATERIALS*. 2012: Venice, Italy.

74. Voigt, W., *Theoretische untersuchungen über die elasticitäts verhältnisse krystalle*. Abhandlungen der Gesellschaft der Wissenschaften zu Goettingen, 1887. **34**.
75. Cox, H.L., *The elasticity and strength of paper and other fibrous materials*. British Journal of Applied Physics, 1952. **3**: p. 72.
76. Krenchel, H., *Fibre Reinforcement: Theoretical and Practical Investigations of the Elasticity and Strength of Fibre-reinforced Materials*. 1964: Akademisk forlag.
77. Galiotis, C., Young, R.J., Yeung, P.H.J., and Batchelder, D.N., *The study of model polydiacetylene/epoxy composites*. Journal of Materials Science, 1984. **19**(11): p. 3640-3648.
78. Fukuda, H. and Chou, T.-W., *An Advanced Shear-Lag Model Applicable to Discontinuous Fiber Composites*. Journal of Composite Materials, 1981. **15**(1): p. 79-91.
79. Kelly, A. and Tyson, W.R., *Tensile properties of fibre-reinforced metals: Copper/tungsten and copper/molybdenum*. Journal of the Mechanics and Physics of Solids, 1965. **13**(6): p. 329-350.
80. Weibull, W., *A statistical distribution function of wide applicability*. Journal Of Applied Mechanics - ASME, 1951.
81. Shih, C. and Lee, L.J., *Tackification of textile fiber preforms in resin transfer molding*. Journal of Composite Materials, 2001. **35**(21): p. 1954-1981.
82. Estrada, G., Vieux-Pernon, C., and Advani, S.G., *Experimental Characterization of the influence of tackifier material on preform permeability*. Journal of Composite Materials, 2002. **36**(19): p. 2297-2310.
83. Kittelson, J.L. and Hackett, S.C., *Tackifier/resin compatibility is essential for aerospace grade resin transfer molding*, in *39th International SAMPE Symposium*. 1994. p. 83.
84. Hillermeier, R.W. and Seferis, J.C., *Interlayer toughening of resin transfer molding composites*. Composites Part A: Applied Science and Manufacturing, 2001. **32**: p. 721-729.
85. Chen, J., Backes, D., and Jayaraman, K., *Dynamics of Binder Displacement in Liquid Molding*. Polymer Composites, 1996. **17**(1): p. 23-33.
86. Qian, C., Harper, L.T., Turner, T.A., and Warrior, N.A., *Notched behaviour of discontinuous carbon fibre composites: Comparison with quasi-isotropic non-crimp fabric*. Composites Part A: Applied Science and Manufacturing, 2011. **42**(3): p. 293-302.
87. Harper, L.T., Turner, T.A., Warrior, N.A., and Rudd, C.D., *Characterisation of random carbon fibre composites from a directed fibre preforming process: The effect of tow filamentisation*. Composites Part A: Applied Science and Manufacturing, 2007. **38**(3): p. 755-770.
88. Harper, L.T., Qian, C.C., Luchoo, R., and Warrior, N.A., *3D geometric modelling of discontinuous fibre composites using a force-directed algorithm*. Journal of Composite Materials, 2016. **0**(0): p. 1-18.
89. Parnas, R.S. and Salem, A.J., *A comparison of the unidirectional and radial in-plane flow of fluids through woven composite reinforcements*. Polymer Composites, 1993. **14**(5): p. 383-394.
90. Collins, R.E., *Flow of fluids through porous materials*. Reinhold chemical engineering series, ed. C.R. Wilke. 1961, New York: Reinhold Publishing Corporation.
91. Wong, C.C., *Modelling the effects of textile preform architecture on permeability*. 2006, University of Nottingham.
92. Parnas, R.S., Howard, J.G., Luce, T.L., and Advani, S.G., *Permeability characterization. Part 1: A proposed standard reference fabric for permeability*. Polymer Composites, 1995. **16**(6): p. 429-445.

93. Endruweit, A., McGregor, P., Long, A.C., and Johnson, M.S., *Influence of the fabric architecture on the variations in experimentally determined in-plane permeability values*. Composites Science and Technology, 2005. **66**: p. 1778-1792.
94. Endruweit, A., Harper, L.T., Turner, T.A., Warrior, N.A., and Long, A.C., *Random Discontinuous Carbon Fiber Preforms Experimental Permeability Characterization and Local Modeling*. Polymer Composites, 2010. **31**(4): p. 569-580.
95. Kozeny, J., *Über kapillare Leitung des Wassers im Boden*. Sitzung Akademie der Wissenschaft, 1927. **136**: p. 271-306.
96. Carman, P.C., *Fluid flow through granular beds*. Transactions of the Institution of Chemical Engineers, 1937. **15**: p. 32-48.
97. Foley, M.E. and Gillespie, J.W., *Modeling the Effect of Fiber Diameter and Fiber Bundle Count on Tow Impregnation during Liquid Molding Processes*. Journal of Composite Materials, 2005. **39**(12): p. 1045-1065.
98. Endruweit, A., Gommer, F., and Long, A.C., *Stochastic analysis of fibre volume fraction and permeability in fibre bundles with random filament arrangement*. Composites Part A: Applied Science and Manufacturing, 2013. **49**: p. 109-118.
99. Amico, S. and Lekakou, C., *An experimental study of the permeability and capillary pressure in resin-transfer moulding*. Composites Science and Technology, 2001. **61**: p. 1945-1959.
100. Amico, S. and Lekakou, C., *Flow through a two-scale porosity, oriented fibre porous medium*. Transport in Porous Media, 2004. **54**(35-53).
101. Rohatgi, V. and Lee, L.J., *Moldability of tackified fiber preforms in liquid composite molding*. Journal of Composite Materials, 1997. **31**(7): p. 720-744.
102. Dickert, M., Berg, D.C., and Ziegmann, G., *Influence of binder activation and fabric design on the permeability of non-crimp carbon fabrics*, in FPCM11. 2012: Auckland.
103. Brody, J.C. and Gillespie, J.W., *The Effects of a Thermoplastic Polyester Preform Binder on Vinyl Ester Resin*. Journal of Thermoplastic Composite Materials, 2005. **18**(3): p. 157-179.
104. Gebart, B.R., *Permeability of Unidirectional Reinforcements for RTM*. Journal of Composite Materials, 1992. **26**(8): p. 1100-1133.
105. Endruweit, A., Harper, L.T., Turner, T.A., Warrior, N.A., and Long, A.C., *Random discontinuous carbon fibre preforms Permeability modelling and resin injection simulation*. Composites: Part A, 2008. **39**: p. 1660-1669.
106. Ni, J., Zhao, Y., Lee, L.J., and Nakamura, S., *Analysis of two-regional flow in liquid composite molding*. Polymer Composites, 1997. **18**(2): p. 254-269.
107. Ngo, N.D. and Tamma, K.K., *Microscale permeability predictions of porous fibrous media*. International Journal of Heat and Mass Transfer, 2001. **44**: p. 3135-3145.
108. Deléglise, M., Le Grogne, P., Binetruy, C., Krawczak, P., and Claude, B., *Modeling of high speed RTM injection with highly reactive resin with on-line mixing*. Composites Part A: Applied Science and Manufacturing, 2011. **42**(10): p. 1390-1397.
109. Harper, L., Qian, C., Luchoo, R., and Warrior, N., *3D geometric modelling of discontinuous fibre composites using a force-directed algorithm*. Journal of Composite Materials, 2017. **51**(17): p. 2389-2406.
110. *PRIME 20LV Epoxy Infusion System*. [cited 2017; Available from: <http://www.gurit.com/Our-Business/Composite-Materials/Other-Products/Laminating-Infusion-Systems/PRIME-20LV>].
111. Park, C.H., Lebel, A., Saouab, A., Breard, J., and Lee, W.I., *Modeling and simulation of voids and saturation in liquid composite molding processes*. Composites: Part A, 2011. **42**: p. 658-668.

112. Ruiz, E., Achim, V., Soukane, S., Trochu, F., and Breard, J., *Optimization of injection flow rate to minimize micro/macro-voids formation in resin transfer molded composites*. Composites Science and Technology, 2006. **66**: p. 475-486.
113. Leclerc, J.S. and Ruiz, E., *Porosity reduction using optimized flow velocity in Resin Transfer Molding*. Composites: Part A, 2008. **39**: p. 1859-1868.
114. Lee, D.H., Lee, W.I., and Kang, M.K., *Analysis and minimization of void formation during resin transfer molding process*. Composites Science and Technology, 2006. **66**: p. 3281-3289.
115. Kardos, J., *Critical issues in achieving desirable mechanical properties for short fiber composites*. Pure and applied chemistry, 1985. **57**(11): p. 1651-1657.
116. Qiu, Y.P. and Weng, G.J., *On the application of Mori-Tanaka's theory involving transversely isotropic spheroidal inclusions*. International Journal of Engineering Science, 1990. **28**(11): p. 1121-1137.
117. Mori, T. and Tanaka, K., *Average stress in matrix and elastic energy of materials with misfitting inclusions*. Acta Metallurgica, 1973. **21**: p. 571-574.
118. Fukunaga, H. and Chou, T.-W., *Strength of Intermingled Hybrid Composites*. Journal of Reinforced Plastics and Composites, 1984. **3**.
119. Hauert, A., Rossoll, A., and Mortensen, A., *Young's modulus of ceramic particle reinforced aluminium: Measurement by the Impulse Excitation Technique and confrontation with analytical models*. Composites Part A: Applied Science and Manufacturing, 2009. **40**(4): p. 524-529.
120. Chen, Z., Gandhi, U., Lee, J., and Wagoner, R.H., *Variation and consistency of Young's modulus in steel*. Journal of Materials Processing Technology, 2016. **227**: p. 227-243.
121. Lopes, M.A., Silva, R.F., Monteiro, F.J., and Santos, J.D., *Microstructural dependence of Young's and shear moduli of P2O5 glass reinforced hydroxyapatite for biomedical applications*. Biomaterials, 2000. **21**(7): p. 749-754.
122. Schmidt, R., Wicher, V., and Tilgner, R., *Young's modulus of moulding compounds measured with a resonance method*. Polymer Testing, 2005. **24**(2): p. 197-203.
123. Viens, M.J. and Johnson, J.J., *Determination of elastic moduli of fiber-resin composites using an impulse excitation technique*. NASA Technical Memorandum 104629, 1996.
124. Song, W., Zhong, Y., and Xiang, J., *Mechanical parameters identification for laminated composites based on the impulse excitation technique*. Composite Structures, 2017. **162**: p. 255-260.
125. Pierri, D. *Lost core: new perspectives in die casting*. 2012; Available from: <http://doc.assofond.it/congr2012/tecn/2BUHLER.pdf>.
126. Yaokawa, J., Miura, D., Anzai, K., Yamada, Y., and Yoshii, H., *Strength of Salt Core Composed of Alkali Carbonate and Alkali Chloride Mixtures Made by Casting Technique*. Materials Transactions, 2007. **48**(5): p. 1034-1041.
127. Jelinek, P., Miksovsky, F., Beno, J., and Adamkova, E., *Development of foundry cores based on inorganic salts*. Materials and technology, 2013. **47**: p. 689-693.
128. Edward, B.F. and Paul, G.A., *Process for making soluble cores*. 1974, U.S. Patents.
129. Pierri, D. *Lost core - neue Perspektiven im Druckguss*. 2013; Available from: www.fhnw.ch/technik/forschung-und-entwicklung/giesserei-zentrum/giessereitag/giessereitag-2013/lost-core-neue-perspektiven-im-druckguss-dario-pierri-buhler-ag.pdf.
130. Taylor, L.S. and York, P., *Characterization of the Phase Transitions of Trehalose Dihydrate on Heating and Subsequent Dehydration*. Journal of Pharmaceutical Sciences, 1998. **87**(3): p. 347-355.
131. Sussich, F., Urbani, R., Princivalle, F., and Cesaro, A., *Polymorphic Amorphous and Crystalline Forms of Trehalose*. J. Am. Chem. Soc, 1998. **120**: p. 7893-7899.

132. Furuki, T., Kishi, A., and Sakurai, M., *De- and rehydration behavior of α,α -trehalose dihydrate under humidity-controlled atmospheres*. Carbohydrate Research, 2005. **340**: p. 429-438.
133. German, R.M., *Powder metallurgy science*. Metal Powder Industries Federation, 105 College Rd. E, Princeton, N. J. 08540, U. S. A, 1984. 279, 1984.
134. Rao, A.S.M., Narender, K., Rao, K.G.K., and Krishna, N.G., *Thermophysical Properties of NaCl, NaBr and NaF by r-Ray Attenuation Technique*. Journal of Modern Physics, 2013. **04**(02): p. 208-214.
135. *ROHACELL for the Automotive Industry*. [cited 2016; Available from: <http://www.rohacell.com/sites/lists/PP-HP/Documents/ROHACELL-Automotive-EN.pdf>.
136. Newman, S. and Meyer, F.J., *Mica composites of improved strength*. Polymer Composites, 1980. **1**(1): p. 37-43.
137. Gunay, M., Aslan, E., Korkut, I., and Seker, U., *Investigation of the effect of rake angle on main cutting force*. International Journal of Machine Tools & Manufacture, 2004. **44**: p. 953-959.